Measurement of double-differential cross sections for mesonless charged-current muon neutrino interactions on argon with final-state protons using the MicroBooNE detector

P. Abratenko,[38] O. Alterkait,[38] D. Andrade Aldana,[15] L. Arellano,[21] J. Asaadi,[37] A. Ashkenazi,[35] S. Balasubramanian,[12] B. Baller,[12] G. Barr,[28] D. Barrow,[28] J. Barrow,[25] V. Basque,[12] O. Benevides Rodrigues,[15] S. Berkman,[12,24] A. Bhanderi,[21] A. Bhat,[7] M. Bhattacharya,[12] M. Bishai,[3] A. Blake,[18] B. Bogart,[23] T. Bolton,[17] J. Y. Book,[14] M. B. Brunetti,[41] L. Camilleri,[10] Y. Cao,[21] D. Caratelli,[4] F. Cavanna,[12] G. Cerati,[12] A. Chappell,[41] Y. Chen,[31] J. M. Conrad,[22] M. Convery,[31] L. Cooper-Troendle,[29] J. I. Crespo-Anadón,[6] R. Cross,[41] M. Del Tutto,[12] S. R. Dennis,[5] P. Detje,[5] A. Devitt,[18] R. Diurba,[2] Z. Djurcic,[1] R. Dorrill,[15] K. Duffy,[28] S. Dytman,[29] B. Eberly,[33] P. Englezos,[30] A. Ereditato,[7,12] J. J. Evans,[21] R. Fine,[19] W. Foreman,[15] B. T. Fleming,[7] D. Franco,[7] A. P. Furmanski,[25] F. Gao,[4] D. Garcia-Gamez,[13] S. Gardiner,[12] G. Ge,[10] S. Gollapinni,[19] E. Gramellini,[21] P. Green,[28] H. Greenlee,[12] L. Gu,[18] W. Gu,[3] R. Guenette,[21] P. Guzowski,[21] L. Hagaman,[7] O. Hen,[22] C. Hilgenberg,[25] G. A. Horton-Smith,[17] Z. Imani,[38] B. Irwin,[25] M. S. Ismail,[29] C. James,[12] X. Ji,[26] J. H. Jo,[3] R. A. Johnson,[8] Y.-J. Jwa,[10] D. Kalra,[10] N. Kamp,[22] G. Karagiorgi,[10] W. Ketchum,[12] M. Kirby,[3,12] T. Kobilarcik,[12] I. Kreslo,[2] N. Lane,[21] I. Lepetic,[30] J.-Y. Li,[11] Y. Li,[3] K. Lin,[30] B. R. Littlejohn,[15] H. Liu,[3] W. C. Louis,[19] X. Luo,[4] C. Mariani,[40] D. Marsden,[21] J. Marshall,[41] N. Martinez,[17] D. A. Martinez Caicedo,[32] S. Martynenko,[3] A. Mastbaum,[30] I. Mawby,[18] N. McConkey,[39] V. Meddage,[17] J. Mendez,[20] J. Micallef,[22,38] K. Miller,[7] A. Mogan,[9] T. Mohayai,[12,16] M. Mooney,[9] A. F. Moor,[5] C. D. Moore,[12] L. Mora Lepin,[21] M. M. Moudgalya,[21] S. Mulleriababu,[2] D. Naples,[29] A. Navrer-Agasson,[21] N. Nayak,[3] M. Nebot-Guinot,[11] J. Nowak,[18] N. Oza,[10] O. Palamara,[12] N. Pallat,[25] V. Paolone,[29] A. Papadopoulou,[1] V. Papavassiliou,[27] H. B. Parkinson,[11] S. F. Pate,[27] N. Patel,[18] Z. Pavlovic,[12] E. Piasetzky,[35] K. Pletcher,[24] I. Pophale,[18] X. Qian,[3] J. L. Raaf,[12] V. Radeka,[3] A. Rafique,[1] M. Reggiani-Guzzo,[11,21] L. Ren,[27] L. Rochester,[31] J. Rodriguez Rondon,[32] M. Rosenberg,[38] M. Ross-Lonergan,[19] I. Safa,[10] G. Scanavini,[42] D. W. Schmitz,[7] A. Schukraft,[12] W. Seligman,[10] M. H. Shaevitz,[10] R. Sharankova,[12] J. Shi,[5] E. L. Snider,[12] M. Soderberg,[34] S. Söldner-Rembold,[21] J. Spitz,[23] M. Stancari,[12] J. St. John,[12] T. Strauss,[12] A. M. Szelc,[11] W. Tang,[36] N. Taniuchi,[5] K. Terao,[31] C. Thorpe,[21] D. Torbunov,[3] D. Totani,[4] M. Toups,[12] A. Trettin,[21] Y.-T. Tsai,[31] J. Tyler,[17] M. A. Uchida,[5] T. Usher,[31] B. Viren,[3] M. Weber,[2] H. Wei,[20] A. J. White,[7] S. Wolbers,[12] T. Wongjirad,[38] M. Wospakrik,[12] K. Wresilo,[5] W. Wu,[29] E. Yandel,[4] T. Yang,[12] L. E. Yates,[12] H. W. Yu,[3] G. P. Zeller,[12] J. Zennamo,[12] and C. Zhang[3]

(The MicroBooNE Collaboration)*

[1] *Argonne National Laboratory (ANL), Lemont, IL, 60439, USA*
[2] *Universität Bern, Bern CH-3012, Switzerland*
[3] *Brookhaven National Laboratory (BNL), Upton, NY, 11973, USA*
[4] *University of California, Santa Barbara, CA, 93106, USA*
[5] *University of Cambridge, Cambridge CB3 0HE, United Kingdom*
[6] *Centro de Investigaciones Energéticas, Medioambientales y Tecnológicas (CIEMAT), Madrid E-28040, Spain*
[7] *University of Chicago, Chicago, IL, 60637, USA*
[8] *University of Cincinnati, Cincinnati, OH, 45221, USA*
[9] *Colorado State University, Fort Collins, CO, 80523, USA*
[10] *Columbia University, New York, NY, 10027, USA*
[11] *University of Edinburgh, Edinburgh EH9 3FD, United Kingdom*
[12] *Fermi National Accelerator Laboratory (FNAL), Batavia, IL 60510, USA*
[13] *Universidad de Granada, Granada E-18071, Spain*
[14] *Harvard University, Cambridge, MA 02138, USA*
[15] *Illinois Institute of Technology (IIT), Chicago, IL 60616, USA*
[16] *Indiana University, Bloomington, IN 47405, USA*
[17] *Kansas State University (KSU), Manhattan, KS, 66506, USA*
[18] *Lancaster University, Lancaster LA1 4YW, United Kingdom*
[19] *Los Alamos National Laboratory (LANL), Los Alamos, NM, 87545, USA*
[20] *Louisiana State University, Baton Rouge, LA, 70803, USA*
[21] *The University of Manchester, Manchester M13 9PL, United Kingdom*
[22] *Massachusetts Institute of Technology (MIT), Cambridge, MA, 02139, USA*
[23] *University of Michigan, Ann Arbor, MI, 48109, USA*
[24] *Michigan State University, East Lansing, MI 48824, USA*
[25] *University of Minnesota, Minneapolis, MN, 55455, USA*
[26] *Nankai University, Nankai District, Tianjin 300071, China*
[27] *New Mexico State University (NMSU), Las Cruces, NM, 88003, USA*

[28] University of Oxford, Oxford OX1 3RH, United Kingdom
[29] University of Pittsburgh, Pittsburgh, PA, 15260, USA
[30] Rutgers University, Piscataway, NJ, 08854, USA
[31] SLAC National Accelerator Laboratory, Menlo Park, CA, 94025, USA
[32] South Dakota School of Mines and Technology (SDSMT), Rapid City, SD, 57701, USA
[33] University of Southern Maine, Portland, ME, 04104, USA
[34] Syracuse University, Syracuse, NY, 13244, USA
[35] Tel Aviv University, Tel Aviv, Israel, 69978
[36] University of Tennessee, Knoxville, TN, 37996, USA
[37] University of Texas, Arlington, TX, 76019, USA
[38] Tufts University, Medford, MA, 02155, USA
[39] University College London, London WC1E 6BT, United Kingdom
[40] Center for Neutrino Physics, Virginia Tech, Blacksburg, VA, 24061, USA
[41] University of Warwick, Coventry CV4 7AL, United Kingdom
[42] Wright Laboratory, Department of Physics, Yale University, New Haven, CT, 06520, USA

(Dated: March 29, 2024)

Charged-current neutrino interactions with final states containing zero mesons and at least one proton are of high interest for current and future accelerator-based neutrino oscillation experiments. Using the Booster Neutrino Beam and the MicroBooNE detector at Fermi National Accelerator Laboratory, we have obtained the first double-differential cross section measurements of this channel for muon neutrino scattering on an argon target with a proton momentum threshold of 0.25 GeV/c. We also report a flux-averaged total cross section of $\sigma = (11.8 \pm 1.2) \times 10^{-38}$ cm^2 / Ar and several single-differential measurements which extend and improve upon previous results. Statistical and systematic uncertainties are quantified with a full treatment of correlations across 359 kinematic bins, including correlations between distributions describing different observables. The resulting data set provides the most detailed information obtained to date for testing models of mesonless neutrino-argon scattering.

I. INTRODUCTION

Accelerator-based measurements of neutrino oscillations will be critical for definitively answering key open questions in high-energy physics, including whether charge-parity (CP) violation [1] occurs in the lepton sector, whether *sterile* neutrino species [2] (which do not participate in the weak interaction) exist, and whether ν_3 is the heaviest or lightest of the known neutrino mass eigenstates [3]. In the coming years, the Fermilab-based Short Baseline Neutrino (SBN) program [4] and Deep Underground Neutrino Experiment (DUNE) [5] will both pursue high-precision neutrino oscillation analyses using liquid argon time projection chambers (LArTPCs) as the primary detector technology. Maximizing the discovery potential of these large experimental efforts will require substantial improvements to the present understanding of GeV-scale neutrino-nucleus scattering physics [6]. An emerging literature of neutrino-argon cross-section measurements [7], pioneered by the ArgoNeuT [8] and MicroBooNE [9] LArTPC experiments, will provide the most direct constraints for refining interaction models to the precision needed for SBN and DUNE.

This article contributes to that effort by presenting measurements of differential cross sections for charged-current (CC) ν_μ scattering on argon leading to final states containing no mesons and one or more protons. This event topology (hereafter abbreviated as CC0πNp) is the dominant neutrino interaction channel for the SBN program, and its contribution is expected to remain important for DUNE oscillation analyses. The results presented herein build upon a previous MicroBooNE investigation [10] which measured single-differential neutrino-argon cross sections in the CC0πNp channel for the first time. The present work leverages subsequent improvements to the MicroBooNE simulation [11], reconstruction [12], and systematic uncertainty quantification [13] to achieve more detailed measurements, including multiple double-differential distributions. The analysis also benefits from a significantly larger data set, which was recorded by the MicroBooNE detector [9] with a total exposure of 6.79×10^{20} protons on target (POT) from the Fermilab Booster Neutrino Beam (BNB) [14].

Various kinematic distributions involving the three-momenta of the final-state muon and leading proton are measured and compared to simulations in this article. An innovative feature of the data set is the strategy used for its presentation; covariances between all 359 kinematic bins studied in the analysis are reported and used to quantify an overall goodness-of-fit of theoretical predictions. The full group of cross-section measurements may thus be regarded as a single result with greater combined model discrimination power (due to the need to describe inter-distribution correlations) than its constituent parts. Together with the inclusive cross-section measurements recently reported by MicroBooNE in Refs. [15, 16], this analysis thus represents a first application of the "block-wise unfolding" technique proposed in Ref. [17].

* microboone_info@fnal.gov

The experimental setup and simulations used in the analysis are described in Sec. II. Section III presents the signal definition and the event selection criteria. Section IV discusses the strategy for reporting the results, including the observables measured and the general approach to corrections for imperfect event reconstruction. The procedures used to estimate uncertainties and convert measured event distributions to cross sections are documented in Secs. V and VI, respectively. Section VII reports the cross-section results and compares them to several model predictions. Finally, Sec. VIII contains a summary and conclusions.

II. MICROBOONE EXPERIMENT AND SIMULATION

The MicroBooNE detector [9] is a LArTPC that operated in the BNB from 2015–2021. The detector's 85-tonne active mass of liquid argon was exposed to a 273 V/cm electric field and instrumented with three wire planes and thirty-two photomultiplier tubes (PMTs). Acrylic disks coated with tetraphenyl butadiene (TPB) were placed in front of the PMTs to convert the 128-nm argon scintillation light into visible wavelengths for efficient detection.

Neutrinos from the BNB are generated by bombarding a beryllium target with 8-GeV protons. Secondary particles produced by the proton collisions are focused by a magnetic horn and decay in flight. The decay products are directed toward a beam stop made of steel and concrete that absorbs particles other than neutrinos. During operation, the MicroBooNE detector was located 463 m downstream from the target along the beam axis. The BNB neutrino flux at this position is dominated by muon neutrinos with a mean energy of 0.8 GeV. Minor contributions from $\bar{\nu}_\mu$ (5.8%) and a mixture of ν_e and $\bar{\nu}_e$ (0.5% combined) are also present.

Interpretation of the data obtained from the MicroBooNE detector is enabled by a suite of Monte Carlo simulations that provide comprehensive modeling of the entire experiment. Neutrino beam production is simulated using the Geant4 framework [18, 19] and a detailed representation of the BNB apparatus developed by the MiniBooNE collaboration [14].

A. Neutrino interaction model

Neutrino interactions are modeled in the MicroBooNE simulation chain using version 3.0.6 of the GENIE neutrino event generator [20–22] with the `G18_10a_02_11a` configuration. This configuration includes a local Fermi gas (LFG) representation of the nuclear ground state [23] and the Valencia model for quasielastic (QE) and two-particle two-hole (2p2h) interactions in the CC channel [24–28]. Resonance production (RES) is simulated with the model of Kuzmin-Lyubushkin-Naumov and Berger-Sehgal (KLN-BS) [29–32], deep inelastic scattering [33] (DIS) is described using the structure functions of Bodek and Yang [34, 35], and coherent pion production (COH) follows the Berger-Sehgal approach [36]. Intranuclear hadronic final-state interactions (FSI) are simulated using the hA2018 model [37]. Several model parameters relevant for calculations of neutrino-nucleon cross-sections were tuned by the GENIE collaboration to data sets from bubble chamber experiments [38].

The GENIE v3.0.6 `G18_10a_02_11a` configuration described above was modified with MicroBooNE-specific tuning [11] of two CCQE and two CC2p2h model parameters to data from the T2K experiment reported in Ref. [39]. The resulting interaction model is referred to as the *MicroBooNE Tune* in the remainder of this article.

B. Detector simulation

Final-state particles produced in GENIE events are transported through the MicroBooNE detector geometry using version 10.3.3 of Geant4 [18, 19]. The response of the detector electronics to these particles is modeled using a custom simulation implemented within the LArSoft framework [40]. This detector response model includes data-driven treatments of position dependence in the wire responses, distortion of the time projection chamber (TPC) electric field due to buildup of slow-moving positive ions (space-charge effects), and dynamically-induced charge [41–45].

Backgrounds generated by cosmic rays and other sources unrelated to the neutrino beam are directly measured in the analysis using *beam-off* data samples collected at times when the BNB was not active. To ensure that these backgrounds are properly treated when reconstructing simulated neutrino interactions, an *overlay* technique is used; simulated TPC wire and PMT waveforms induced by GENIE neutrino scattering events are superimposed on measured waveforms from beam-off data before analysis [46].

III. SIGNAL DEFINITION AND EVENT SELECTION

A neutrino scattering event is considered part of the signal for this analysis if it fulfills the following criteria:

(1) A muon neutrino undergoes a CC interaction with an argon nucleus.

(2) The final state contains at least one proton.

(3) The momentum of the outgoing muon lies within the interval [0.1, 1.2] GeV/c.

(4) The momentum of the leading final-state proton (i.e., the proton with the highest momentum) lies within the interval [0.25, 1.0] GeV/c.

(5) The final state contains zero mesons and zero antimesons.

The momentum limits on the muon and leading proton in signal requirements (3) and (4) are motivated by considerations of efficiency, resolution, and systematic uncertainties. Apart from adjustments to these momentum limits, the signal definition given above is the same as the one adopted in the previous MicroBooNE CC0πNp analysis [10].

A. Reconstruction workflow

Identification of candidate CC0πNp signal events in this article relies upon an automated event reconstruction workflow implemented within the Pandora multi-algorithm pattern-recognition toolkit [47]. The individual hits reconstructed from the pulses recorded by each of the TPC wire planes are clustered in 2D and then correlated to produce 3D particle candidates. Collections of nearby particle candidates are grouped into *slices*, and information from both the TPC and PMTs is used to identify a maximum of one slice per event that contains a candidate neutrino interaction. Algorithms to calculate additional reconstructed quantities, such as the particle identification score described in Ref. [12] and the muon momentum estimator described in Ref. [48], are combined with this generic neutrino selection to perform the analysis.

B. Event categories

Plots of reconstructed event distributions in Fig. 1 and Figs. 7–14 show the prediction of the MicroBooNE simulation as a stacked histogram that distinguishes between the following categories of events:

Signal: All events which satisfy signal requirements (1) to (5) and have a true neutrino vertex position that falls within the fiducial volume defined in selection requirement (I) from Sec. III C. Signal events are divided into subcategories based on whether the primary interaction mode is QE, 2p2h, or any other process. The last of these subcategories is dominated by resonant pion production followed by intranuclear pion absorption.

Out FV: Events in which the true neutrino vertex falls outside of the fiducial volume (FV). This category includes all final-state topologies since it is defined solely in terms of the true vertex location.

CC$N\pi$: Events containing a charged-current ν_μ interaction which produces one or more final-state pions of any charge. These fail to satisfy signal requirement (5). Note that ν_μ CC events containing final-state mesons other than pions fall into another event category.

CC0π0p: Charged-current ν_μ events containing zero final-state pions of any momentum and zero protons within the true momentum limits imposed by signal requirement (4). Events with any number of mesons other than pions are allowed in this category.

Other CC: Charged-current ν_μ events which do not fall into any of the previous categories. Among these are events which would otherwise be signal but do not satisfy the muon momentum limits imposed by signal requirement (3). This category also includes events containing at least one proton within the momentum limits from signal requirement (4) together with one or more mesons other than pions.

ν_e CC: Events involving a charged-current ν_e interaction inside the fiducial volume. These fail to satisfy signal requirement (1).

NC: Events in which a neutrino or antineutrino of any flavor undergoes a neutral-current interaction within the fiducial volume. These fail to satisfy signal requirement (1).

Beam-off: Cosmic-ray-induced backgrounds.

Other: All events which do not fall into one of the other categories defined above. This category is dominated by CC interactions of antineutrinos.

C. Inclusive ν_μ CC preselection

Following automated reconstruction using the Pandora framework, twelve event-selection criteria are applied to distinguish the CC0πNp signal from other event topologies. These criteria are divided into a preselection that seeks to identify inclusive ν_μ CC events (described in the following paragraphs), quality checks to eliminate events with a poorly-reconstructed final-state muon (Sec. III D), and additional requirements designed to isolate mesonless final states containing one or more protons (Sec. III E). Overall performance of the selection is then discussed in Sec. III F, including evolution of the efficiency and purity as each requirement is applied.

In order of application, the selection criteria used to identify ν_μ CC candidate events are as follows:

(I) The position of the reconstructed neutrino vertex must lie within a fiducial volume representing a region in which the efficiency of the remainder of the selection is appreciable and the detector response is well-understood. The fiducial volume chosen for this analysis is a rectangular prism with most boundaries parallel to and 21.5 cm inward from the edges of the active volume of the MicroBooNE detector. The only exception is the boundary that is perpendicular to the beam on the downstream side. This boundary is chosen to be 70 cm inward

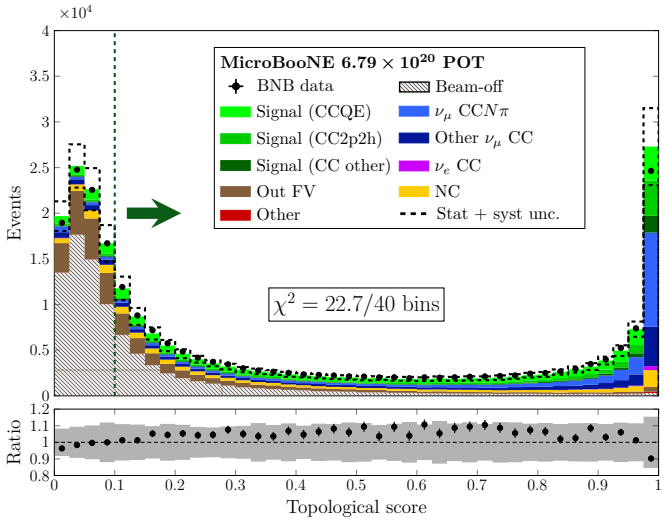

FIG. 1. Distribution of topological score values obtained when applying the ν_μ CC inclusive preselection. The portion near zero is dominated by beam-off events as expected. The green arrow points into the region in which events are accepted by selection requirement (III). The dashed lines indicate the total uncertainty on the simulation prediction evaluated according to the prescription given in Sec. V. The lower panel shows the ratio of the data to the simulation prediction. The same total uncertainty band is represented by the shaded gray region.

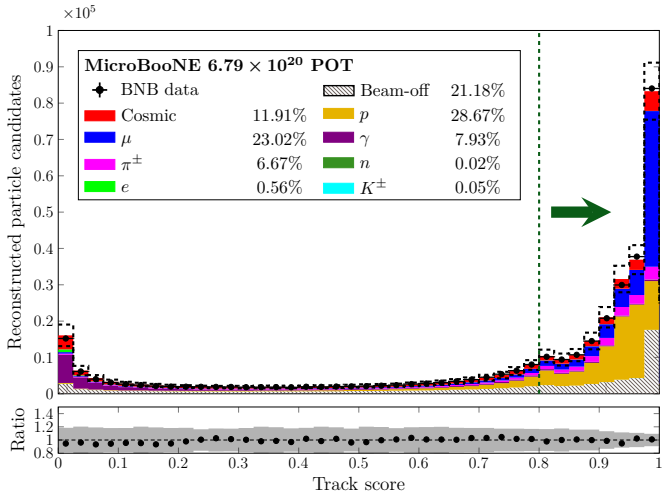

FIG. 2. Track score criterion applied to all reconstructed primary particles when searching for a muon candidate. The green arrow points into the region in which particle candidates are accepted. The percentages in the legend indicate the fraction of reconstructed particles of each type before the illustrated selection is applied. The lower panel shows the ratio of the data to the simulation prediction. The uncertainty on the simulation prediction is represented by the dashed lines in the top panel and the gray region in the bottom panel.

from the edge of the active volume to enable better acceptance of forward-going muons.

(II) Starting points for all reconstructed primary particles (i.e., those labeled by the reconstruction as direct progeny of the neutrino) are required to lie within a looser containment volume offset inward from the active volume edges by 10 cm on all sides.

(III) The topological score [49] assigned to the event must be greater than 0.1. This score represents the output of a support-vector machine designed to classify events as either neutrino-like (scores near 1) or cosmic-ray-like (scores near 0). Figure 1 shows the measured distribution of this variable, obtained at this stage of the selection, compared to the prediction from the MicroBooNE simulation chain. The topological score threshold of 0.1 is sufficient to remove a large fraction of beam-off and out-of-fiducial-volume backgrounds.

(IV) The event must contain a muon candidate, which is defined as a reconstructed primary particle that satisfies the following criteria:

a. The track score [49, 50] assigned to the particle by the reconstruction must be greater than 0.8. This score classifies reconstructed particles as shower-like (values near 0) and track-like (values near 1). This requirement slightly increases the muon purity (see Fig. 2). The "cosmic" ("beam-off") category in the legend represents reconstructed particle candidates attributed to cosmic-ray activity in events that include (do not include) a simulated neutrino interaction. All other categories represent reconstructed particle candidates that correspond to a specific kind of true particle produced by a simulated neutrino interaction.

b. The Euclidean distance between the particle's reconstructed starting position and the reconstructed neutrino vertex must be less than 4 cm (see Fig 3). This is a minor quality check to ensure that the muon candidate is correctly associated with the reconstructed neutrino vertex.

c. The length of the particle track must be greater than 10 cm (see Fig 4). Tracks below this length are overwhelmingly generated by protons and cosmic activity. The lower limit on the muon momentum applied in signal requirement (3) helps to mitigate the impact of this cut on the efficiency for very low-energy muons.

d. The log-likelihood ratio particle-identification (LLR PID) score assigned to the particle must exceed 0.2 (see Fig. 5). This score is calculated by comparing track hit information from all three TPC wire planes to theoretical templates for muons and protons. The logarithm of a likelihood ratio for these two parti-

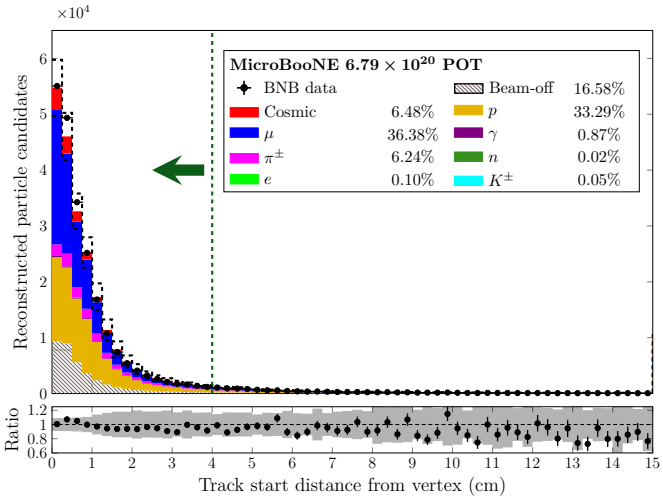

FIG. 3. Distribution of distances between the reconstructed neutrino vertex and reconstructed primary particles. The green arrow points into the region in which particles are accepted as possible muon candidates. The percentages in the legend indicate the fraction of reconstructed particles of each type before the illustrated selection is applied. The lower panel shows the ratio of the data to the simulation prediction. The uncertainty on the simulation prediction is represented by the dashed lines in the top panel and the gray region in the bottom panel.

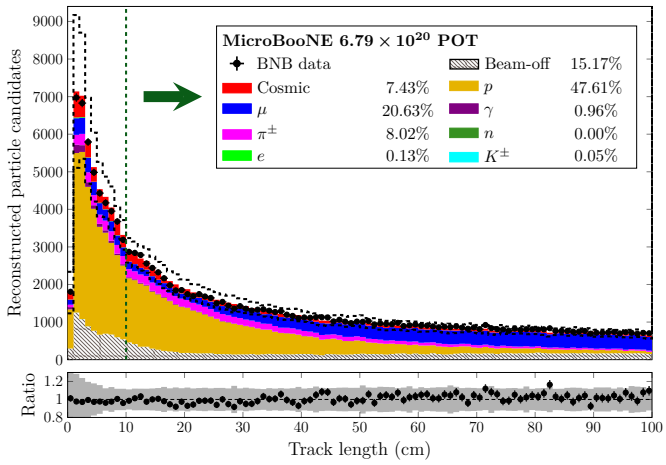

FIG. 4. Track length criterion applied to reconstructed primary particles when searching for a muon candidate. The green arrow points into the region in which particle candidates are accepted. The percentages in the legend indicate the fraction of reconstructed particles of each type before the illustrated selection is applied. The lower panel shows the ratio of the data to the simulation prediction. The uncertainty on the simulation prediction is represented by the dashed lines in the top panel and the gray region in the bottom panel.

cle identification hypotheses is then converted to a score where -1 is most proton-like and 1 is most muon-like. Reference [12] describes this particle identification technique in greater detail.

In cases where two or more reconstructed primary particles satisfy these criteria, the one with the highest LLR PID score (most muon-like) is considered the muon candidate.

D. Muon momentum reconstruction quality checks

Three additional selection criteria are applied immediately after the ν_μ CC preselection to ensure adequate reconstruction of the outgoing muon momentum. In order of application, they are as follows:

(V) The muon candidate track must have a reconstructed end point within the containment volume defined in selection requirement (II). Requiring containment allows for a reliable track-length-based estimate of the muon momentum. This criterion substantially improves the resolution when reconstructing the muon momentum and derived quantities (e.g., δp_T) at the cost of a notable drop in efficiency.

(VI) Muon momentum estimators based on multiple Coulomb scattering [48] (p_μ^{MCS}) and based on track length [51] (p_μ^{range}) for the muon candidate track must agree with each other within 25%, i.e., they must satisfy the relation

$$\frac{\left|p_\mu^{\mathrm{range}} - p_\mu^{\mathrm{MCS}}\right|}{p_\mu^{\mathrm{range}}} < 0.25\,. \tag{1}$$

This requirement removes events in which only a portion of the full muon track is successfully reconstructed.

(VII) The track-length-based estimator for the reconstructed muon momentum p_μ^{range} must lie within the limits imposed by requirement (3) from the signal definition: $0.1\ \mathrm{GeV}/c \leq p_\mu^{\mathrm{range}} \leq 1.2\ \mathrm{GeV}/c$.

E. $0\pi Np$ selection

The remaining five criteria from the full CC$0\pi Np$ selection are intended to isolate final states containing zero mesons and one or more protons. In order of application, they are

(VIII) All reconstructed primary particles must have a track score higher than 0.5 (track-like). This requirement eliminates events containing electromagnetic showers, which are not expected for mesonless ν_μ interactions.

(IX) At least one reconstructed primary particle that is not the muon candidate must be present in the event. All such particles are considered proton candidates.

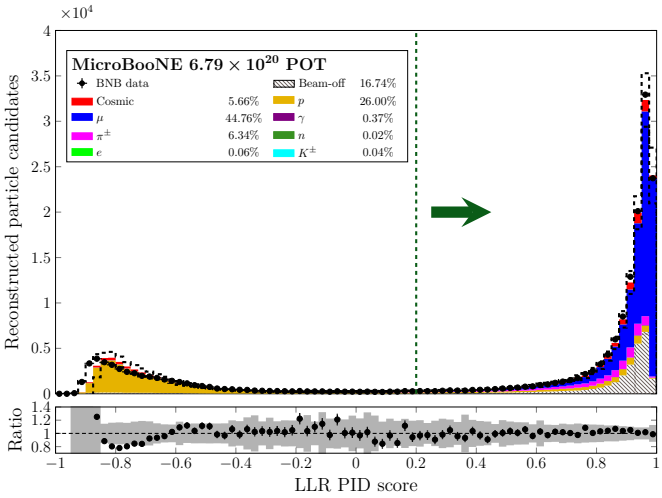

FIG. 5. Log-likelihood ratio particle ID score for reconstructed primary particles under consideration as possible muon candidates. The green arrow points into the region in which muon candidates are accepted by the selection. The percentages in the legend indicate the fraction of reconstructed particles of each type before the illustrated selection is applied. The lower panel shows the ratio of the data to the simulation prediction. The uncertainty on the simulation prediction is represented by the dashed lines in the top panel and the gray region in the bottom panel.

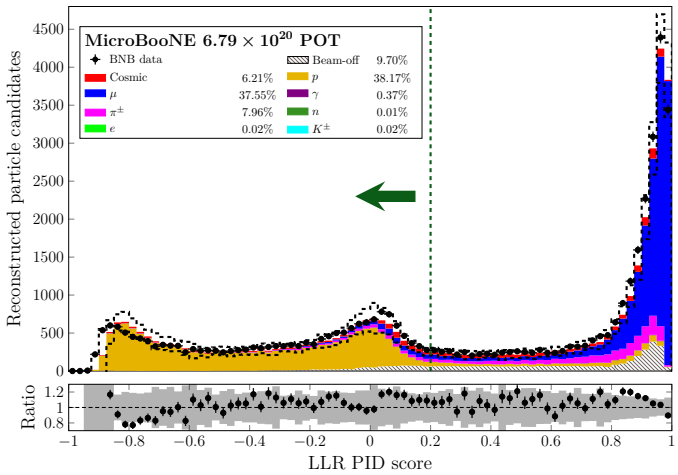

FIG. 6. Log-likelihood ratio particle ID requirement applied to proton candidates in selection requirement (XI). The green arrow points into the region in which proton candidates are accepted. The percentages in the legend indicate the fraction of reconstructed particles of each type before the illustrated selection is applied. The lower panel shows the ratio of the data to the simulation prediction. The uncertainty on the simulation prediction is represented by the dashed lines in the top panel and the gray region in the bottom panel.

(X) All proton candidates must have reconstructed end points that lie within the containment volume defined in selection requirement (II). This is a quality requirement intended to ensure that a track-length-based estimator of the proton momentum will be valid. Containment of the end point for the muon candidate is already enforced by selection requirement (V).

(XI) All proton candidates must have an LLR PID score less than 0.2 (see Fig. 6). The chosen cutoff value comes close to optimizing the product of efficiency and purity while maintaining good acceptance of low-momentum protons.

(XII) The longest proton candidate track must have a length-based momentum estimator p_p^{range} that falls within the limits given in requirement (4) from the signal definition: $0.25\ \text{GeV}/c \leq p_p^{\text{range}} \leq 1.0\ \text{GeV}/c$.

F. Overall selection performance

Events that satisfy all twelve selection requirements described in the previous subsections are considered the CC0πNp candidates of interest for this analysis. The full CC0πNp selection achieves an estimated overall efficiency of 12.3% and a purity of 78.5%. The evolution of these quantities as each requirement is applied is shown in Table I, as well as the relative efficiency ("Rel. eff."),

TABLE I. Evolution of the selection efficiency, purity, and relative efficiency as the various requirements described in the text are applied.

Requirement	Index	Eff.	Purity	Rel. eff.
No cuts	–	1.0000	0.0230	–
In FV	(I)	0.7817	0.2084	0.7817
Starts contained	(II)	0.7258	0.2114	0.9284
Topological score	(III)	0.6418	0.2945	0.8843
CC incl	(IV)	0.5720	0.3442	0.8913
μ contained	(V)	0.2381	0.3382	0.4162
μ quality	(VI)	0.1960	0.3967	0.8233
μ momentum limits	(VII)	0.1956	0.4044	0.9977
No showers	(VIII)	0.1716	0.4772	0.8775
Has p candidate	(IX)	0.1514	0.5300	0.8822
p contained	(X)	0.1435	0.5724	0.9482
p PID	(XI)	0.1249	0.7781	0.8700
p momentum limits	(XII)	0.1233	0.7851	0.9872

which is defined as the ratio of the selection efficiency after the current requirement is applied to the efficiency before it is applied. Equivalently, it is the efficiency calculated considering only those signal events accepted after applying all previous criteria.

IV. DATA PRESENTATION STRATEGY

The selection defined in the previous section is used in the remainder of this article to obtain single- and double-

differential cross sections for a variety of kinematic variables. To maximize the usefulness of these measurements for the neutrino interaction modeling community, an innovative strategy for reporting the results has been developed.

In previous MicroBooNE cross-section publications, and typically in the experimental neutrino scattering literature as a whole, individual kinematic distributions are treated as entirely separate entities. For example, in the article describing the previous MicroBooNE CC0πNp analysis [10], single-differential cross sections are shown for both the muon momentum and scattering angle (among several other observables), but the covariance matrices used to report the measurement uncertainties consider only correlations between bins of the same variable. Readers are thus obliged to treat each reported differential cross section as if it was obtained in isolation from all others. This reduces the power of the full multivariable data set since external users must either ignore correlations between the observables that are known to be important (e.g., those introduced by limited data statistics and systematic uncertainties on the neutrino flux prediction), invent ad hoc correlations that may be inaccurate, or consider only a single variable at a time when performing model comparisons. This problem has been encountered and discussed previously in the neutrino interaction literature [52], but standard practices for experimental data releases have not yet been adjusted to address it.

The present analysis overcomes this limitation by providing comprehensive uncertainties for all final results; cross sections are reported in a binning scheme that involves multiple variables, and an overall covariance matrix is computed that accounts for the measurement uncertainties and correlations between all pairs of bins. To avoid double-counting in the cross-section extraction procedure, bins describing the same kinematic distribution are grouped into distinct blocks. As described in the sections that follow, some mathematical operations are applied to each block independently, but the blockwise results are later merged together to form the final group of measurements.

A. Observables measured

Various observables related to the 3-momenta of the outgoing muon ($\mathbf{p}_\mu$) and leading proton ($\mathbf{p}_p$) are measured in this analysis. Studies of sub-leading protons in the CC0πNp channel are reserved for later work. In addition to the magnitude of the momentum for the muon (p_μ) and leading proton (p_p) and their scattering angles (θ_μ and θ_p, defined with respect to the neutrino direction $+\hat{\mathbf{z}}$), differential cross sections in several other variables are reported. These include the opening angle $\theta_{\mu p}$ between the muon and leading proton

$$\theta_{\mu p} \equiv \arccos\left(\frac{\mathbf{p}_\mu \cdot \mathbf{p}_p}{p_\mu\, p_p}\right), \tag{2}$$

as well as the magnitude δp_T of the transverse missing momentum

$$\delta\mathbf{p}_T \equiv \mathbf{p}_\mu^T + \mathbf{p}_p^T\,. \tag{3}$$

Here, $\mathbf{p}_\mu^T$ is the vector projection of the muon momentum transverse to the neutrino beam direction and $\mathbf{p}_p^T$ is the same for the leading proton. These vectors have magnitudes p_μ^T and p_p^T respectively. One may also describe the angular orientation of $\delta\mathbf{p}_T$ with respect to $\mathbf{p}_\mu^T$ using the angle

$$\delta\alpha_T \equiv \arccos\left(\frac{-\mathbf{p}_\mu^T \cdot \delta\mathbf{p}_T}{p_\mu^T\, \delta p_T}\right) \tag{4}$$

as well as the vector components

$$\delta p_{T_x} \equiv \frac{(\hat{\mathbf{z}} \times \mathbf{p}_\mu^T) \cdot \delta\mathbf{p}_T}{p_\mu^T}\,, \tag{5}$$

and

$$\delta p_{T_y} \equiv \frac{-\mathbf{p}_\mu^T \cdot \delta\mathbf{p}_T}{p_\mu^T} = \delta p_T \cdot \cos\delta\alpha_T\,, \tag{6}$$

where the hat on $\hat{\mathbf{z}}$ indicates that it is a unit vector.

Measurements of the transverse kinematic imbalance (TKI) variables δp_T, $\delta\alpha_T$ were originally proposed [53] as a means of exploring nuclear effects in neutrino scattering with a reduced dependence on the neutrino energy. Cross sections as a function of these variables for a hydrocarbon target have been reported by the T2K [54] and MINERvA [55] collaborations, the latter also extending [56] the investigation to δp_{T_x} and δp_{T_y}. In response to community interest [57] in measuring these observables using a LArTPC, a recent MicroBooNE analysis reported first neutrino-argon differential cross sections in TKI variables for an exclusive one-proton final state [58], including the first double-differential TKI measurement for neutrino scattering on any nuclear target [59]. The present work reports similar measurements for the more inclusive CC0πNp signal event topology.

Finally, this analysis measures an estimator p_n for the momentum of the initial struck neutron in the CC interaction. This estimator was proposed in Ref. [60] with similar phenomenological motivations as the TKI variables, but it is calculated using momentum components both transverse and longitudinal to the neutrino beam direction. Specifically, p_n is computed via the expression

$$p_n = \sqrt{\delta p_L^2 + \delta p_T^2} \tag{7}$$

where the reconstructed longitudinal missing momentum δp_L is given by

$$\delta p_L \equiv \frac{R}{2} - \frac{m_f^2 + \delta p_T^2}{2R}\,. \tag{8}$$

Here

$$m_f \equiv m_{\mathrm{Ar40}} - m_n + B \tag{9}$$

and

$$R \equiv m_{\mathrm{Ar40}} + p_\mu^z + p_p^z - E_\mu - E_p \,, \tag{10}$$

where $m_{\mathrm{Ar40}} = 37.215526$ GeV/c^2 is the mass of the ^{40}Ar nuclear target (not the atomic mass), $m_n = 0.93956541$ GeV/c^2 is the mass of a neutron, and $B = 0.02478$ GeV is the assumed average binding energy for a neutron in ^{40}Ar. The longitudinal momentum components and total energies of the muon (p_μ^z, E_μ) and leading proton (p_p^z, E_p) are also used above.

The value of B chosen in the present work is a weighted average of the neutron separation energies E_α given in Table I of Ref. [60] with the shell occupancies n_α used as the weights. An equivalent prescription for carbon (using Table II from the same reference) was adopted to estimate B in a prior MINERvA analysis that studied p_n [55]. The first measured neutrino cross sections in this observable for an argon target were recently reported by MicroBooNE for a one-proton final state [61] assuming a different value $B = 0.0309$ GeV based on a study of electron scattering data [62].

B. Estimation of inefficiency and bin migrations

Corrections for imperfect detector and reconstruction performance in the analysis are applied using an unfolding procedure documented in Sec. VI. The implementation of this procedure requires a description of the relationship between reconstructed and true values of the observables of interest. This relationship is estimated quantitatively by assigning simulated CC0πNp events to two duplicate sets of the bins defined in Table III of Appendix A. The *true bins* contain all simulated CC0πNp events that have true values of the observables that fall within the relevant kinematic limits. The *reconstructed bins* contain those events that pass the full selection and have appropriate reconstructed values of the observables.

With these definitions, the connection between the reconstructed and true observables is described using a *response matrix* Δ, which transforms a prediction of signal event counts in true bins μ into a corresponding prediction in reconstructed bins j. Each element of the response matrix is computed from the MicroBooNE simulation results according to the relation

$$\Delta_{j\mu} \equiv \frac{\phi_{j\mu}}{\phi_\mu} \,, \tag{11}$$

where ϕ_μ is the total number of signal events in true bin μ and $\phi_{j\mu}$ is the number of signal events which fall simultaneously into true bin μ and reconstructed bin j. Thus, the response matrix quantifies the effects of both inefficiency and smearing of the observables due to imperfect reconstruction. This matrix is employed in systematic uncertainty estimation and unfolding as described in Secs. V and VI respectively. It is plotted in Sec. IV of the supplemental materials.

One may also quantify the effect of smearing separately from inefficiency by calculating the *migration matrix* M. Each element of this matrix is estimated from simulation via the expression

$$M_{j\mu} = \frac{\phi_{j\mu}}{\sum_\ell \phi_{\ell\mu}} \,, \tag{12}$$

where, to avoid double-counting, the sum over ℓ includes only those reconstructed bins in the block of interest. The migration matrix element $M_{j\mu}$ is thus an estimate of the probability that a selected signal event belonging to true bin μ will be assigned to reconstructed bin j. Plots of the migration matrices for each of the 14 blocks of bins defined in Table III are given in Sec. II of the supplemental materials.

V. UNCERTAINTIES

Systematic uncertainties are estimated by modifying the nominal MicroBooNE simulation and calculating resultant variations in the expected number of selected events n_j in each reconstructed bin j. This expected event count includes contributions from both simulated neutrino interactions and measured constant-in-time backgrounds from beam-off data:

$$n_j = \phi_j + O_j + B_j \,. \tag{13}$$

Here the expected contents of the j-th reconstructed bin are divided into ϕ_j simulated signal CC0πNp events, O_j measured beam-off background events, and B_j simulated beam-correlated background events.

Uncertainties are quantified using covariance matrices calculated according to a multiple-universe procedure. Under this approach, the covariance between the expected event counts n_a and n_b in the a-th and b-th reconstructed bins is represented by the matrix element

$$V_{ab} = \frac{1}{N_{\mathrm{univ}}} \sum_{u=1}^{N_{\mathrm{univ}}} \left(n_a^{\mathrm{CV}} - n_a^u\right)\left(n_b^{\mathrm{CV}} - n_b^u\right) . \tag{14}$$

Here n_a^{CV} is the total event count in reconstructed bin a predicted by the central-value MicroBooNE simulation. The variable n_a^u is a prediction of the same quantity computed based on an alternate simulation (i.e., in an alternate *universe*) in which some aspect of the models used to describe the neutrino beam, particle interactions, and the detector response has been changed from the adopted central value. The total number of alternate universes N_{univ} included when computing the average in Eq. (14) depends on the systematic effect of interest. In some cases, only a single variation ($N_{\mathrm{univ}} = 1$) is used. Covariance matrices V_{ab} are calculated individually for each source of uncertainty. A total covariance matrix is then obtained by summing the individual contributions.

A. Sources of systematic uncertainty

Several classes of systematic uncertainties are considered in this analysis. Those related to the BNB flux prediction, which include variations related to the horn current and hadron production modeling, follow the treatment developed by the MiniBooNE collaboration [14]. Flux shape uncertainties are handled in a way which allows the final cross-section results to be reported based upon the predicted BNB ν_μ flux (tabulated in the supplemental materials) rather than the unknown true flux [63].

The GENIE-based neutrino interaction model and associated uncertainties used by MicroBooNE are documented in a dedicated publication [11]. Following Ref. [58], an additional single-universe variation to the neutrino interaction model is adopted in which an alternative event generator (version 19.02.2 of NuWro [64]) replaces GENIE in the MicroBooNE simulation chain and is used to predict the reconstructed event counts.

Uncertainties related to propagation of the final-state particles emerging from the neutrino interaction are calculated using the Geant4Reweight [65] software package. Systematic variations of the Geant4 [18, 19] total cross section model for positive pions, negative pions, and protons are considered. For protons, variations are applied to the elastic and reaction (i.e., total inelastic) channels separately. For pions, the elastic, quasielastic, absorption, single charge-exchange, double charge-exchange, and pion production channels are individually varied.

Systematic uncertainties on the detector response model are calculated for both the MicroBooNE photon detection system and the time projection chamber. For the former, three alternate universes are constructed in which the scintillation light yield, attenuation, and Rayleigh scattering length are individually varied. For the latter, space-charge effects, electron-ion recombination, and data-driven modifications to the simulated wire response [13] are considered.

Fully-correlated fractional uncertainties are also applied to the beam-related portion of the reconstructed events ($\phi_j + B_j$) to account for limited precision in the counting of protons delivered to the beam target (2%) and the number of argon atoms in the fiducial volume (1%).

B. Signal model uncertainty

For most of the systematic uncertainties mentioned above, the simulated reconstructed event counts ϕ_j and B_j are varied directly in each alternate universe. However, since uncertainties related to predicting the CC0πNp signal will only affect the final results via their impact on estimating the detection efficiency and bin migrations, a different treatment is used for neutrino interaction model variations. In this case, the expected number of selected signal events ϕ_j is rewritten in the form

$$\phi_j = \sum_\mu \Delta_{j\mu}\, \phi_\mu^{\mathrm{CV}}\,, \tag{15}$$

where $\Delta_{j\mu}$ is the response matrix element connecting true bin μ and reconstructed bin j. This quantity is varied in each alternate universe, while the expected signal event counts in the μ-th true bin ϕ_μ^{CV} are held constant at the central-value prediction (as indicated by the superscript). To avoid double-counting events, the sum over μ includes only those true bins that belong to the same block as the j-th reconstructed bin. Details about the binning scheme and response matrix definition are provided above in Sec. IV.

C. Statistical correlations

The data release strategy outlined in Sec. IV requires a slightly more complicated treatment of statistical uncertainties than has been typical for previous neutrino cross-section analyses. When every measured event belongs to exactly one bin, statistical fluctuations of the bin contents are described by independent Poisson distributions. In that case, the statistical covariance matrix is diagonal, and the variance of each bin is estimated by the number of observed counts.

However, reporting combined measurements over the multiple blocks of bins defined in Table III introduces correlations in the statistical uncertainties because the same event belongs to a unique bin in each block. Fortunately, the derivation of an estimator for the statistical covariance between two arbitrary bins is straightforward. As shown in Sec. III C 1 of Ref. [17], the statistical covariance between any pair of bins is estimated as simply the number of events that fall simultaneously into both of them. In the case of weighted Monte Carlo events, the sum of the squares of the event weights is used rather than the raw event count.

D. Impact on integrated cross section

The flux-averaged total CC0πNp cross section obtained by this analysis is $\sigma = (11.8 \pm 1.2) \times 10^{-38}$ cm^2 / Ar. The full fractional uncertainty of 9.8% includes contributions from the neutrino flux prediction (6.6%), neutrino interaction modeling (5.1%), detector response modeling (4.1%), beam exposure measurements (2.2%), data statistics (1.4%), estimation of the number of argon atoms in the fiducial volume (1.1%), modeling of final-state particle propagation (0.9%), and Monte Carlo statistics (0.8%). The data statistical uncertainty includes a contribution from the beam-off measurements used to estimate cosmic-ray backgrounds. The Monte Carlo statistical uncertainty includes a contribution from simulated neutrino-induced backgrounds from the BNB.

For the total cross-section measurement, the additional neutrino interaction modeling uncertainty estimated by using NuWro as an alternative event generator (1.7%) is substantially smaller than the uncertainty arising from GENIE systematic variations (4.8%). However, for many of the differential measurements reported below, the NuWro-based systematic uncertainty is larger. Full covariance matrices giving the contributions of both of these classes of interaction model variations to the total measurement uncertainty are reported in the supplemental materials. For the detector response model, the uncertainty related to the simulation of electron recombination [66] has a dominant impact on the total cross section result (3.3%).

E. Reconstructed event distributions

As an intermediate step in the analysis, the event selection presented in Sec. III and the uncertainty treatment described above were applied to measure candidate CC0πNp event rates in each of the 359 kinematic bins defined in Table III. The measured event rates and associated uncertainties were then used as input to the unfolding procedure defined in Sec. VI to obtain the final cross-section results.

The plots in Figs. 7 to 14 report the measured event rates (black data points) as a function of reconstructed observables for a total beam exposure of 6.79×10^{20} POT. The error bars on the data points show only the statistical uncertainty. The stacked histograms in the main panel of each plot show the central-value prediction from the MicroBooNE simulation chain. Individual contributions from the event categories defined in Sec. III are shown using the same color scheme as in Fig. 1. The total uncertainty (including statistical and systematic contributions) on the central-value prediction is indicated by the dashed lines. Below the main panel of each plot, the ratio of the data points to the central-value prediction is also shown, and the total uncertainty on the prediction is indicated by the gray band.

Reasonable agreement between the measured event rates and the MicroBooNE simulation prediction is seen across most of the phase space studied, yielding an overall χ^2 value of 355.25 for the 359 reconstructed bins. The areas of greatest tension are the muon angular distribution at moderate p_μ (see Fig. 7), as well as the individual and double-differential distributions of p_n and $\theta_{\mu p}$ (see Figs. 9 and 13).

F. Sideband-based validation of background model

Removal of the beam-correlated backgrounds in this analysis relies upon a simulation-based estimate B_j of their contribution to the measured event counts in each reconstructed bin j. A sideband study, described below, was performed to demonstrate that the background predictions from the MicroBooNE simulation are sufficiently precise to obtain the final measurements.

Three sets of alternative selection criteria were developed to enhance sensitivity to the three dominant backgrounds: events outside of the fiducial volume (Out FV, see Sec. III), neutral-current events (NC), and ν_μ charged-current events with one or more final-state pions (CC$N\pi$). In each case, the full CC0πNp selection was used as a starting point, and minor adjustments were made to improve acceptance of the background category of interest. By construction, all events which pass at least one set of alternative selection criteria are rejected by the original CC0πNp selection. The alternative selection criteria for each class of background are given below.

Out FV: The full CC0πNp selection is unaltered except that the event must fail requirement (I) (i.e., the reconstructed neutrino vertex position must lie outside the fiducial volume).

NC: The event must fail requirement (IV) (there must not be a muon candidate). The additional requirements (V)–(VII) applied to the muon candidate are also removed. All other CC0πNp selection criteria remain the same. The event must also contain at least two reconstructed primary particles. To allow all of the observables of interest to be defined for such events, the reconstructed primary particle with the longest track length is treated as the muon candidate, while the second-longest is treated as the leading proton candidate. Checks of the simulated NC events that passed the original CC0πNp selection revealed that this ordering by track length occurred in a large majority (88%) of cases.

CC$N\pi$: The full CC0πNp selection is unaltered except that requirement (XI) is reversed; at least one of the proton candidates must have an LLR PID score greater than 0.2 (muon-like).

To assess the adequacy of the background model for this analysis, the logical OR of these three alternative selections was applied to measure event rates. That is, an event was accepted by this combined sideband selection if it satisfied all of the criteria for at least one of the Out-FV-, NC-, or CC$N\pi$-enhanced selections described above. Good agreement between the MicroBooNE simulation prediction and the sideband data, within the uncertainties defined above, was found across the full phase space defined in Table III. An overall χ^2 value of 177.94 was obtained for the full set of 359 bins. Based on this successful comparison with the sideband data set, the background predictions of MicroBooNE's simulation are used unaltered to obtain the final cross-section results. Plots of the measured and predicted sideband event distributions are provided in Sec. III of the supplemental materials.

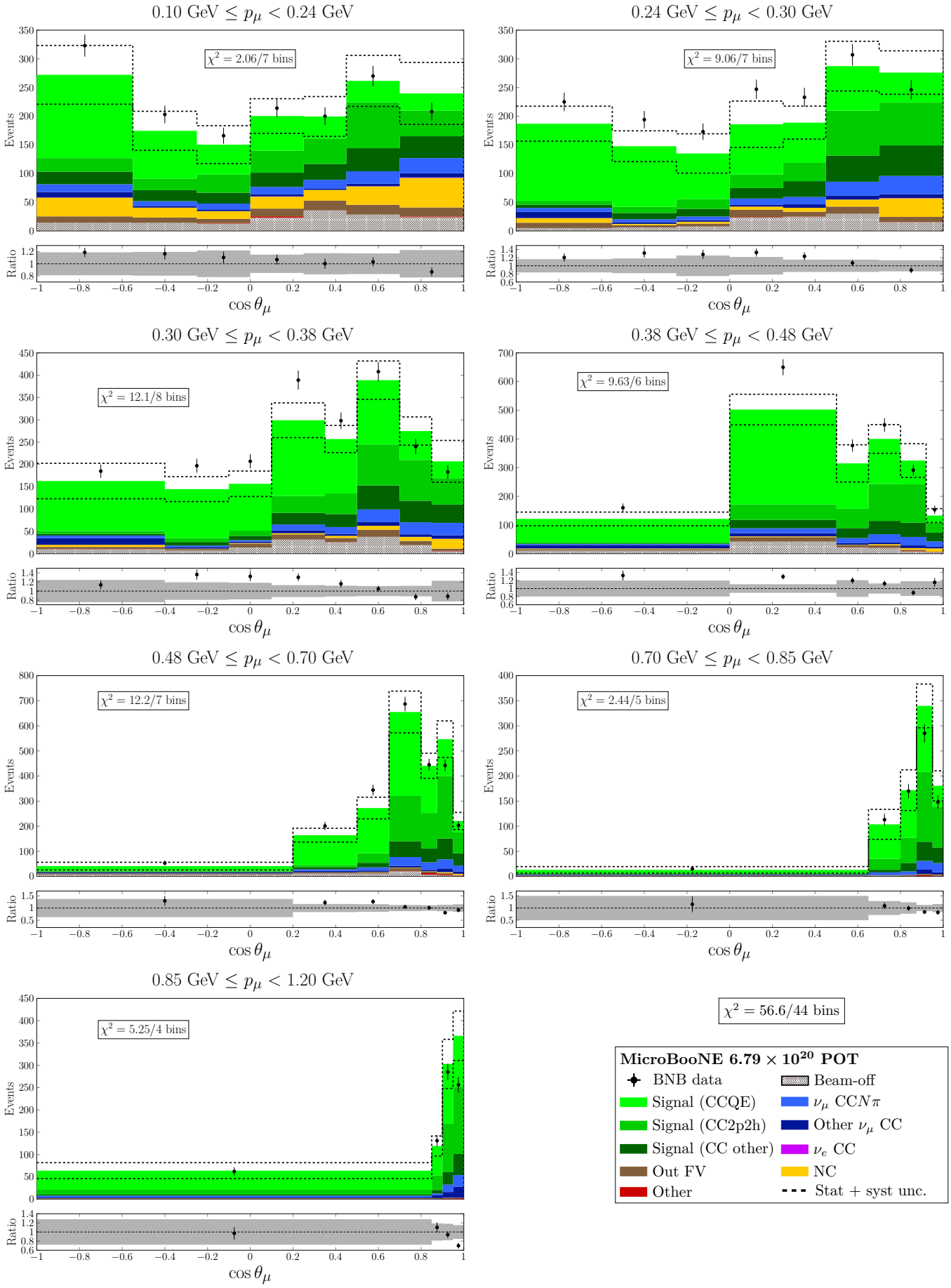

FIG. 7. Reconstructed event distributions for block #0 ($p_\mu, \cos\theta_\mu$). The bottom panel of each plot shows the ratio of the data to the MicroBooNE simulation prediction. The uncertainty on the prediction is represented by the dashed lines in each top panel and the gray region in each bottom panel.

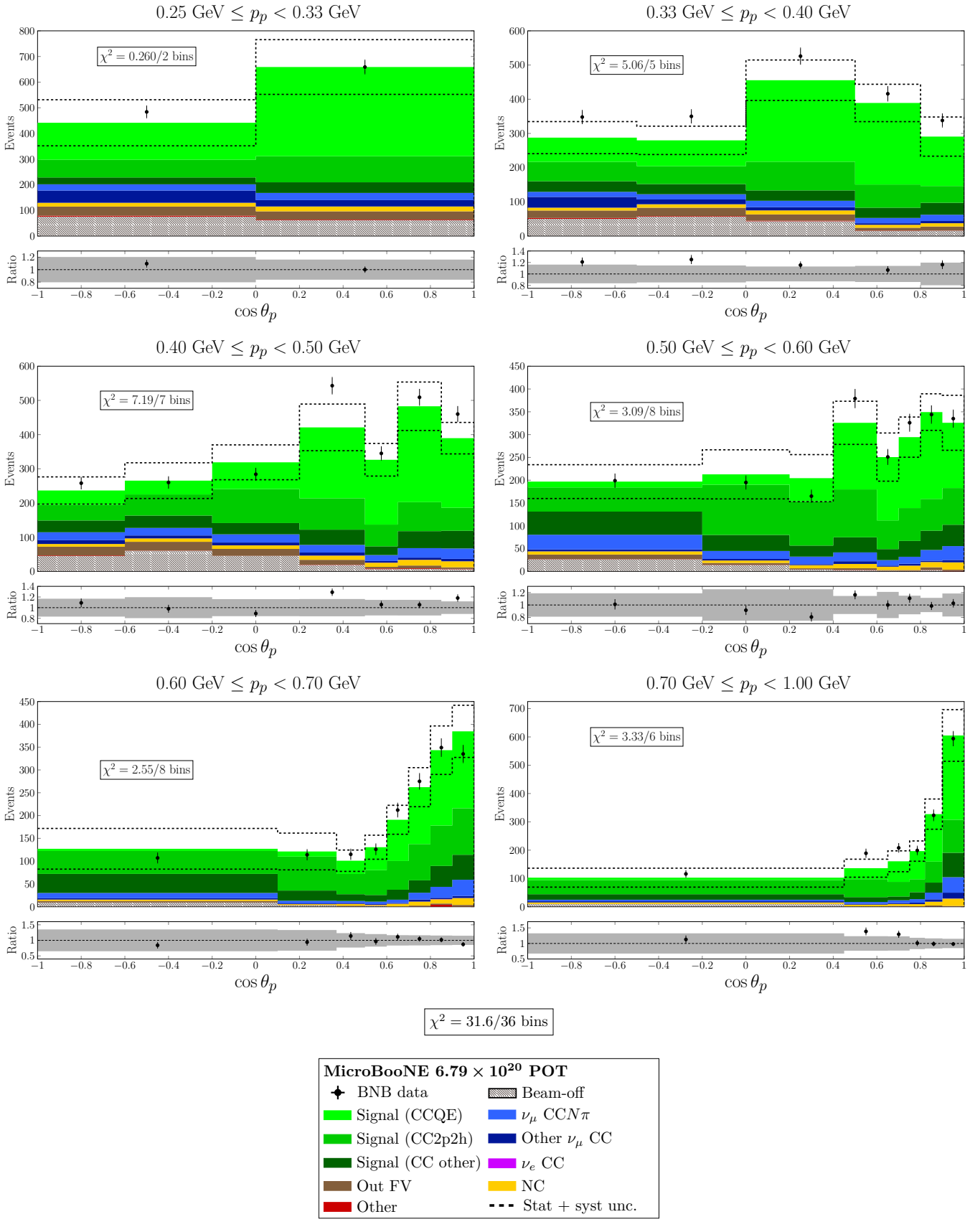

FIG. 8. Reconstructed event distributions for block #1 ($p_p, \cos\theta_p$). The bottom panel of each plot shows the ratio of the data to the MicroBooNE simulation prediction. The uncertainty on the prediction is represented by the dashed lines in each top panel and the gray region in each bottom panel.

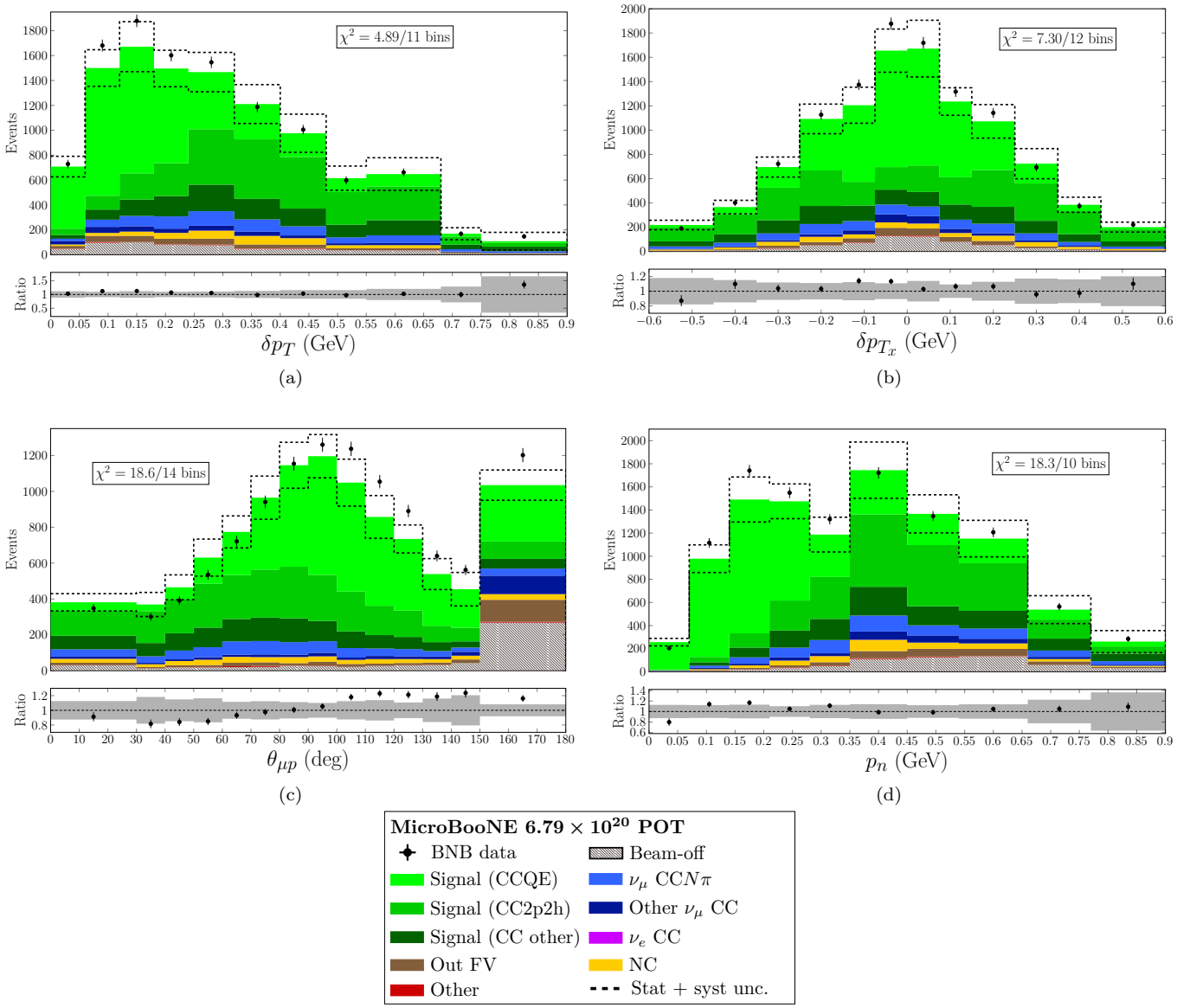

FIG. 9. Reconstructed event distributions for (a) block #2 (δp_T), (b) block #5 (δp_{T_x}), (c) block #7 ($\theta_{\mu p}$), and (d) block #8 (p_n). The bottom panel of each plot shows the ratio of the data to the MicroBooNE simulation prediction. The uncertainty on the prediction is represented by the dashed lines in each top panel and the gray region in each bottom panel.

VI. CROSS-SECTION EXTRACTION

A neutrino cross-section measurement is ultimately the result of a counting experiment: estimated backgrounds are subtracted from a measured number of events in each bin, and scaling factors are then applied to obtain a quantity with the appropriate units. Corrections to the measured event counts for detector inefficiency and bin migrations (due to imperfect reconstruction) must also be applied via a procedure called *unfolding*. Multiple standard methods for unfolding are described in terms of the matrix transformation

$$\hat{\phi}_\mu = \sum_j U_{\mu j}\, d_j \,, \tag{16}$$

where a vector of measured, background-subtracted event counts $\mathbf{d}$ is multiplied by an *unfolding matrix* U to obtain an estimator $\hat{\boldsymbol{\phi}}$ for the vector of true signal event counts. The element of $\mathbf{d}$ corresponding to the j-th reconstructed bin is given by

$$d_j = D_j - O_j - B_j \,, \tag{17}$$

where D_j is the total number of measured events in the bin, and both O_j and B_j are defined as in Eq. (13). In

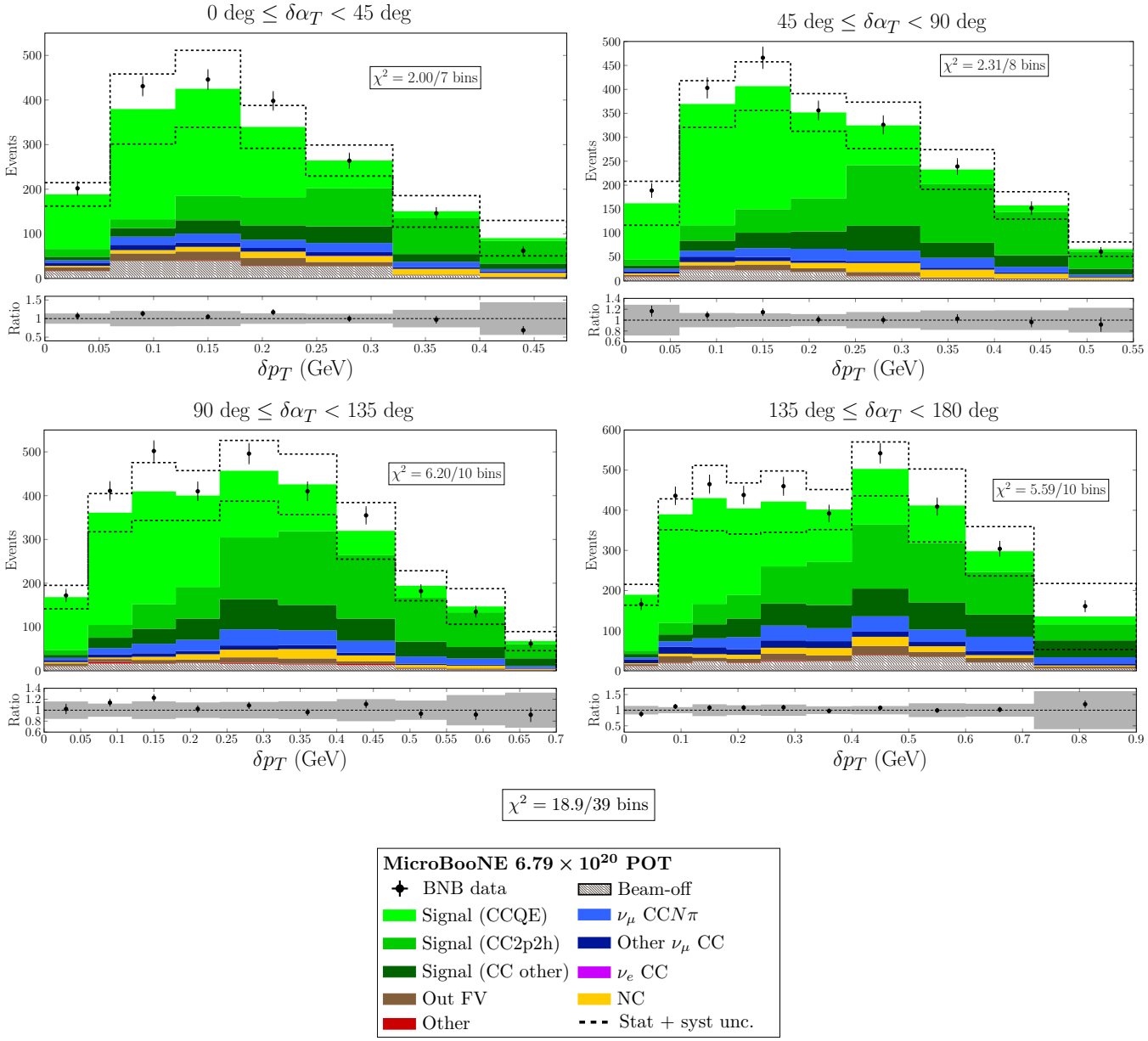

FIG. 10. Reconstructed event distributions for block #3 ($\delta\alpha_T, \delta p_T$). The overall χ^2 value includes contributions from four δp_T overflow bins that are not plotted. The bottom panel of each plot shows the ratio of the data to the MicroBooNE simulation prediction. The uncertainty on the prediction is represented by the dashed lines in each top panel and the gray region in each bottom panel.

this context, B_j is evaluated in the central-value universe. The covariance between the measured event counts in the a-th and b-th reconstructed bins is used to calculate the covariance between the unfolded event counts in the μ-th and ν-th true bins according to the relation

$$V_{\mu\nu} = \mathrm{Cov}(\hat{\phi}_\mu, \hat{\phi}_\nu) = \sum_{a,b} \mathfrak{E}_{\mu a}\, \mathrm{Cov}(d_a, d_b)\, \mathfrak{E}^T_{b\nu}\,, \qquad (18)$$

where the elements of the error propagation matrix $\mathfrak{E}$ are the partial derivatives

$$\mathfrak{E}_{\mu a} \equiv \frac{\partial \hat{\phi}_\mu}{\partial d_a}\,. \qquad (19)$$

An explicit expression for these, appropriate for this analysis, is given below in Eq. (30). The contribution of systematic uncertainties to the covariance on the background-subtracted measured event counts is estimated from the expected event counts:

$$\mathrm{Cov}(d_a, d_b) \approx \mathrm{Cov}(n_a, n_b) = V_{ab}\,, \qquad (20)$$

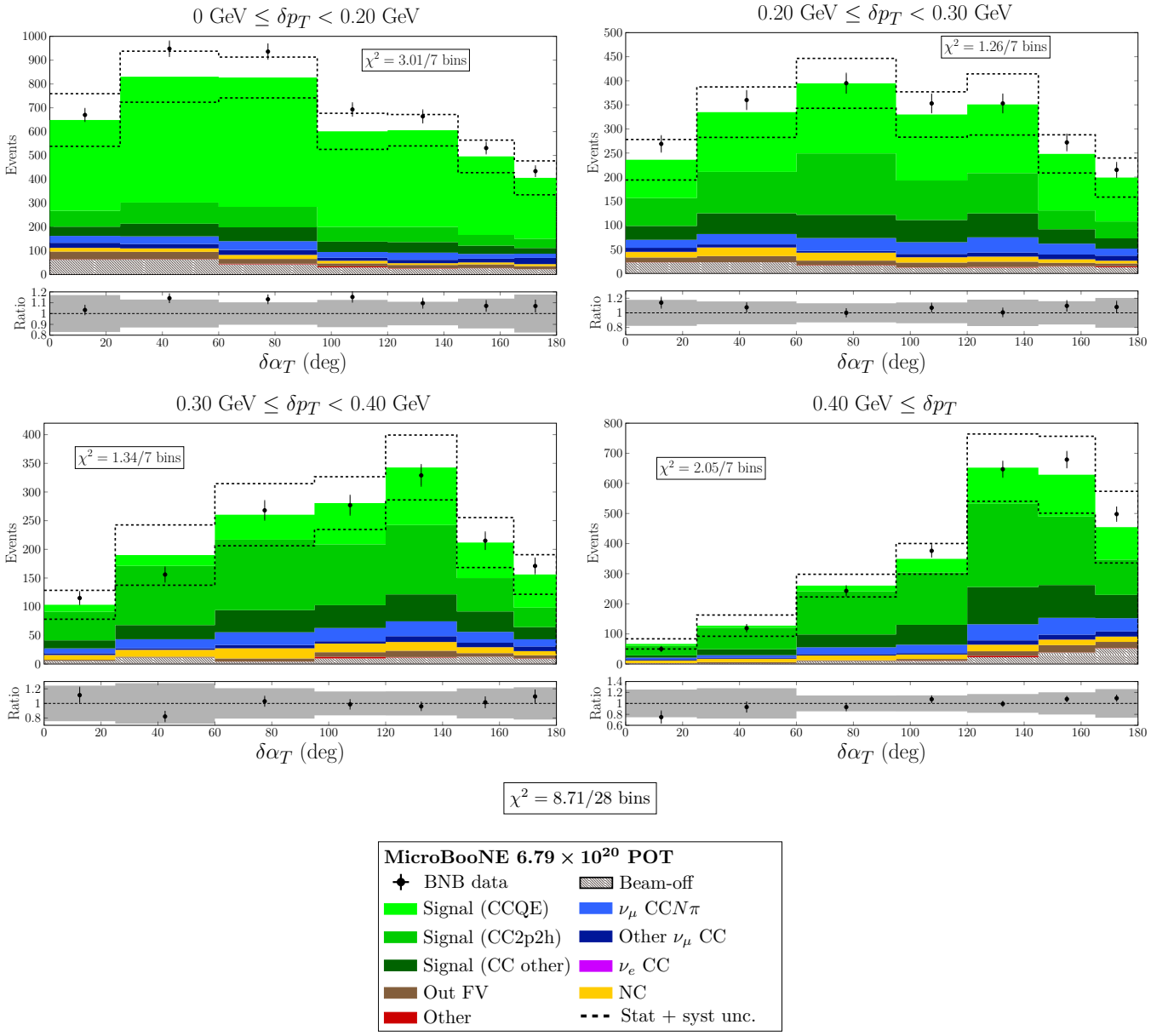

FIG. 11. Reconstructed event distributions for block #4 ($\delta p_T, \delta\alpha_T$). The bottom panel of each plot shows the ratio of the data to the MicroBooNE simulation prediction. The uncertainty on the prediction is represented by the dashed lines in each top panel and the gray region in each bottom panel.

where V_{ab} is calculated according to the prescription in Eq. (14).

A. The additional smearing matrix A_C

A simple method of unfolding is to directly invert the response matrix Δ via

$$U^{\text{direct}} = (\Delta^T \Delta)^{-1} \Delta^T . \tag{21}$$

However, in most cases of practical interest, this approach leads to strong anticorrelations between bins and large uncertainties. Overcoming these difficulties requires introducing new information (specifically, a prior prediction of the unfolded result) into the otherwise ill-posed unfolding problem. The process of adding this information is known as *regularization*. The various unfolding techniques defined in the literature differ in their prescriptions for how the regularization should be carried out.

Multiple recent MicroBooNE analyses [15, 16, 58, 59, 61, 67, 68] have used the Wiener-SVD [69] unfolding technique, which is based on an analogy with signal processing: regularization is applied using a "Wiener filter" matrix designed to mitigate "noise" arising from uncer-

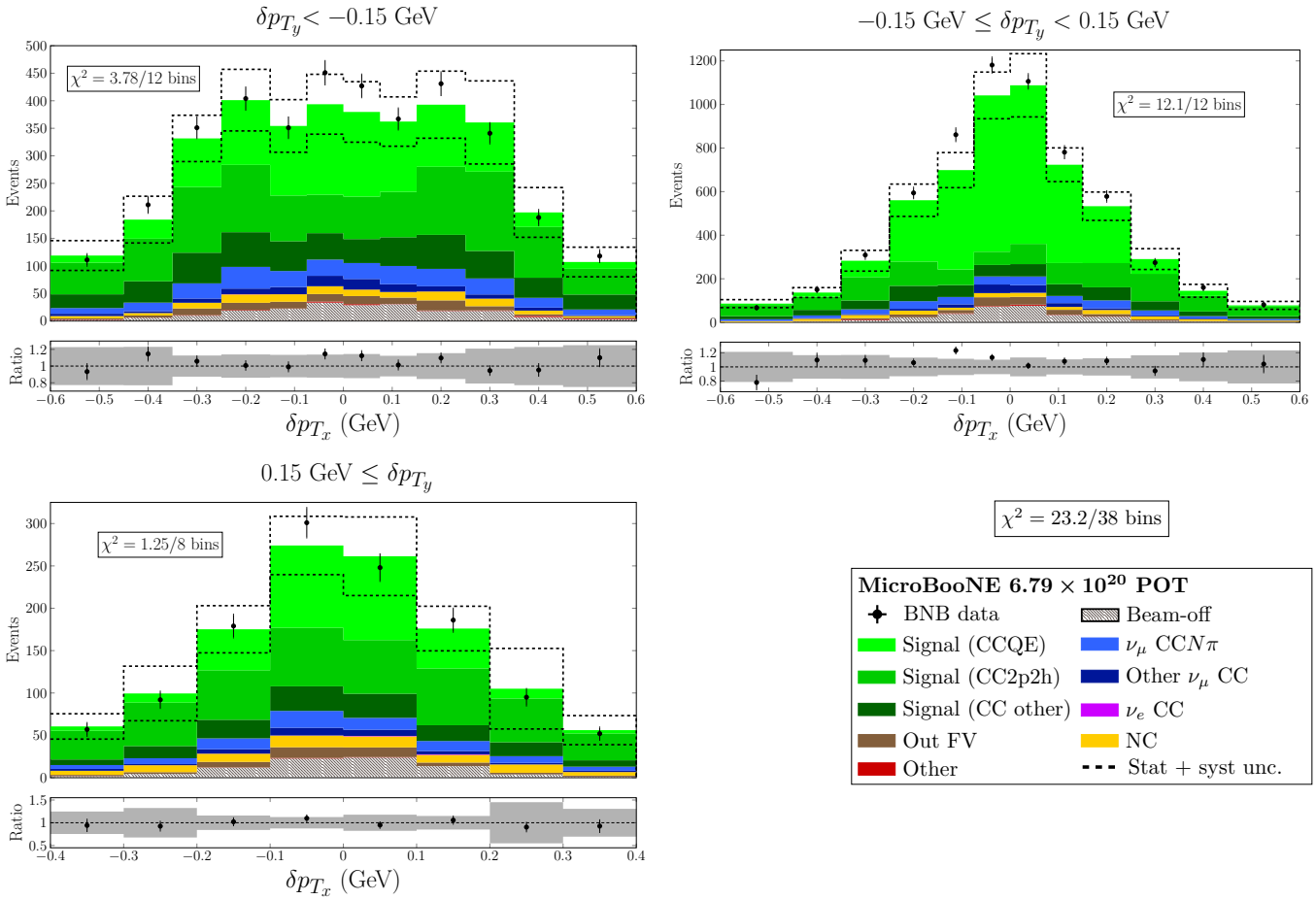

FIG. 12. Reconstructed event distributions for block #6 ($\delta p_{T_y}, \delta p_{T_x}$). The overall χ^2 value includes contributions from three underflow and three overflow δp_{T_x} bins that are not plotted. The bottom panel of each plot shows the ratio of the data to the MicroBooNE simulation prediction. The uncertainty on the prediction is represented by the dashed lines in each top panel and the gray region in each bottom panel.

tainties on the measurement. The Wiener-SVD method involves explicit construction of an *additional smearing matrix* A_C which is related to the unfolding matrix U via

$$U = A_C \cdot U^{\text{direct}} = A_C \cdot (\Delta^T \Delta)^{-1} \Delta^T . \quad (22)$$

The additional smearing matrix thus encapsulates the effect of regularization on the unfolding procedure. While an expression for A_C specific to the Wiener-SVD method is given in Eq. (3.23) of the original publication [69], it follows from the definition in Eq. (22) that A_C may be calculated for an arbitrary unfolding method via

$$A_C = U \cdot \Delta . \quad (23)$$

Reference [69] also describes a method to avoid introducing new measurement uncertainties related to the unfolding procedure itself. By multiplying theoretical predictions by A_C before comparisons are made to the unfolded results, the effects of regularization-related bias on the measurement are properly taken into account. This prescription is followed herein: all model predictions are multiplied by A_C when comparisons are made to the unfolded data. The A_C matrix elements needed to compare the final measurements to new theoretical predictions are provided in the supplemental materials.

B. D'Agostini iterative unfolding

The present work adopts an iterative method of unfolding popularized in high-energy physics by D'Agostini [70]. An initial estimate for the unfolded event counts (iteration $i = 0$) is obtained from the central-value prediction of the MicroBooNE simulation in the true bins:

$$\hat{\phi}^0_\mu = \phi^{\text{CV}}_\mu . \quad (24)$$

Superscripts on $\hat{\phi}$ and related quantities are used to denote the number of iterations. Subsequent iterations of the method are used to refine the initial estimate using the measured event rates in each reconstructed bin. This

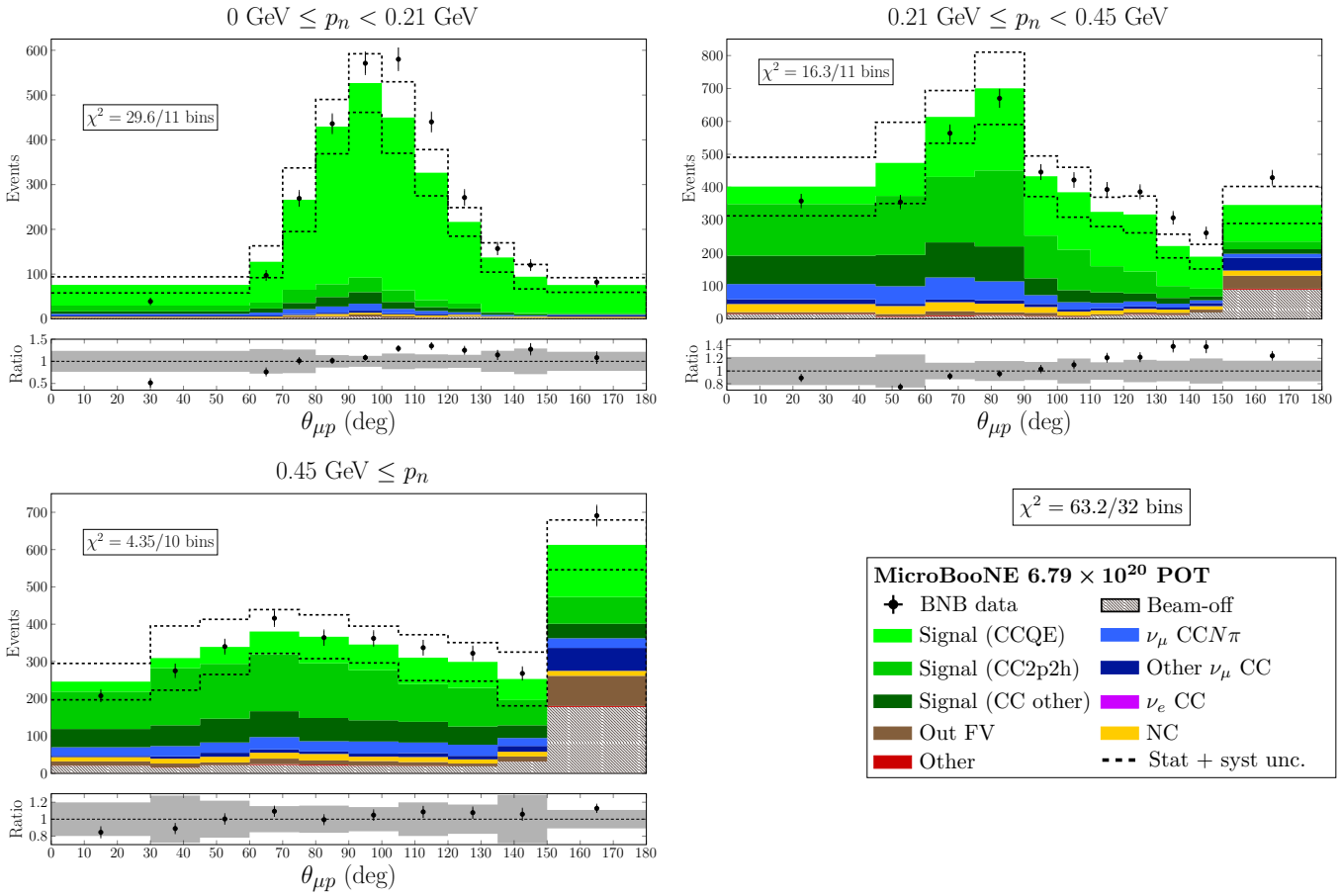

FIG. 13. Reconstructed event distributions for block #9 $(p_n, \theta_{\mu p})$. The bottom panel of each plot shows the ratio of the data to the MicroBooNE simulation prediction. The uncertainty on the prediction is represented by the dashed lines in each top panel and the gray region in each bottom panel.

is done via the formula

$$\hat{\phi}_\mu^{i+1} = \sum_j U_{\mu j}^i \, d_j \, . \tag{25}$$

where the unfolding matrix element

$$U_{\mu j}^i = \frac{P_{j\mu}^i}{\epsilon_\mu} \tag{26}$$

is defined in terms of the selection efficiency in the μ-th true bin

$$\epsilon_\mu = \sum_\ell \Delta_{\ell\mu} \tag{27}$$

and the conditional probability that a signal event which belongs to the μ-th true bin will be assigned to the j-th reconstructed bin

$$P_{j\mu}^i = \frac{\Delta_{j\mu} \, \hat{\phi}_\mu^i}{\sum_\nu \Delta_{j\nu} \, \hat{\phi}_\nu^i} \, . \tag{28}$$

Because the unfolding matrix depends on the measured event counts for iterations $i > 0$, the error propagation matrix elements needed to evaluate uncertainties on the unfolded result

$$V_{\mu\nu}^i = \mathrm{Cov}(\hat{\phi}_\mu^i, \hat{\phi}_\nu^i) = \sum_{a,b} \mathfrak{E}_{\mu a}^i \, \mathrm{Cov}(d_a, d_b) \, \mathfrak{E}_{\nu b}^i \tag{29}$$

are given by [71, 72]

$$\mathfrak{E}_{\mu a}^{i+1} = \frac{\partial \hat{\phi}_\mu^{i+1}}{\partial d_a} = U_{\mu a}^i + \frac{\hat{\phi}_\mu^{i+1}}{\hat{\phi}_\mu^i} \mathfrak{E}_{\mu a}^i - \sum_{\nu,b} \epsilon_\nu \frac{d_b}{\hat{\phi}_\nu^i} \, U_{\mu b}^i \, U_{\nu b}^i \, \mathfrak{E}_{\nu a}^i \, . \tag{30}$$

For the first iteration, this reduces to

$$\mathfrak{E}_{\mu a}^1 = U_{\mu a}^0 \tag{31}$$

since the central-value prediction of the MicroBooNE simulation does not depend on the data:

$$\mathfrak{E}_{\mu a}^0 = \frac{\partial \hat{\phi}_\mu^0}{\partial d_a} = \frac{\partial \phi_\mu^{\mathrm{CV}}}{\partial d_a} = 0 \, . \tag{32}$$

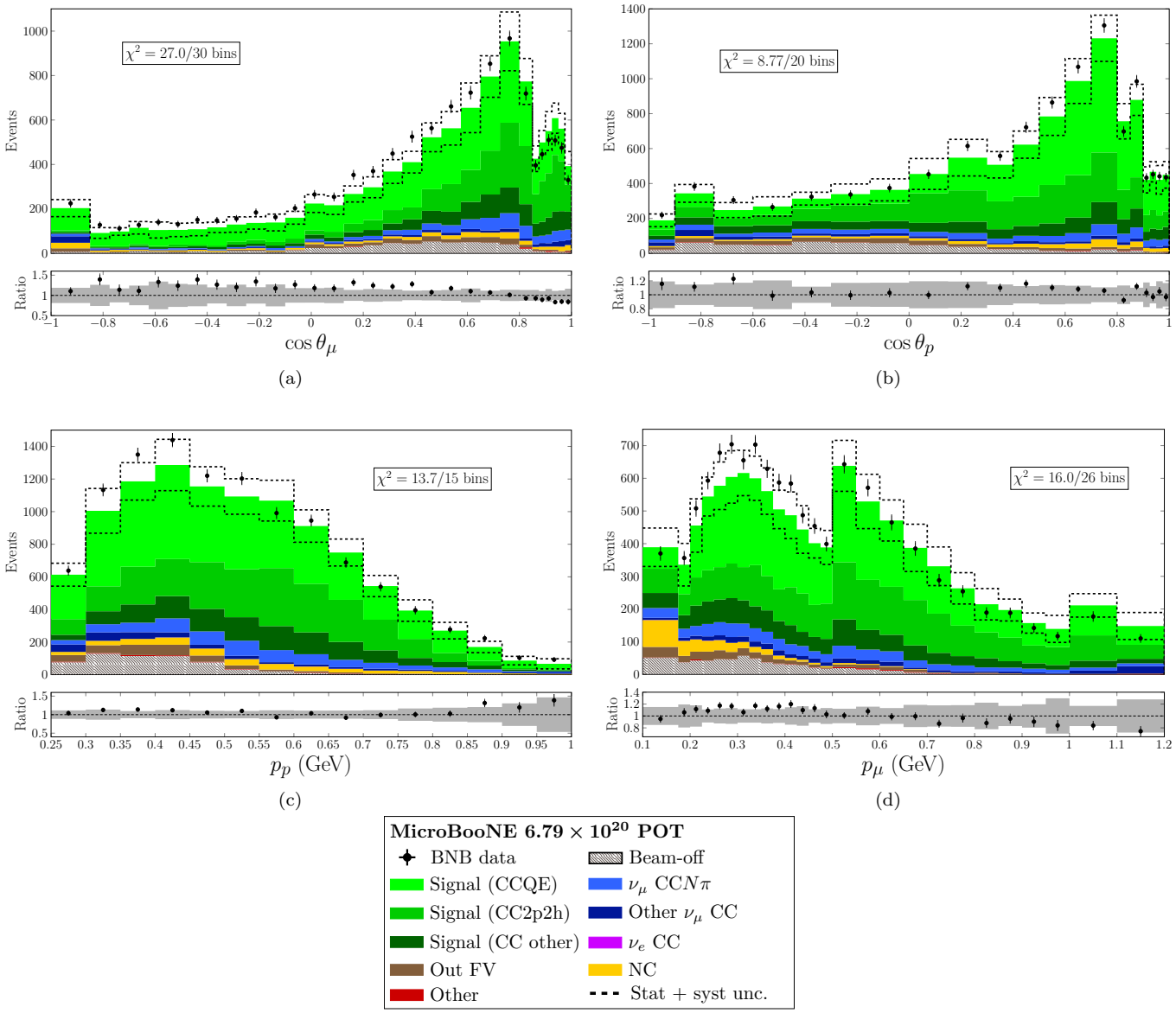

FIG. 14. Reconstructed event distributions for (a) block #10 ($\cos\theta_\mu$), (b) block #11 ($\cos\theta_p$), (c) block #12 (p_p), and (d) block #13 (p_μ). The bottom panel of each plot shows the ratio of the data to the MicroBooNE simulation prediction. The uncertainty on the prediction is represented by the dashed lines in each top panel and the gray region in each bottom panel.

C. Convergence criterion for unfolding iterations

In the limit of many iterations, the D'Agostini approach converges to the direct inversion result discussed in Sec. VI A. Regularization is thus applied by stopping the method at a finite number of iterations.

Traditionally, the choice of the number of iterations to use in the D'Agostini unfolding method is a critical step of an analysis: one must iterate enough times to avoid a strong bias towards the initial estimate $\hat{\phi}_\mu^0$ for the true event distribution without approaching the direct inversion result too closely. These concerns are addressed in this article by multiplying theoretical predictions by the additional smearing matrix A_C before comparing them to the unfolded data. The implicit regularization in the D'Agostini method is thus applied to the predictions in a consistent way, avoiding the need to introduce new unfolding-related systematic uncertainties.

Nevertheless, even while using A_C, one must choose a definite number of iterations in order to unfold via the D'Agostini approach. In this analysis, the choice is made by continuing to iterate until the average fractional deviation $\mathfrak{F}$ in the T true bins

$$\mathfrak{F} \equiv \frac{1}{T}\sum_\mu \frac{\left|\hat{\phi}_\mu^{i+1} - \hat{\phi}_\mu^{i}\right|}{\hat{\phi}_\mu^{i+1}} \tag{33}$$

between neighboring iterations falls below 2.5%. This cutoff was chosen empirically based on the unfolding performance in fake data studies and the observation that fluctuations of the bin counts at this level will be well-covered by typical systematic uncertainties. The fake data studies used to validate the unfolding procedure treated the prediction in the NuWro alternate universe (see Sec. V A) as if it were real data. Recovery of the known true bin counts ϕ_μ predicted by NuWro was verified within the relevant subset of the uncertainties, i.e., only the Monte Carlo statistical and neutrino interaction model systematic uncertainties were included.

D. Blockwise unfolding

The convergence criterion discussed in Sec. VI C leads to between two and five iterations being used to unfold each individual block of bins.

To avoid the double-counting issues mentioned in Sec. IV (e.g., an incorrect calculation of the selection efficiency from the elements of the response matrix Δ), the sums in Eqs. (27)–(30) and Eq. (33) should be understood to include only true and reconstructed bins within the same block. Also, since Eq. (33) is intended to be an average, T should be interpreted as the number of true bins in the block of interest.

An overall unfolding matrix U used according to Eq. (16) to obtain final results involving all bins is constructed as the direct sum of the blockwise unfolding matrices:

$$U = \bigoplus_b U_b = U_0 \oplus U_1 \oplus \cdots = \begin{pmatrix} U_0 & 0 & 0 & \dots \\ 0 & U_1 & 0 & \dots \\ 0 & 0 & \ddots & \dots \\ \vdots & \vdots & \vdots & \ddots \end{pmatrix} . \quad (34)$$

Here U_b is the unfolding matrix for the b-th block of true and reconstructed bins. A similar direct sum is calculated to build the combined error propagation matrix needed to evaluate the unfolded covariance matrix in Eq. (18):

$$\mathfrak{E} = \bigoplus_b \mathfrak{E}_b = \mathfrak{E}_0 \oplus \mathfrak{E}_1 \oplus \dots \quad (35)$$

E. Decomposition of the blockwise covariance matrices

The covariance matrix $V_{\mu\nu}$ describing the unfolded event counts $\hat{\phi}_\mu$ and $\hat{\phi}_\nu$ (see Eq. (18)) for an individual block of bins can be decomposed into components representing normalization-only, shape-only, and mixed uncertainties according to the relations [73]

$$V_{\mu\nu} = V_{\mu\nu}^{\text{norm}} + V_{\mu\nu}^{\text{shape}} + V_{\mu\nu}^{\text{mixed}} \quad (36)$$

$$V_{\mu\nu}^{\text{norm}} = \frac{\hat{\phi}_\mu \hat{\phi}_\nu}{\hat{\phi}_{\text{tot}}^2} \sum_{\alpha\beta} V_{\alpha\beta} \quad (37)$$

$$V_{\mu\nu}^{\text{mixed}} = \frac{\hat{\phi}_\mu}{\hat{\phi}_{\text{tot}}} \sum_\alpha V_{\alpha\nu} + \frac{\hat{\phi}_\nu}{\hat{\phi}_{\text{tot}}} \sum_\alpha V_{\mu\alpha} - 2V_{\mu\nu}^{\text{norm}} \quad (38)$$

where

$$\hat{\phi}_{\text{tot}} \equiv \sum_\alpha \hat{\phi}_\alpha \, , \quad (39)$$

and the sums are understood to include all true bins belonging to the block of interest and no others. Note that the same formulas cannot be meaningfully applied to the multi-block covariance matrix due to double-counting when computing the total number of events in Eq. (39). This decomposition of the covariance matrix is used when presenting cross-section results for individual blocks of bins in Sec. VII B.

F. Calculation of differential cross sections

The unfolded event counts $\hat{\phi}_\mu$ from the final iteration provide an estimator for the true number of signal events in the μ-th bin. They may be converted to a flux-averaged differential cross section according to the formula

$$\left\langle \frac{d^n\sigma}{d\mathbf{x}} \right\rangle_\mu = \frac{\hat{\phi}_\mu}{\Phi \, \mathcal{N}_{\text{Ar}} \, \Delta\mathbf{x}_\mu} \quad (40)$$

where $\Phi = 5.00846 \times 10^{11}$ ν_μ /cm^2 is the integrated flux of muon neutrinos calculated for the beam exposure (6.79×10^{20} POT) used in the analysis, $\mathcal{N}_{\text{Ar}} = 7.99249 \times 10^{29}$ is the number of argon nuclei in the fiducial volume, and $\Delta\mathbf{x}_\mu$ is the product of the n widths of the μ-th bin of the n-dimensional measurement.

The covariance between the n- and m-dimensional differential cross sections in the μ-th and ν-th true bins is likewise given by

$$\text{Cov}\left(\left\langle \frac{d^n\sigma}{d\mathbf{x}} \right\rangle_\mu , \left\langle \frac{d^m\sigma}{d\mathbf{y}} \right\rangle_\nu \right) = \frac{\text{Cov}(\hat{\phi}_\mu, \hat{\phi}_\nu)}{\Phi^2 \, \mathcal{N}_{\text{Ar}}^2 \, \Delta\mathbf{x}_\mu \, \Delta\mathbf{y}_\nu} \, . \quad (41)$$

VII. RESULTS

The measurements shown in the remainder of this article are flux-averaged differential CC0πNp cross sections obtained via the unfolding procedure presented above. Several event generator predictions are compared to the data using NUISANCE [74], and goodness-of-fit is quantified for the data set as a whole and for the individual blocks of kinematic bins listed in Table III.

In Sec. I of the supplemental materials, the full 359-bin data set is presented in terms of flux-averaged total

cross sections integrated over each bin (trivially obtainable by multiplying by the bin widths $\Delta \mathbf{x}_\mu$). This allows the measured cross sections and the covariance matrix elements for all observables to be expressed using consistent units.

A. Interaction models

In addition to the MicroBooNE Tune model described in Sec. II A and used to execute the analysis, the predictions of several other simulation-based neutrino interaction models are compared to the measured cross-section results. These models include multiple configurations of GENIE as well as three alternative neutrino event generators.

The GENIE-based prediction labeled *GENIE 3.0.6* is produced using the same code version and model set (`G18_10a_02_11a`) as the MicroBooNE Tune, but the custom MicroBooNE-specific modifications described in Ref. [11] are omitted. The *GENIE 2.12.10* prediction uses a near-default configuration of this older version of the code, which includes the Bodek-Ritchie Fermi gas description of the nuclear ground state [75], the Llewellyn Smith CCQE calculation [76], an empirical model for 2p2h interactions [77], the Rein-Sehgal treatment of RES and COH scattering [78], and the hA FSI model [79, 80]. The modeling ingredients in *GENIE 3.2.0 G18_02a*, which uses the default configuration (*G18_02a_00_000*) of this recent GENIE release, are largely similar to GENIE 2.12.10. In addition to code updates, however, the KLN-BS RES model [29–32], Berger-Sehgal COH model [36], and hA2018 FSI model [37] replace their prior counterparts. A final configuration, *GENIE 3.2.0 G21_11b*, uses the more recently-added `G21_11b_00_000` model set, which adopts the SuSAv2 calculation [81–84] of CCQE and 2p2h cross sections as well as the hN2018 FSI model [37]. The remaining components of the model set are similar to GENIE 3.0.6.

The first prediction of an alternate neutrino event generator, *NuWro 19.02.2*, uses the NuWro [64] implementations of the LFG nuclear ground state [23], the Llewellyn Smith CCQE model [76], the Valencia CC2p2h model [27, 28], the Adler-Rarita-Schwinger treatment of Δ resonance production [32], the Berger-Sehgal COH model [36] and an intranuclear cascade approach to FSI. A comparison to *NEUT 5.6.0* is also provided, in which the NEUT event generator [85, 86] is configured to use an LFG nuclear model [23], the Valencia model for CCQE and 2p2h [24–28], the KLN-BS RES calculation [29–32], the Berger-Sehgal COH model [36], and an FSI cascade treatment with nuclear medium corrections for pions [87].

Finally, a prediction from the GiBUU event generator [88] (labeled *GiBUU 2021.1*) is studied using the 2021 "patch 1" release of the code announced to users on 5 November 2021. Ingredients of the GiBUU physics model include an LFG representation of the nuclear ground state [23], a standard expression for the neutrino-nucleon CCQE cross section [89], an empirical 2p2h model, a treatment of RES based upon the MAID analysis [90], and a DIS model from PYTHIA [91]. A unique feature of the code is its dynamical model of intranuclear hadron transport based upon numerical solution of the Boltzmann-Uehling-Uhlenbeck equation. A consistent nuclear potential is used in both the description of the target nucleus and FSI.

The χ^2 metric used to assess goodness-of-fit when comparing these models to data accounts for the total covariance matrix associated with the measurements but neglects any theoretical uncertainties on the predictions themselves. Documentation needed to enable new comparisons beyond those shown here is provided in Sec. I of the supplemental materials. The data set from this article has also recently been incorporated into the NUISANCE [74] software framework for convenient use by the neutrino interaction modeling community.

B. Differential cross-section results

Figures 15 to 28 present the final results of the analysis as flux-averaged differential cross sections. The measurements are compared to the event generator models described above, each rendered in the plots as a distinct colored line. The legends accompanying each figure list the models together with their overall χ^2 scores describing the level of agreement with data. Each χ^2 score is separated from the number of bins for which it was calculated by a / character. A separate figure is included for each block of bins defined in Table III.

Following recent MicroBooNE publications that report cross sections for an exclusive single-proton final state [58, 59, 61], the covariance matrix decomposition described in Sec. VI E is applied when displaying the measurement uncertainties. For the data points shown in each plot, the inner error bars represent the statistical uncertainty only, while the outer error bars also include shape-only systematic uncertainties. The remaining portion of the total uncertainty, composed of both normalization and mixed terms, is shown by the gray band along the x-axis.

Table II presents the χ^2 scores quantifying goodness-of-fit with the full group of measurements for each of the event generator models studied. None of the simulation predictions provides a satisfactory treatment of the entire data set ($\chi^2 \approx 1$/bin). The best χ^2 value is obtained by the GENIE 3.0.6 calculation, although poor agreement is seen between this model and the data in some of the individual blocks of bins, and its prediction is seen to be systematically low across the entire measured phase space. The modest preference for GENIE 3.0.6 may thus be attributed to a manifestation of Peelle's Pertinent Puzzle [92] (in which implausibly low predictions are favored using a least-squares metric like χ^2) rather than a particularly high-quality description of the data. The substantially larger χ^2 values seen for GENIE 2.12.10 and

GENIE 3.2.0 G18_02a, however, do suggest that some of their common model components (e.g., a global rather than local Fermi gas description of the nuclear ground state) are disfavored by the present measurements. As shown in the plots below, GiBUU 2021.1 has the best χ^2 score for many of the individual blocks of bins despite performing more poorly when confronted with the combined results.

TABLE II. Overall χ^2 scores for each of the neutrino interaction models studied.

Model	χ^2 / 359 bins
GENIE 3.0.6	1859
NEUT 5.6.0	2582
MicroBooNE Tune	2673
GENIE 3.2.0 G21_11b	2947
GiBUU 2021.1	4836
NuWro 19.02.1	5315
GENIE 3.2.0 G18_02a	5724
GENIE 2.12.10	7799

Figure 15 presents the double-differential cross-section measurement in terms of muon momentum (p_μ) and scattering angle (θ_μ) obtained using the kinematic bins from block #0. The GiBUU 2021.1 model achieves the best agreement with this distribution, partially due to its larger cross section relative to most of the other plotted models in the region of moderate p_μ (especially between 0.3 and 0.38 GeV/c) and intermediate scattering angles. Interestingly, the data are compatible with an even larger cross section in this region, to the extent that all studied predictions lie noticeably below the measured central value in several relevant bins.

Figure 16 presents the double-differential cross-section measurement in terms of the leading proton momentum (p_p) and scattering angle (θ_p) obtained using the bins from block #1. At low p_p, the NuWro 19.02.2 calculation markedly undershoots the data, particularly at forward proton angles. However, this model prediction becomes more similar to the others with increasing p_p, as can also be seen in the single-differential p_p results shown in Fig. 27. Significant model differences are seen in the shape of the forward-angle region at relatively high p_p, but the systematic uncertainty of the present measurement allows for only limited sensitivity to these details.

Figure 17 shows the single-differential cross section in the transverse momentum imbalance δp_T as obtained from the analysis bins in block #2. A clear preference in the χ^2 values is seen for models which can simultaneously provide a relatively good treatment of the low-δp_T region (dominated by CCQE events without proton FSI) and the high-δp_T tail (dominated by more inelastic events and CCQE with FSI). Notably, two of the event generator models that show the poorest agreement with this distribution, NuWro 19.02.2 and GENIE 3.2.0 G18_02a, have their greatest tension with the data in opposite kinematic regions corresponding to high- and low-δp_T, respectively.

A double-differential result in which the δp_T measurement is sub-divided into four $\delta\alpha_T$ bins (as defined in block #3) is plotted in Fig. 18. Here the NuWro 19.02.2 model shows good agreement with data in the lowest $\delta\alpha_T$ region, which gradually worsens with increasing $\delta\alpha_T$. A similar trend is seen in Fig. 12 of Ref. [58], which reports a similar MicroBooNE measurement studying a more exclusive single-proton final state. Because the effect of FSI is to make the $\delta\alpha_T$ distribution more asymmetric and weighted towards high values [58, 93], these results may indicate an underestimation of proton FSI in the NuWro 19.02.2 configuration considered herein. The GENIE 3.2.0 G18_02a model, on the other hand, shows a roughly consistent deficit in the lowest δp_T bins across all $\delta\alpha_T$ values, which is suggestive of missing CCQE strength. Similar conclusions follow from Fig. 19, in which the bins from block #4 are used to report a measurement of double-differential $\delta\alpha_T$ distributions in four coarse bins of δp_T.

Figure 20 presents a single-differential cross-section measurement in δp_{T_x}, the component of $\delta\mathbf{p}_T$ that is orthogonal to the transverse projection of the outgoing muon momentum. The GiBUU 2021.1 and NEUT 5.6.0 models provide particularly good predictions for this observable, which follows a distribution that is nearly symmetric around zero. Figure 21 subdivides this measurement into three coarse bins of δp_{T_y}, the other component of $\delta\mathbf{p}_T$. Here the effects of FSI enhance the cross section in the region where δp_{T_y} is negative. The strong deficit seen in the NuWro 19.02.2 prediction in the lowest δp_{T_y} bin is thus symptomatic of the same modeling deficiencies seen previously at high values of δp_T and $\delta\alpha_T$.

Figure 22 displays the measured single-differential CC0πNp cross section in bins of $\theta_{\mu p}$, the opening angle between the outgoing muon and leading proton. Although all of the interaction models studied in this article agree on the rough shape of this angular distribution, the position of the peak is sensitive to the relative contributions of QE and 2p2h events, as seen in the lower-left panel of Fig. 9. The data points provide a peak location that is shifted slightly to the right of the bulk of the event generator predictions, with NEUT 5.6.0 and especially GiBUU 2021.1 achieving the best agreement.

Figure 23 reports the measured distribution of p_n, a three-dimensional analog of δp_T which includes the component of missing momentum δp_L longitudinal to the neutrino beam. The addition of this new direction noticeably worsens the χ^2/bin for all models studied, particularly for GENIE 2.12.10 and NEUT 5.6.0, although the latter still achieves the second-best χ^2 score. When one considers the single-differential cross section for p_n in isolation, the GiBUU 2021.1, GENIE 3.2.0 G21_11b, and MicroBooNE Tune models also describe the data fairly well (χ^2/bin < 1) despite using distinct theoretical treatments of both the QE and 2p2h interaction modes.

Figure 24 presents double-differential cross sections as a function of $\theta_{\mu p}$ in three bins of p_n. Here the prefer-

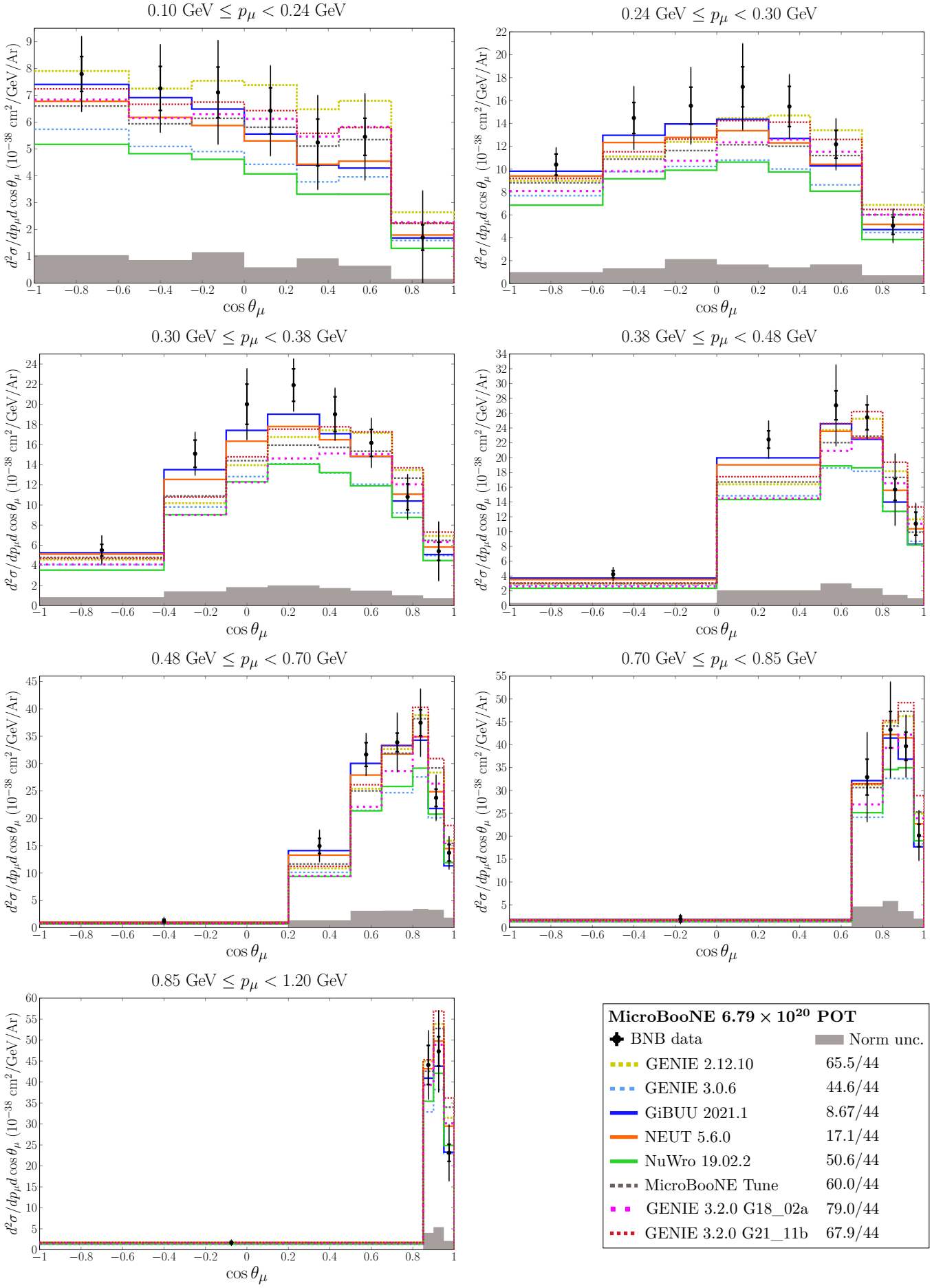

FIG. 15. Measured differential cross sections for block #0 ($p_\mu, \cos\theta_\mu$). Statistical (shape-only systematic) uncertainties are included in the inner (outer) error bars. The remainder of the total uncertainty is shown by the gray band along the x-axis.

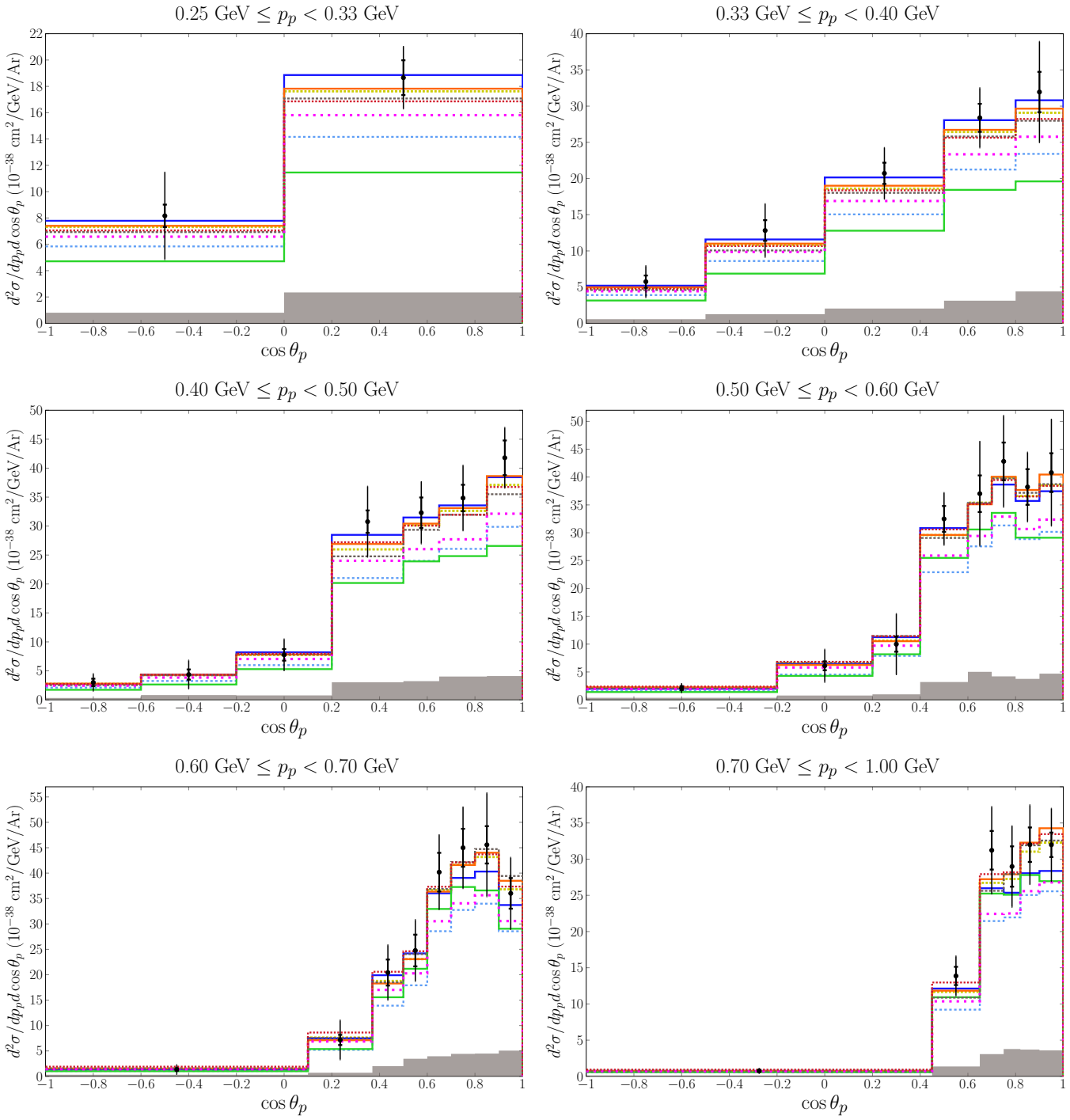

FIG. 16. Measured differential cross sections for block #1 $(p_p, \cos\theta_p)$. Statistical (shape-only systematic) uncertainties are included in the inner (outer) error bars. The remainder of the total uncertainty is shown by the gray band along the x-axis.

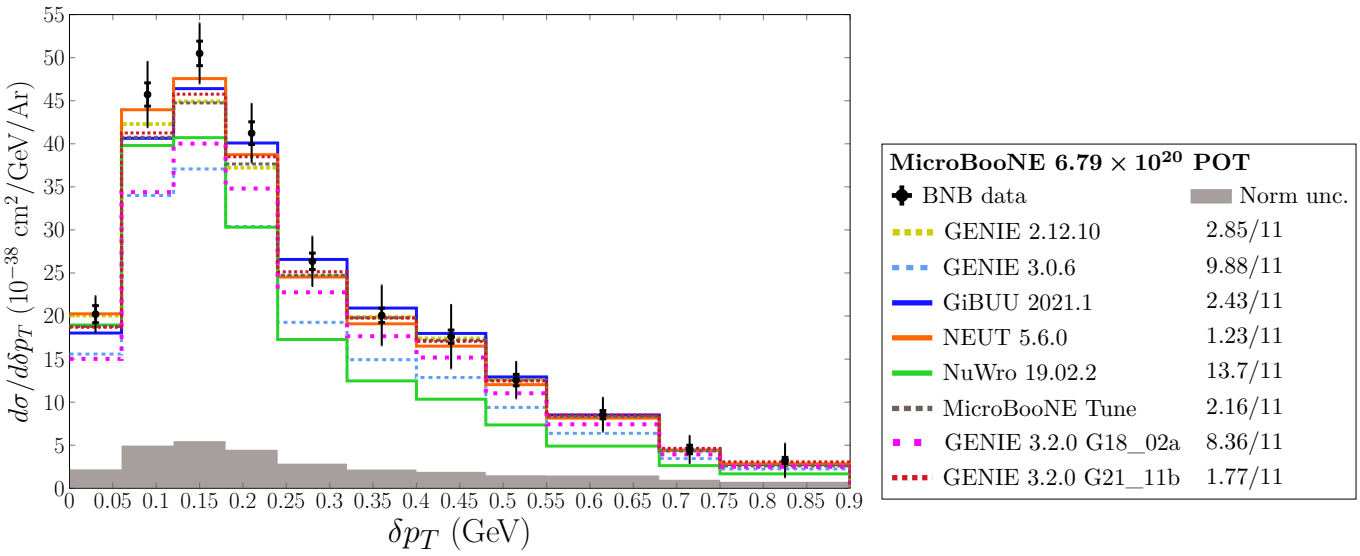

FIG. 17. Measured differential cross sections for block #2 (δp_T). Statistical (shape-only systematic) uncertainties are included in the inner (outer) error bars. The remainder of the total uncertainty is shown by the gray band along the x-axis.

ence for the peak location predicted by GiBUU 2021.1 in Fig. 22 is partially explained by this model's remarkably good description of the data in the bin of moderate p_n (0.21 GeV/c to 0.45 GeV/c). As shown in Fig. 13, this is also the kinematic region in which differences in the relative contributions of QE and 2p2h events have the greatest impact on the shape of the $\theta_{\mu p}$ distribution. Although it obtains one of the larger χ^2 values for this group of bins (block #9), the NuWro 19.02.2 model provides nearly the best agreement ($\chi^2 = 3.85/11$ bins) in the QE-dominated region of $p_n < 0.21$ GeV/c. Only the NEUT 5.6.0 model achieves slightly better performance ($\chi^2 = 3.32/11$ bins) for this region of phase space.

Figure 25 shows the measured single-differential cross section as a function of the muon scattering angle θ_μ. The lowest χ^2 values obtained by GiBUU 2021.1 and NEUT 5.6.0 can be attributed to two features of these model predictions. First, the data favor significantly more cross-section strength in the $\cos\theta_\mu \lesssim 0.4$ region than is predicted by the majority of the studied event generators. Here the GiBUU 2021.1 and NEUT 5.6.0 predictions are noticeably higher than the others. A similar tendency for models to underpredict data in this angular region has also been seen in recent MicroBooNE cross-section results for quasielastic-like interactions [58] and inclusive charged-current ν_μ scattering with at least one proton in the final state [16]. Second, both GiBUU 2021.1 and NEUT 5.6.0 provide a good description within uncertainties of the forward-angle region ($\cos\theta_\mu \gtrsim 0.8$), although GiBUU 2021.1 lies substantially closer to the measured data point in the most-forward bin.

Finally, Figs. 26, 27, and 28 present measured single-differential cross sections in terms of the leading proton scattering angle (θ_p), leading proton momentum (p_p), and muon momentum (p_μ), respectively. For all three distributions, GiBUU 2021.1 provides the best quantitative agreement with the data, driven in part by its prediction of a higher CC0πNp cross section at moderate proton scattering angles ($\cos\theta_p \in [0, 0.6]$), low proton momenta ($p_p < 0.5$ GeV/c) and moderate muon momenta ($p_\mu \in [0.25, 0.5]$ GeV/c).

For the single-differential p_μ and p_p results, similar trends can be seen in MicroBooNE data for inclusive CC ν_μ events with one or more final-state protons [16]. For both the CC0πNp cross sections shown here and the inclusive results, data indicate a higher cross section near the peak of the p_μ distribution than is predicted by a variety of neutrino event generators, and models with a larger prediction at low p_p are also preferred.

VIII. SUMMARY AND CONCLUSIONS

This article presents a detailed study of charged-current muon-neutrino interactions with argon leading to mesonless final states containing one or more protons. Flux-averaged cross sections for this CC0πNp process were measured using the Fermilab Booster Neutrino Beam and MicroBooNE detector. The results are reported as a function of ten observables related to the three-momenta of the outgoing muon and leading proton. A larger data set and significant improvements to MicroBooNE's software tools since the experiment's first CC0πNp cross-section analysis was reported [10] allow the present work to achieve higher precision and explore new kinematic distributions, including the first double-differential measurements in the CC0πNp channel for an argon target.

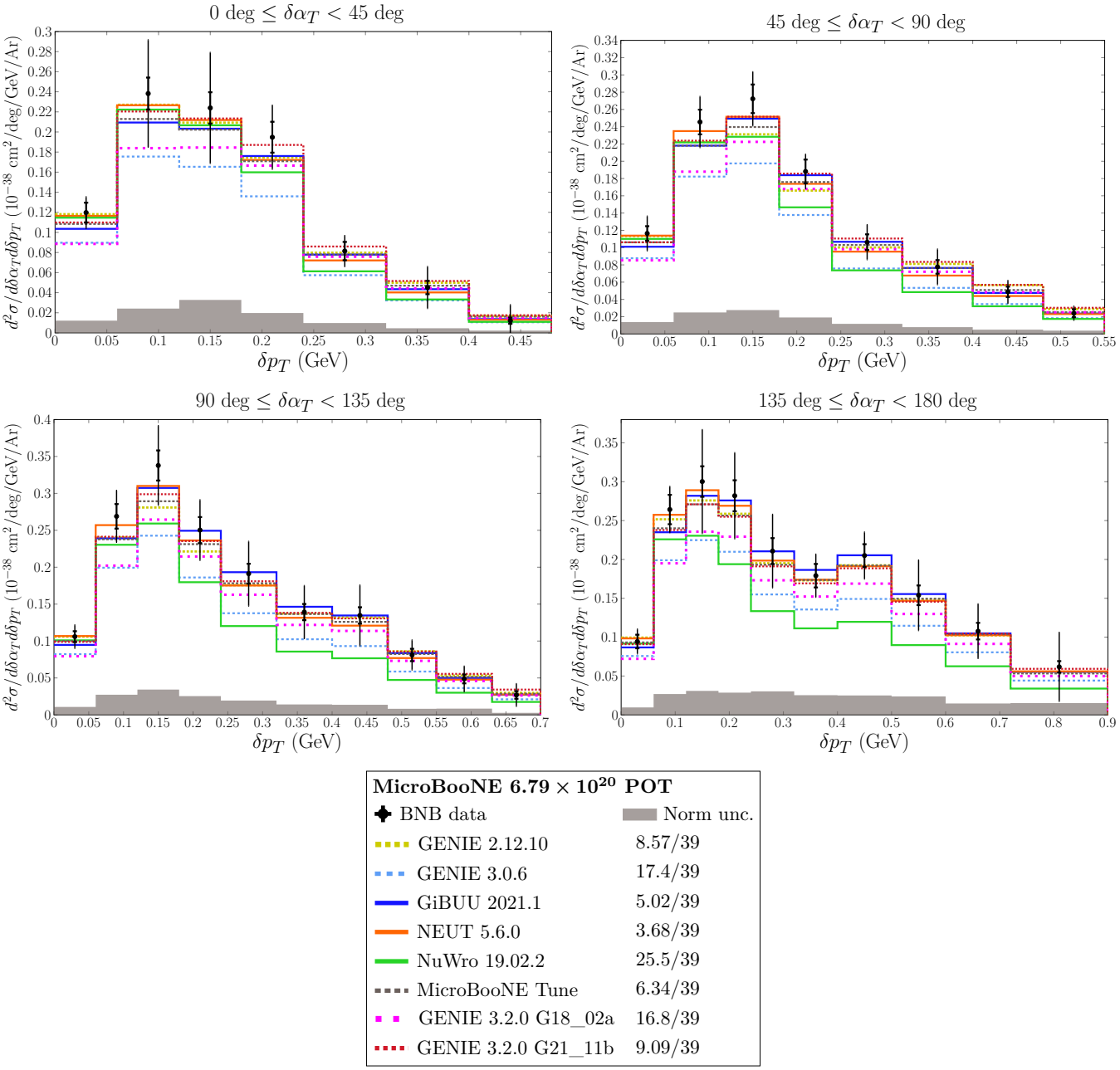

FIG. 18. Measured differential cross sections for block #3 ($\delta\alpha_T, \delta p_T$). The overall χ^2 value includes contributions from four δp_T overflow bins that are not plotted. Statistical (shape-only systematic) uncertainties are included in the inner (outer) error bars. The remainder of the total uncertainty is shown by the gray band along the x-axis.

A covariance matrix describing correlated uncertainties between all 359 kinematic bins is provided in the supplemental materials, allowing goodness-of-fit to be quantitatively assessed for theoretical predictions describing the entire data set. This data release strategy represents an improvement over the typical procedure employed to date in the neutrino scattering literature, in which correlations between distinct kinematic distributions are not disclosed.

The predictions of several standard neutrino event generators are presented and compared to the MicroBooNE data. The GiBUU 2021.1 model provides a relatively good description of all of the individual differential cross sections studied, but its poor agreement with the combined set of measurements (quantified with the χ^2 score given in Table II) suggests that the correlations between kinematic distributions are less well-modeled. Overall agreement is likewise unsatisfactory for the other neutrino interaction models considered herein, although those with the least sophisticated treatments of nu-

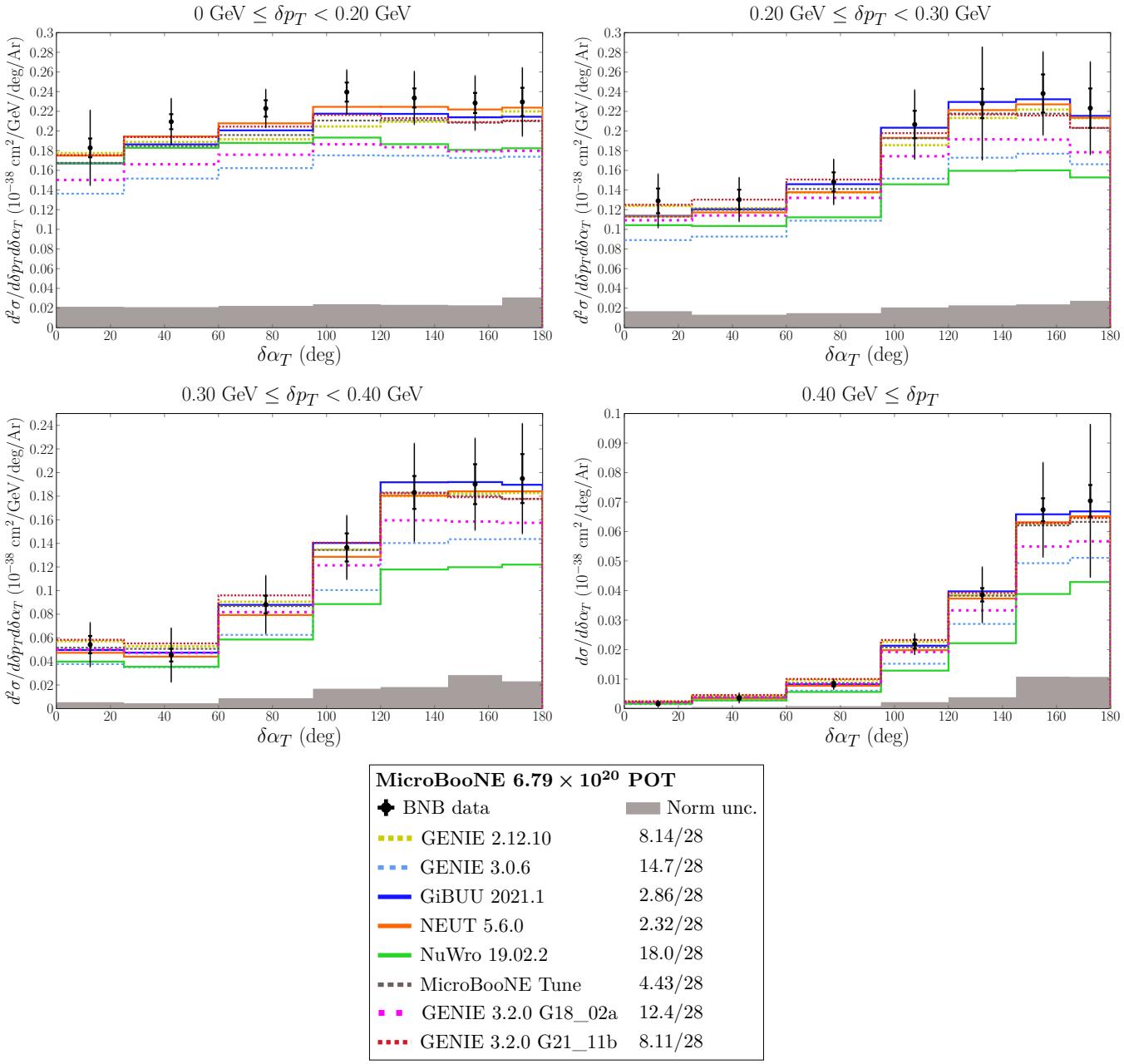

FIG. 19. Measured differential cross sections for block #4 ($\delta p_T, \delta\alpha_T$). Statistical (shape-only systematic) uncertainties are included in the inner (outer) error bars. The remainder of the total uncertainty is shown by the gray band along the x-axis.

clear effects (GENIE 2.12.10 and GENIE 3.2.0 G18_02a) obtain substantially higher χ^2 values than the others. The GENIE 3.0.6 prediction achieves the best overall goodness-of-fit of the models studied, but it is seen to systematically underpredict the data across a large fraction of the measured phase space.

Some of the kinematic regions for which the present measurements give the greatest model discrimination power include moderate p_μ, low to moderate $\cos\theta_\mu$, and low p_p. The data show a clear preference for the greater cross-section strength assigned to these regions by GiBUU 2021.1 and NEUT 5.6.0 compared with the other event generators studied. These two models also describe the distribution of the muon-proton opening angle $\theta_{\mu p}$ noticeably better than their counterparts. Especially when combined with recent MicroBooNE measurements examining more exclusive [58, 59, 94] and inclusive [68, 95] final-state topologies in charged-current ν_μ-argon scattering, the present data set provides a highly detailed benchmark for the ongoing effort to improve event generators to the precision needed for the future accelerator-based neutrino oscillation program.

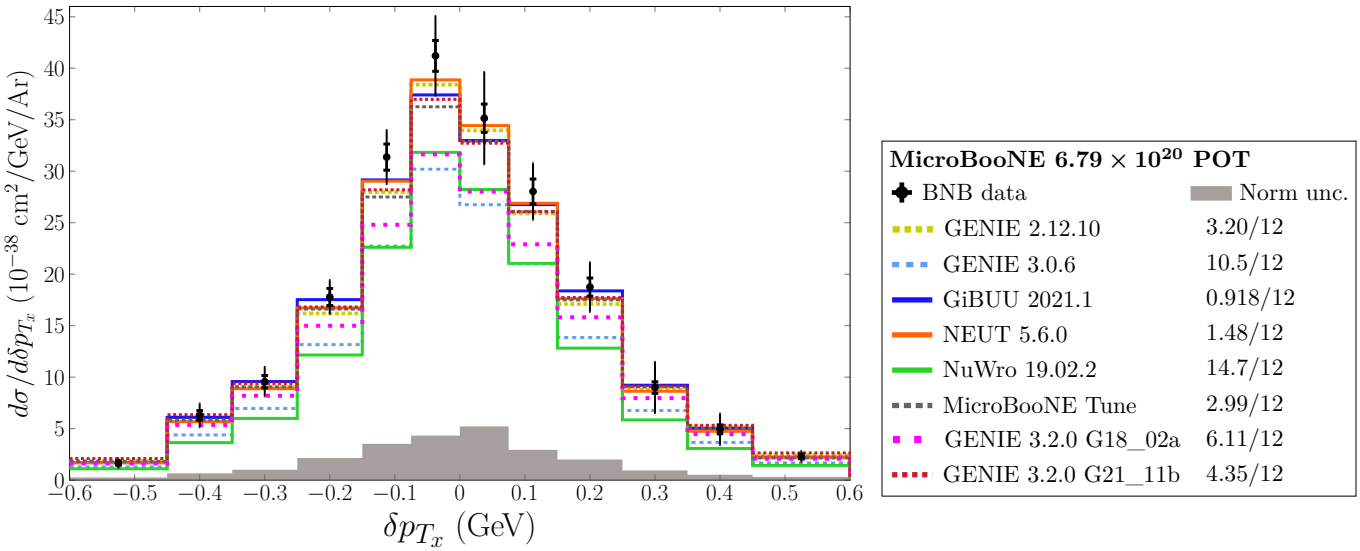

FIG. 20. Measured differential cross sections for block #5 (δp_{T_x}). Statistical (shape-only systematic) uncertainties are included in the inner (outer) error bars. The remainder of the total uncertainty is shown by the gray band along the x-axis.

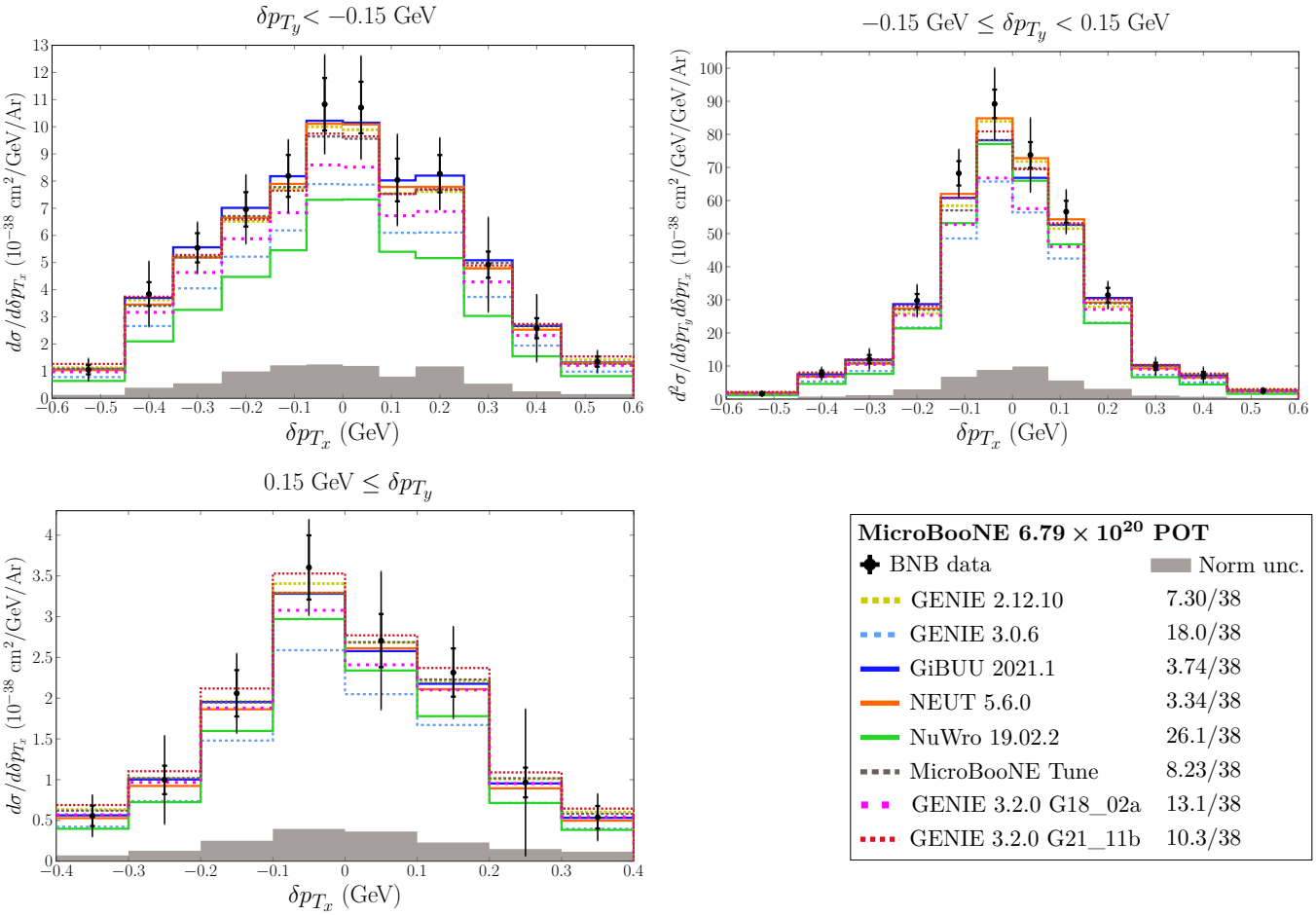

FIG. 21. Measured differential cross sections for block #6 ($\delta p_{T_y}, \delta p_{T_x}$). The overall χ^2 value includes contributions from three underflow and three overflow δp_{T_x} bins that are not plotted. Statistical (shape-only systematic) uncertainties are included in the inner (outer) error bars. The remainder of the total uncertainty is shown by the gray band along the x-axis.

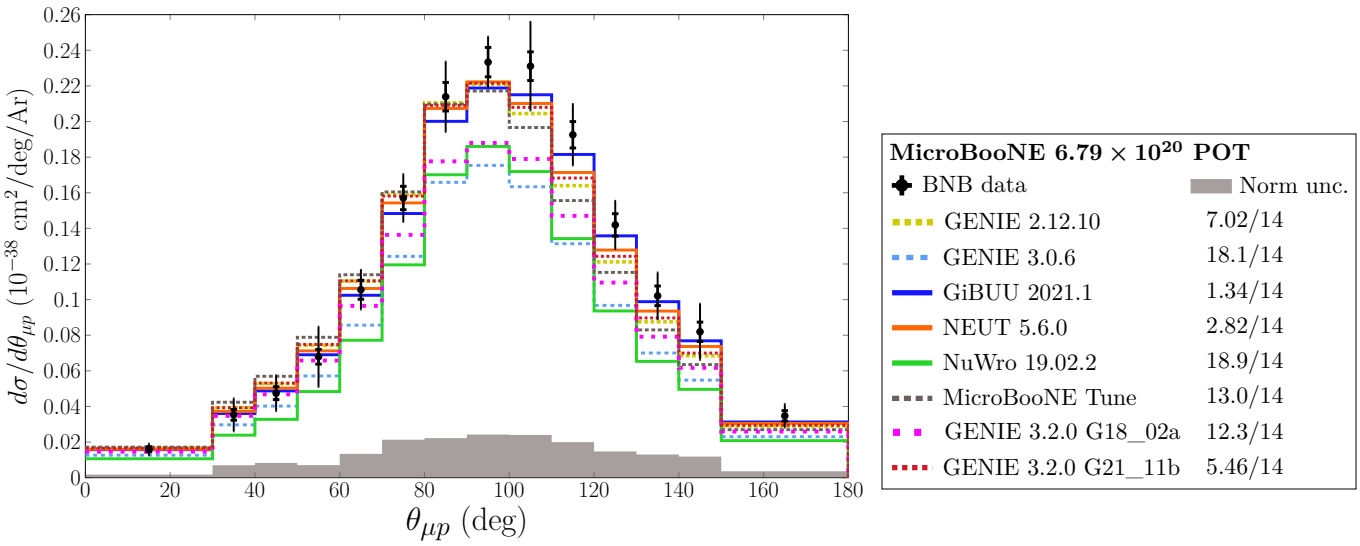

FIG. 22. Measured differential cross sections for block #7 ($\theta_{\mu p}$). Statistical (shape-only systematic) uncertainties are included in the inner (outer) error bars. The remainder of the total uncertainty is shown by the gray band along the x-axis.

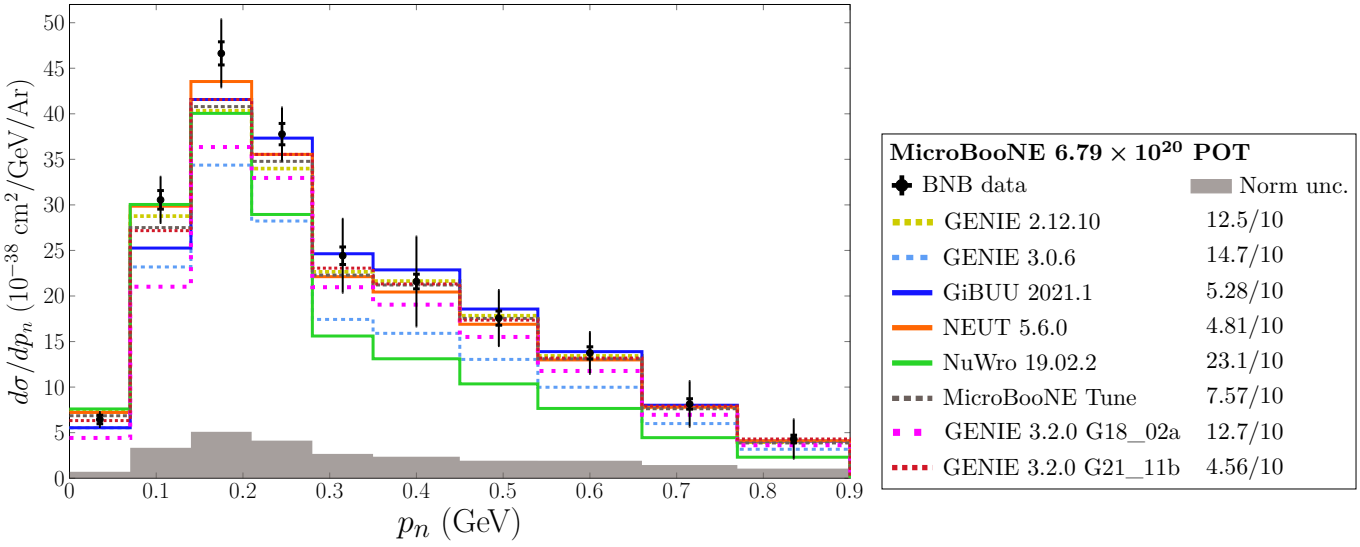

FIG. 23. Measured differential cross sections for block #8 (p_n). Statistical (shape-only systematic) uncertainties are included in the inner (outer) error bars. The remainder of the total uncertainty is shown by the gray band along the x-axis.

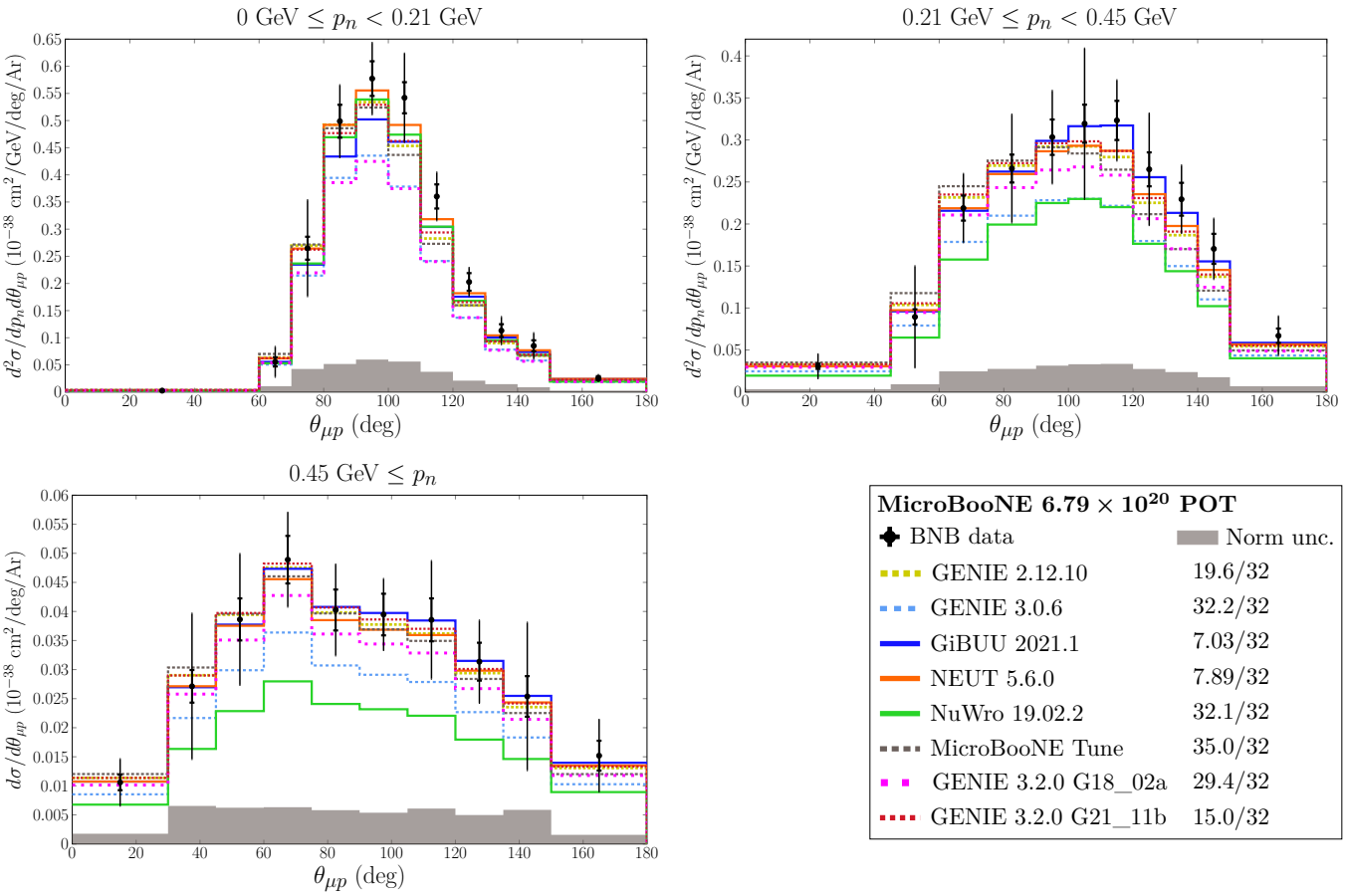

FIG. 24. Measured differential cross sections for block #9 ($p_n, \theta_{\mu p}$). Statistical (shape-only systematic) uncertainties are included in the inner (outer) error bars. The remainder of the total uncertainty is shown by the gray band along the x-axis.

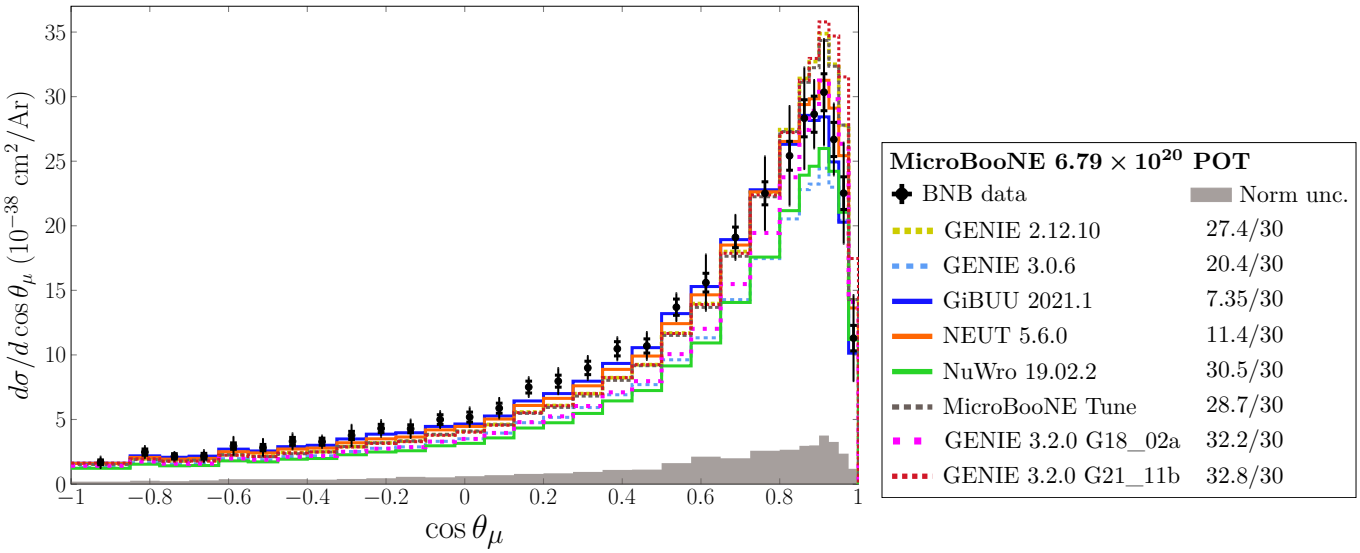

FIG. 25. Measured differential cross sections for block #10 ($\cos\theta_\mu$). Statistical (shape-only systematic) uncertainties are included in the inner (outer) error bars. The remainder of the total uncertainty is shown by the gray band along the x-axis.

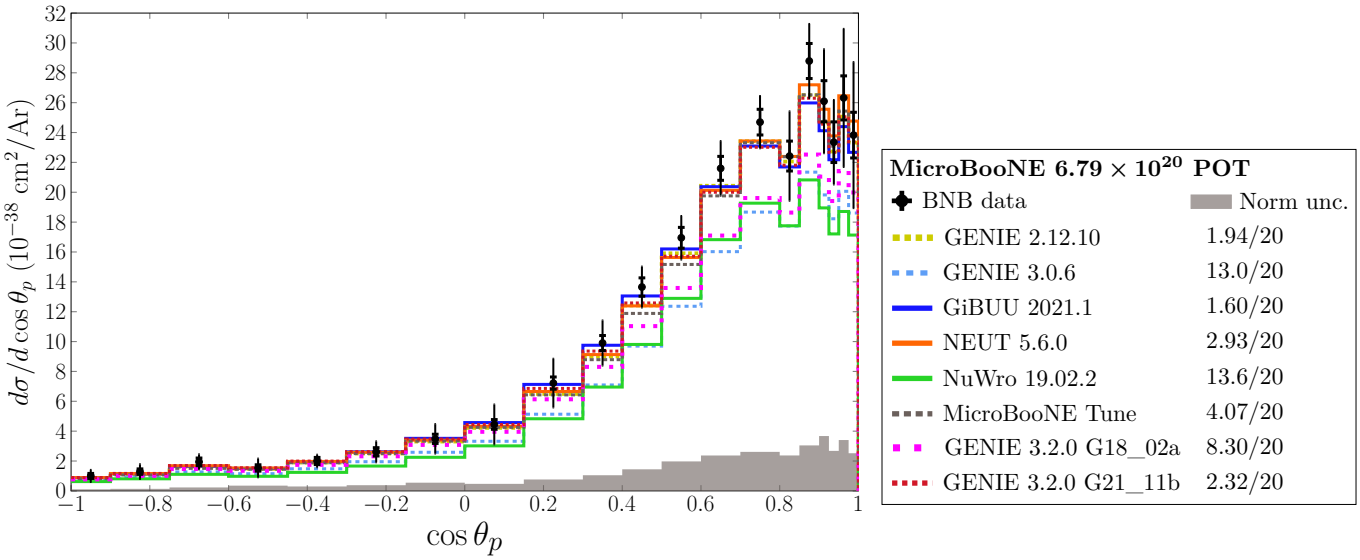

FIG. 26. Measured differential cross sections for block #11 ($\cos\theta_p$). Statistical (shape-only systematic) uncertainties are included in the inner (outer) error bars. The remainder of the total uncertainty is shown by the gray band along the x-axis.

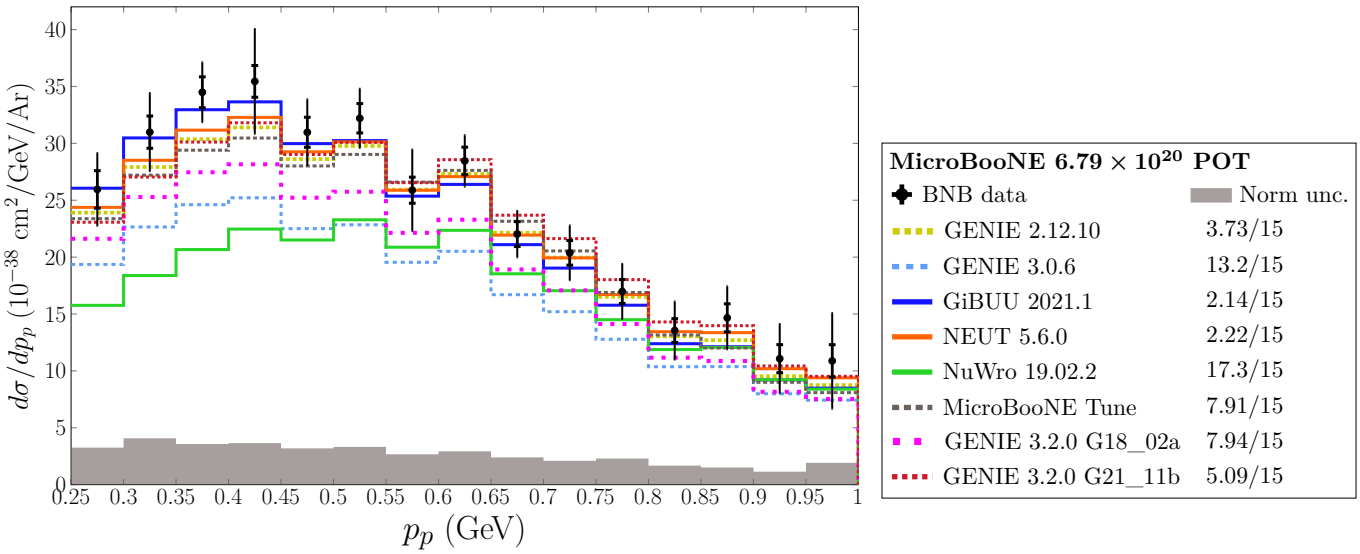

FIG. 27. Measured differential cross sections for block #12 (p_p). Statistical (shape-only systematic) uncertainties are included in the inner (outer) error bars. The remainder of the total uncertainty is shown by the gray band along the x-axis.

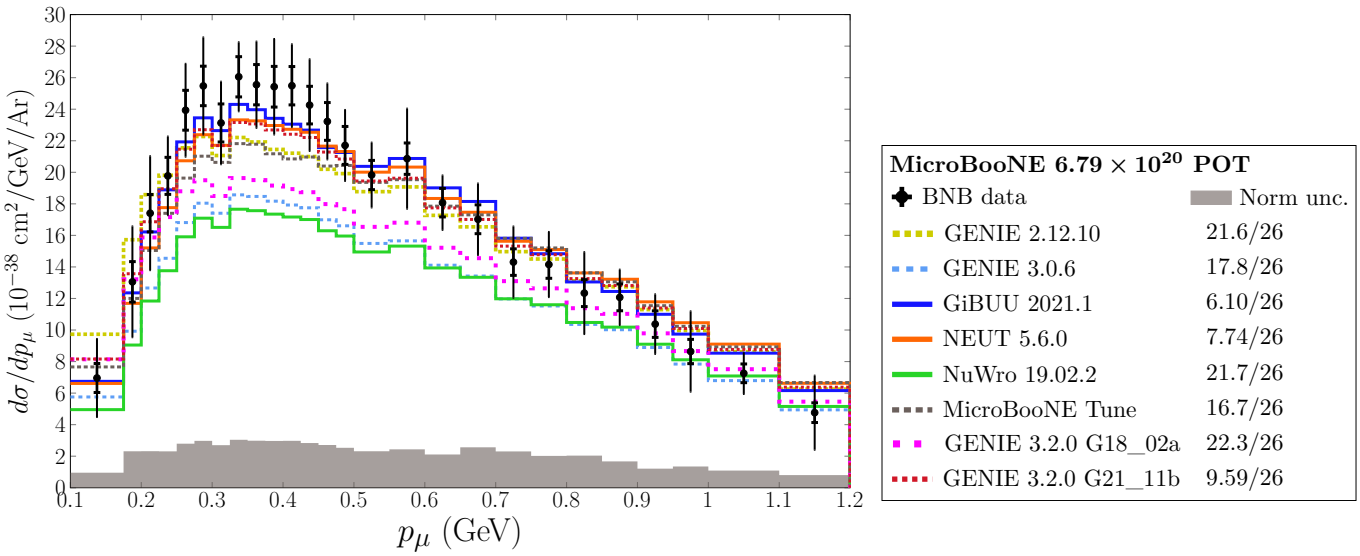

FIG. 28. Measured differential cross sections for block #13 (p_μ). Statistical (shape-only systematic) uncertainties are included in the inner (outer) error bars. The remainder of the total uncertainty is shown by the gray band along the x-axis.

IX. ACKNOWLEDGMENTS

This document was prepared by the MicroBooNE collaboration using the resources of the Fermi National Accelerator Laboratory (Fermilab), a U.S. Department of Energy, Office of Science, HEP User Facility. Fermilab is managed by Fermi Research Alliance, LLC (FRA), acting under Contract No. DE-AC02-07CH11359. MicroBooNE is supported by the following: the U.S. Department of Energy, Office of Science, Offices of High Energy Physics and Nuclear Physics; the U.S. National Science Foundation; the Swiss National Science Foundation; the Science and Technology Facilities Council (STFC), part of the United Kingdom Research and Innovation; the Royal Society (United Kingdom); the UK Research and Innovation (UKRI) Future Leaders Fellowship; and the NSF AI Institute for Artificial Intelligence and Fundamental Interactions. Additional support for the laser calibration system and cosmic ray tagger was provided by the Albert Einstein Center for Fundamental Physics, Bern, Switzerland. We also acknowledge the contributions of technical and scientific staff to the design, construction, and operation of the MicroBooNE detector as well as the contributions of past collaborators to the development of MicroBooNE analyses, without whom this work would not have been possible. For the purpose of open access, the authors have applied a Creative Commons Attribution (CC BY) public copyright license to any Author Accepted Manuscript version arising from this submission.

Appendix A: Bin definitions

Table III presents the full set of 359 kinematic bins used to report the CC0πNp cross section measurements. For an observable x, the bin with lower limit x^{low} and upper limit x^{high} will include events with $x^{\text{low}} \leq x < x^{\text{high}}$. The blocks of related bins (indicated in the table) are defined so that a selected event will belong to a unique bin within each block.

TABLE III: Bin definitions used in the analysis.

Block 0: $(p_\mu, \cos\theta_\mu)$

bin number	p_μ^{low} (GeV/c)	p_μ^{high} (GeV/c)	$\cos\theta_\mu^{\text{low}}$	$\cos\theta_\mu^{\text{high}}$
0	0.1	0.24	−1	−0.55
1			−0.55	−0.25
2			−0.25	0
3			0	0.25
4			0.25	0.45
5			0.45	0.7
6			0.7	1
7	0.24	0.3	−1	−0.55
8			−0.55	−0.25
9			−0.25	0
10			0	0.25
11			0.25	0.45
12			0.45	0.7
13			0.7	1
14	0.3	0.38	−1	−0.4
15			−0.4	−0.1
16			−0.1	0.1
17			0.1	0.35
18			0.35	0.5
19			0.5	0.7
20			0.7	0.85
21			0.85	1
22	0.38	0.48	−1	0
23			0	0.5
24			0.5	0.65
25			0.65	0.8
26			0.8	0.92
27			0.92	1
28	0.48	0.7	−1	0.2
29			0.2	0.5
30			0.5	0.65
31			0.65	0.8
32			0.8	0.875
33			0.875	0.95
34			0.95	1
35	0.7	0.85	−1	0.65
36			0.65	0.8
37			0.8	0.875
38			0.875	0.95
39			0.95	1
40	0.85	1.2	−1	0.85
41			0.85	0.9
42			0.9	0.95
43			0.95	1

Block 1: $(p_p, \cos\theta_p)$

bin number	p_p^{low} (GeV/c)	p_p^{high} (GeV/c)	$\cos\theta_p^{\text{low}}$	$\cos\theta_p^{\text{high}}$
44	0.25	0.325	−1	0
45			0	1
46	0.325	0.4	−1	−0.5

47			−0.5	0
48			0	0.5
49			0.5	0.8
50			0.8	1
51	0.4	0.5	−1	−0.6
52			−0.6	−0.2
53			−0.2	0.2
54			0.2	0.5
55			0.5	0.65
56			0.65	0.85
57			0.85	1
58	0.5	0.6	−1	−0.2
59			−0.2	0.2
60			0.2	0.4
61			0.4	0.6
62			0.6	0.7
63			0.7	0.8
64			0.8	0.9
65			0.9	1
66	0.6	0.7	−1	0.1
67			0.1	0.37
68			0.37	0.5
69			0.5	0.6
70			0.6	0.7
71			0.7	0.8
72			0.8	0.9
73			0.9	1
74	0.7	1	−1	0.45
75			0.45	0.65
76			0.65	0.75
77			0.75	0.82
78			0.82	0.9
79			0.9	1

Block 2: δp_T

bin number	δp_T^{low} (GeV/c)	δp_T^{high} (GeV/c)
80	0	0.06
81	0.06	0.12
82	0.12	0.18
83	0.18	0.24
84	0.24	0.32
85	0.32	0.40
86	0.40	0.48
87	0.48	0.55
88	0.55	0.68
89	0.68	0.75
90	0.75	0.90
91	0.90	∞

Block 3: $(\delta\alpha_T, \delta p_T)$

bin number	$\delta\alpha_T^{\text{low}}$ (°)	$\delta\alpha_T^{\text{high}}$ (°)	δp_T^{low} (GeV/c)	δp_T^{high} (GeV/c)
92	0	45	0	0.06
93			0.06	0.12
94			0.12	0.18
95			0.18	0.24
96			0.24	0.32

97			0.32	0.40
98			0.40	0.48
99			0.48	∞
100	45	90	0	0.06
101			0.06	0.12
102			0.12	0.18
103			0.18	0.24
104			0.24	0.32
105			0.32	0.40
106			0.40	0.48
107			0.48	0.55
108			0.55	∞
109	90	135	0	0.06
110			0.06	0.12
111			0.12	0.18
112			0.18	0.24
113			0.24	0.32
114			0.32	0.40
115			0.40	0.48
116			0.48	0.55
117			0.55	0.63
118			0.63	0.70
119			0.70	∞
120	135	180	0	0.06
121			0.06	0.12
122			0.12	0.18
123			0.18	0.24
124			0.24	0.32
125			0.32	0.40
126			0.40	0.50
127			0.50	0.60
128			0.60	0.72
129			0.72	0.90
130			0.90	∞

Block 4: $(\delta p_T, \delta\alpha_T)$

bin number	δp_T^{low} (GeV/c)	δp_T^{high} (GeV/c)	$\delta\alpha_T^{\text{low}}$ (°)	$\delta\alpha_T^{\text{high}}$ (°)
131	0	0.2	0	25
132			25	60
133			60	95
134			95	120
135			120	145
136			145	165
137			165	180
138	0.2	0.3	0	25
139			25	60
140			60	95
141			95	120
142			120	145
143			145	165
144			165	180
145	0.3	0.4	0	25
146			25	60
147			60	95
148			95	120
149			120	145
150			145	165

151			165	180
152	0.4	∞	0	25
153			25	60
154			60	95
155			95	120
156			120	145
157			145	165
158			165	180

Block 5: δp_{T_x}

bin number	$\delta p_{T_x}^{\text{low}}$ (GeV/c)	$\delta p_{T_x}^{\text{high}}$ (GeV/c)
159	$-\infty$	-0.60
160	-0.60	-0.45
161	-0.45	-0.35
162	-0.35	-0.25
163	-0.25	-0.15
164	-0.15	-0.075
165	-0.075	0
166	0	0.075
167	0.075	0.15
168	0.15	0.25
169	0.25	0.35
170	0.35	0.45
171	0.45	0.6
172	0.60	∞

Block 6: $(\delta p_{T_y}, \delta p_{T_x})$

bin number	$\delta p_{T_y}^{\text{low}}$ (GeV/c)	$\delta p_{T_y}^{\text{high}}$ (GeV/c)	$\delta p_{T_x}^{\text{low}}$ (GeV/c)	$\delta p_{T_x}^{\text{high}}$ (GeV/c)
173	$-\infty$	-0.15	$-\infty$	-0.6
174			-0.6	-0.45
175			-0.45	-0.35
176			-0.35	-0.25
177			-0.25	-0.15
178			-0.15	-0.075
179			-0.075	0
180			0	0.075
181			0.075	0.15
182			0.15	0.25
183			0.25	0.35
184			0.35	0.45
185			0.45	0.60
186			0.60	∞
187	-0.15	0.15	$-\infty$	-0.6
188			-0.6	-0.45
189			-0.45	-0.35
190			-0.35	-0.25
191			-0.25	-0.15
192			-0.15	-0.075
193			-0.075	0
194			0	0.075
195			0.075	0.15
196			0.15	0.25
197			0.25	0.35
198			0.35	0.45
199			0.45	0.60
200			0.60	∞

201	0.15	∞	$-\infty$	-0.4
202			-0.4	-0.3
203			-0.3	-0.2
204			-0.2	-0.1
205			-0.1	0
206			0	0.1
207			0.1	0.2
208			0.2	0.3
209			0.3	0.4
210			0.4	∞

Block 7: $\theta_{\mu p}$

bin number	$\theta_{\mu p}^{\text{low}}$ (°)	$\theta_{\mu p}^{\text{high}}$ (°)
211	0	30
212	30	40
213	40	50
214	50	60
215	60	70
216	70	80
217	80	90
218	90	100
219	100	110
220	110	120
221	120	130
222	130	140
223	140	150
224	150	180

Block 8: p_n

bin number	p_n^{low} (GeV/c)	p_n^{high} (GeV/c)
225	0	0.07
226	0.07	0.14
227	0.14	0.21
228	0.21	0.28
229	0.28	0.35
230	0.35	0.45
231	0.45	0.54
232	0.54	0.66
233	0.66	0.77
234	0.77	0.9
235	0.9	∞

Block 9: $(p_n, \theta_{\mu p})$

bin number	p_n^{low} (GeV/c)	p_n^{high} (GeV/c)	$\theta_{\mu p}^{\text{low}}$ (°)	$\theta_{\mu p}^{\text{high}}$ (°)
236	0	0.21	0	60
237			60	70
238			70	80
239			80	90
240			90	100
241			100	110
242			110	120
243			120	130
244			130	140
245			140	150
246			150	180
247	0.21	0.45	0	45

248			45	60
249			60	75
250			75	90
251			90	100
252			100	110
253			110	120
254			120	130
255			130	140
256			140	150
257			150	180
258	0.45	∞	0	30
259			30	45
260			45	60
261			60	75
262			75	90
263			90	105
264			105	120
265			120	135
266			135	150
267			150	180

Block 10: $\cos\theta_\mu$

bin number	$\cos\theta_\mu^{\text{low}}$	$\cos\theta_\mu^{\text{high}}$
268	-1	-0.85
269	-0.85	-0.775
270	-0.775	-0.7
271	-0.7	-0.625
272	-0.625	-0.55
273	-0.55	-0.475
274	-0.475	-0.4
275	-0.4	-0.325
276	-0.325	-0.25
277	-0.25	-0.175
278	-0.175	-0.1
279	-0.1	-0.025
280	-0.025	0.05
281	0.05	0.125
282	0.125	0.2
283	0.2	0.275
284	0.275	0.35
285	0.35	0.425
286	0.425	0.5
287	0.5	0.575
288	0.575	0.65
289	0.65	0.725
290	0.725	0.8
291	0.8	0.85
292	0.85	0.875
293	0.875	0.9
294	0.9	0.925
295	0.925	0.95
296	0.95	0.975
297	0.975	1

Block 11: $\cos\theta_p$

bin number	$\cos\theta_p^{\text{low}}$	$\cos\theta_p^{\text{high}}$
298	-1	-0.9
299	-0.9	-0.75

300	−0.75	−0.6
301	−0.6	−0.45
302	−0.45	−0.3
303	−0.3	−0.15
304	−0.15	0
305	0	0.15
306	0.15	0.3
307	0.3	0.4
308	0.4	0.5
309	0.5	0.6
310	0.6	0.7
311	0.7	0.8
312	0.8	0.85
313	0.85	0.9
314	0.9	0.925
315	0.925	0.95
316	0.95	0.975
317	0.975	1

Block 12: p_p

bin number	p_p^{low} (GeV/c)	p_p^{high} (GeV/c)
318	0.25	0.3
319	0.3	0.35
320	0.35	0.4
321	0.4	0.45
322	0.45	0.5
323	0.5	0.55
324	0.55	0.6
325	0.6	0.65
326	0.65	0.7
327	0.7	0.75
328	0.75	0.8
329	0.8	0.85
330	0.85	0.9
331	0.9	0.95
332	0.95	1

Block 13: p_μ

bin number	p_μ^{low} (GeV/c)	p_μ^{high} (GeV/c)
333	0.1	0.175
334	0.175	0.2
335	0.2	0.225
336	0.225	0.25
337	0.25	0.275
338	0.275	0.3
339	0.3	0.325
340	0.325	0.35
341	0.35	0.375
342	0.375	0.4
343	0.4	0.425
344	0.425	0.45
345	0.45	0.475
346	0.475	0.5
347	0.5	0.55
348	0.55	0.6
349	0.6	0.65
350	0.65	0.7
351	0.7	0.75
352	0.75	0.8

353	0.8	0.85
354	0.85	0.9
355	0.9	0.95
356	0.95	1
357	1	1.1
358	1.1	1.2

[1] G. C. Branco, R. González Felipe, and F. R. Joaquim, Leptonic CP violation, Rev. Mod. Phys. **84**, 515 (2012), arXiv:1111.5332 [hep-ph].

[2] C. Giunti and T. Lasserre, eV-scale sterile neutrinos, Annu. Rev. Nucl. Part. Sci. **69**, 163 (2019), arXiv:1901.08330 [hep-ph].

[3] P. F. de Salas, S. Gariazzo, O. Mena, C. A. Ternes, and M. Tórtola, Neutrino mass ordering from oscillations and beyond: 2018 status and future prospects, Front. Astron. Space Sci. **5**, 10.3389/fspas.2018.00036 (2018), arXiv:1806.11051 [hep-ph].

[4] P. A. N. Machado, O. Palamara, and D. W. Schmitz, The Short-Baseline Neutrino program at Fermilab, Annu. Rev. Nucl. Part. Sci. **69**, 363 (2019), arXiv:1903.04608 [hep-ex].

[5] B. Abi, R. Acciarri, M. A. Acero, *et al.* (DUNE Collaboration), Deep Underground Neutrino Experiment (DUNE), Far Detector Technical Design Report, Volume II: DUNE Physics, (2020), arXiv:2002.03005 [hep-ex].

[6] L. Alvarez-Ruso *et al.*, Neutrino Scattering Theory Experiment Collaboration white paper: Status and challenges of neutrino–nucleus scattering, Prog. Part. Nucl. Phys. **100**, 1 (2018), arXiv:1706.03621 [hep-ph].

[7] K. E. Duffy, A. P. Furmanski, E. Gramellini, O. Palamara, M. Soderberg, and T. Yang, Neutrino interaction measurements with the MicroBooNE and ArgoNeuT liquid argon time projection chambers, Eur. Phys. J. Spec. Top. **230**, 4275 (2021).

[8] C. Anderson *et al.* (ArgoNeuT Collaboration), The ArgoNeuT detector in the NuMI low-energy beam line at Fermilab, J. Instrum. **7** (10), P10019, arXiv:1205.6747 [physics.ins-det].

[9] R. Acciarri *et al.* (MicroBooNE Collaboration), Design and construction of the MicroBooNE detector, J. Instrum. **12** (02), P02017, arXiv:1612.05824 [physics.ins-det].

[10] P. Abratenko *et al.* (MicroBooNE Collaboration), Measurement of differential cross sections for ν_μ-Ar charged-current interactions with protons and no pions in the final state with the MicroBooNE detector, Phys. Rev. D **102**, 112013 (2020), arXiv:2010.02390 [hep-ex].

[11] P. Abratenko *et al.* (MicroBooNE Collaboration), New CC0π GENIE model tune for MicroBooNE, Phys. Rev. D **105**, 072001 (2022), arXiv:2110.14028 [hep-ex].

[12] P. Abratenko *et al.* (MicroBooNE Collaboration), Calorimetric classification of track-like signatures in liquid argon TPCs using MicroBooNE data, J. High Energy Phys. **2021** (12), 153, arXiv:2109.02460 [physics.ins-det].

[13] P. Abratenko *et al.* (MicroBooNE Collaboration), Novel approach for evaluating detector-related uncertainties in a LArTPC using MicroBooNE data, Eur. Phys. J. C **82**, 454 (2022), arXiv:2111.03556 [physics.ins-det].

[14] A. A. Aguilar-Arevalo *et al.* (MiniBooNE Collaboration), Neutrino flux prediction at MiniBooNE, Phys. Rev. D **79**, 072002 (2009), arXiv:0806.1449 [hep-ex].

[15] P. Abratenko *et al.* (MicroBooNE Collaboration), First simultaneous measurement of differential muon-neutrino charged-current cross sections on argon for final states with and without protons using MicroBooNE data, (2024), arXiv:2402.19281 [hep-ex].

[16] P. Abratenko *et al.* (MicroBooNE Collaboration), Inclusive cross section measurements in final states with and without protons for charged-current ν_μ-Ar scattering in MicroBooNE, (2024), arXiv:2402.19216 [hep-ex].

[17] S. Gardiner, Mathematical methods for neutrino cross-section extraction, (2024), arXiv:2401.04065 [hep-ex].

[18] S. Agostinelli, J. Allison, K. Amako, *et al.*, Geant4–a simulation toolkit, Nucl. Instrum. Methods Phys. Res. A **506**, 250 (2003).

[19] J. Allison *et al.*, Recent developments in Geant4, Nucl. Instrum. Meth. Phys. Res. A **835**, 186 (2016).

[20] L. Alvarez-Ruso *et al.* (GENIE Collaboration), Recent highlights from GENIE v3, Eur. Phys. J. ST **230**, 4449 (2021).

[21] C. Andreopoulos *et al.*, The GENIE neutrino Monte Carlo generator, Nucl. Instrum. Methods Phys. Res. A **614**, 87 (2010).

[22] C. Andreopoulos *et al.*, The GENIE neutrino monte carlo generator: Physics and user manual, arXiv (2015), 1510.05494 [hep-ph].

[23] R. Carrasco and E. Oset, Interaction of real photons with nuclei from 100-MeV to 500-MeV, Nucl. Phys. A **536**, 445 (1992).

[24] J. Nieves, J. E. Amaro, and M. Valverde, Inclusive quasielastic charged-current neutrino-nucleus reactions, Phys. Rev. C **70**, 055503 (2004), nucl-th/0408005.

[25] J. Nieves, J. E. Amaro, and M. Valverde, Erratum: Inclusive quasielastic charged-current neutrino-nucleus reactions [Phys. Rev. C 70, 055503 (2004)], Phys. Rev. C **72**, 019902 (2005).

[26] J. Nieves, F. Sanchez, I. Ruiz Simo, and M. Vicente Vacas, Neutrino energy reconstruction and the shape of the CCQE-like total cross section, Phys. Rev. D **85**, 113008 (2012).

[27] R. Gran, J. Nieves, F. Sanchez, and M. J. Vicente Vacas, Neutrino-nucleus quasi-elastic and 2p2h interactions up to 10 GeV, Phys. Rev. D **88**, 113007 (2013), arXiv:1307.8105 [hep-ph].

[28] J. Schwehr, D. Cherdack, and R. Gran, GENIE implementation of IFIC Valencia model for QE-like 2p2h

neutrino-nucleus cross section, (2017), arXiv:1601.02038 [hep-ph].
[29] J. A. Nowak (MiniBooNE Collaboration), Four momentum transfer discrepancy in the charged current π^+ production in the MiniBooNE: Data vs. theory, AIP Conf. Proc. **1189**, 243 (2009).
[30] K. Kuzmin, V. Lyubushkin, and V. Naumov, Lepton polarization in neutrino nucleon interactions, Phys. Part. Nucl. **35**, S133 (2004).
[31] C. Berger and L. Sehgal, Lepton mass effects in single pion production by neutrinos, Phys. Rev. D **76**, 113004 (2007).
[32] K. M. Graczyk and J. T. Sobczyk, Form factors in the quark resonance model, Phys. Rev. D **77**, 053001 (2008), [Erratum: Phys.Rev.D 79, 079903 (2009)].
[33] E. A. Paschos and J.-Y. Yu, Neutrino interactions in oscillation experiments, Phys. Rev. D **65**, 033002 (2002), hep-ph/0107261.
[34] A. Bodek, I. Park, and U.-k. Yang, Improved low Q^2 model for neutrino and electron nucleon cross sections in few GeV region, Nucl. Phys. B (Proc. Suppl.) **139**, 113 (2005), hep-ph/0411202.
[35] A. Bodek and U.-k. Yang, NUFACT09 update to the Bodek-Yang unified model for electron– and neutrino–nucleon scattering cross sections, AIP Conf. Proc. **1222**, 233 (2010).
[36] C. Berger and L. Sehgal, PCAC and coherent pion production by low energy neutrinos, Phys. Rev. D **79**, 053003 (2009).
[37] S. Dytman, Y. Hayato, R. Raboanary, J. T. Sobczyk, J. Tena-Vidal, and N. Vololoniaina, Comparison of validation methods of simulations for final state interactions in hadron production experiments, Phys. Rev. D **104**, 053006 (2021).
[38] J. Tena-Vidal *et al.* (GENIE Collaboration), Neutrino-nucleon cross-section model tuning in GENIE v3, Phys. Rev. D **104**, 072009 (2021), arXiv:2104.09179 [hep-ph].
[39] K. Abe, C. Andreopoulos, M. Antonova, S. Aoki, A. Ariga, S. Assylbekov, D. Autiero, M. Barbi, G. J. Barker, *et al.* (T2K Collaboration), Measurement of double-differential muon neutrino charged-current interactions on C_8H_8 without pions in the final state using the T2K off-axis beam, Phys. Rev. D **93**, 112012 (2016), 1602.03652.
[40] E. Snider and G. Petrillo, LArSoft: toolkit for simulation, reconstruction and analysis of liquid argon TPC neutrino detectors, J. Phys.: Conf. Ser. **898**, 042057 (2017).
[41] C. Adams *et al.* (MicroBooNE Collaboration), Ionization electron signal processing in single phase LArTPCs. Part I. Algorithm description and quantitative evaluation with MicroBooNE simulation, J. Instrum. **13** (07), P07006, arXiv:1802.08709 [physics.ins-det].
[42] C. Adams *et al.* (MicroBooNE Collaboration), Ionization electron signal processing in single phase LArTPCs. Part II. Data/simulation comparison and performance in MicroBooNE, J. Instrum. **13** (07), P07007, arXiv:1804.02583 [physics.ins-det].
[43] R. Acciarri *et al.* (MicroBooNE Collaboration), Noise characterization and filtering in the MicroBooNE liquid argon TPC, J. Instrum. **12** (08), P08003, arXiv:1705.07341 [physics.ins-det].
[44] P. Abratenko *et al.* (MicroBooNE Collaboration), Measurement of space charge effects in the MicroBooNE LArTPC using cosmic muons, J. Instrum. **15** (12), P12037, arXiv:2008.09765 [physics.ins-det].
[45] C. Adams *et al.* (MicroBooNE Collaboration), A method to determine the electric field of liquid argon time projection chambers using a UV laser system and its application in MicroBooNE, J. Instrum. **15** (07), P07010.
[46] C. Adams *et al.* (MicroBooNE Collaboration), Rejecting cosmic background for exclusive neutrino interaction studies with liquid argon TPCs; a case study with the MicroBooNE detector, Eur. Phys. J. C **79**, 673 (2019), arXiv:1812.05679 [physics.ins-det].
[47] R. Acciarri *et al.* (MicroBooNE Collaboration), The Pandora multi-algorithm approach to automated pattern recognition of cosmic-ray muon and neutrino events in the MicroBooNE detector, Eur. Phys. J. C **78**, 82 (2018), arXiv:1708.03135 [hep-ex].
[48] P. Abratenko *et al.* (MicroBooNE Collaboration), Determination of muon momentum in the MicroBooNE LArTPC using an improved model of multiple Coulomb scattering, J. Instrum. **12** (10), P10010, arXiv:1703.06187 [physics.ins-det].
[49] W. V. D. Pontseele, *Search for Electron Neutrino Anomalies with the MicroBooNE Detector*, Ph.D. thesis, Oxford University (2020).
[50] P. Abratenko *et al.* (MicroBooNE collaboration), Search for an anomalous excess of charged-current ν_e interactions without pions in the final state with the MicroBooNE experiment, Phys. Rev. D **105**, 112004 (2022), arXiv:2110.14065 [hep-ex].
[51] M. J. Berger, J. S. Coursey, M. A. Zucker, and J. Chang, Stopping-power & range tables for electrons, protons, and helium ions, NIST Standard Reference Database 124 (2017).
[52] P. Stowell *et al.* (MINERvA Collaboration), Tuning the GENIE pion production model with MINERvA data, Phys. Rev. D **100**, 072005 (2019), arXiv:1903.01558 [hep-ex].
[53] X.-G. Lu, L. Pickering, S. Dolan, G. Barr, D. Coplowe, Y. Uchida, D. Wark, M. O. Wascko, A. Weber, and T. Yuan, Measurement of nuclear effects in neutrino interactions with minimal dependence on neutrino energy, Phys. Rev. C **94**, 015503 (2016), arXiv:1512.05748 [nucl-th].
[54] K. Abe *et al.* (T2K collaboration), Characterization of nuclear effects in muon-neutrino scattering on hydrocarbon with a measurement of final-state kinematics and correlations in charged-current pionless interactions at T2K, Phys. Rev. D **98**, 032003 (2018), arXiv:1802.05078 [hep-ex].
[55] X.-G. Lu *et al.* (MINERvA Collaboration), Measurement of final-state correlations in neutrino muon-proton mesonless production on hydrocarbon at $E = 3$ GeV, Phys. Rev. Lett. **121**, 022504 (2018), arXiv:1805.05486 [hep-ex].
[56] T. Cai *et al.* (MINERvA Collaboration), Nucleon binding energy and transverse momentum imbalance in neutrino-nucleus reactions, Phys. Rev. D **101**, 092001 (2020), arXiv:1910.08658 [hep-ex].
[57] L. Bathe-Peters, S. Gardiner, and R. Guenette, Comparing generator predictions of transverse kinematic imbalance in neutrino-argon scattering, arXiv (2022), 2201.04664 [hep-ph].
[58] P. Abratenko *et al.* (MicroBooNE), Multidifferential cross section measurements of ν_μ-argon quasielasticlike reactions with the MicroBooNE detector, Phys. Rev. D

108, 053002 (2023), arXiv:2301.03700 [hep-ex].
[59] P. Abratenko *et al.* (MicroBooNE), First double-differential measurement of kinematic imbalance in neutrino interactions with the MicroBooNE detector, Phys. Rev. Lett. **131**, 101802 (2023), arXiv:2301.03706 [hep-ex].
[60] A. P. Furmanski and J. T. Sobczyk, Neutrino energy reconstruction from one-muon and one-proton events, Phys. Rev. C **95**, 065501 (2017), arXiv:1609.03530 [hep-ex].
[61] P. Abratenko *et al.* (MicroBooNE Collaboration), Measurement of nuclear effects in neutrino-argon interactions using generalized kinematic imbalance variables with the MicroBooNE detector, (2023), arXiv:2310.06082 [nucl-ex].
[62] A. Bodek and T. Cai, Removal energies and final state interaction in lepton nucleus scattering, Eur. Phys. J. C **79**, 293 (2019), arXiv:1801.07975 [nucl-th].
[63] L. Koch and S. Dolan, Treatment of flux shape uncertainties in unfolded, flux-averaged neutrino cross-section measurements, Phys. Rev. D **102**, 113012 (2020), arXiv:2009.00552 [hep-ex].
[64] T. Golan, J. Sobczyk, and J. Żmuda, NuWro: the Wrocław Monte Carlo generator of neutrino interactions, Nucl. Phys. B - Proc. Suppl. **229-232**, 499 (2012).
[65] J. Calcutt, C. Thorpe, K. Mahn, and L. Fields, Geant4Reweight: a framework for evaluating and propagating hadronic interaction uncertainties in Geant4, J. Instrum. **16** (08), P08042, arXiv:2105.01744 [physics.data-an].
[66] R. Acciarri *et al.*, A study of electron recombination using highly ionizing particles in the ArgoNeuT liquid argon TPC, J. Instrum. **8** (08), P08005, arXiv:1306.1712 [phys.ins-det].
[67] P. Abratenko *et al.* (MicroBooNE Collaboration), First measurement of inclusive electron-neutrino and antineutrino charged current differential cross sections in charged lepton energy on argon in MicroBooNE, Phys. Rev. D **105**, L051102 (2022), arXiv:2109.06832 [hep-ex].
[68] P. Abratenko *et al.* (MicroBooNE Collaboration), First measurement of energy-dependent inclusive muon neutrino charged-current cross sections on argon with the MicroBooNE detector, Phys. Rev. Lett. **128**, 151801 (2022), arXiv:2110.14023 [hep-ex].
[69] W. Tang, X. Li, X. Qian, H. Wei, and C. Zhang, Data unfolding with Wiener-SVD method, J. Instrum. **12** (10), P10002, arXiv:1705.03568 [physics.data-an].
[70] G. D'Agostini, A multidimensional unfolding method based on Bayes' theorem, Nucl. Instrum. Methods Phys. Res. A **362**, 487 (1995).
[71] J. Bourbeau, *Measuring the cosmic-ray energy spectrum, composition, and anisotropy at PeV scales using the IceCube Observatory*, Ph.D. thesis, University of Wisconsin – Madison (2019).
[72] J. Bourbeau and Z. Hampel-Arias, PyUnfold: A Python package for iterative unfolding, J. Open Source Softw. **3**, 741 (2018), arXiv:1806.03350 [physics.data-an].
[73] M. Shaevitz, Separating components of error matrices (2008), BooNE Technical Note 253.
[74] P. Stowell *et al.*, NUISANCE: a neutrino cross-section generator tuning and comparison framework, J. Instrum. **12** (01), P01016, arXiv:1612.07393 [hep-ex].
[75] A. Bodek and J. L. Ritchie, Fermi-motion effects in deep-inelastic lepton scattering from nuclear targets, Phys. Rev. D **23**, 1070 (1981).
[76] C. Llewellyn Smith, Neutrino reactions at accelerator energies, Phys. Rept. **3**, 261 (1972).
[77] T. Katori, Meson exchange current (MEC) models in neutrino interaction generators, AIP Conf. Proc. **1663**, 030001 (2015).
[78] D. Rein and L. Sehgal, Neutrino excitation of baryon resonances and single pion production, Ann. Phys. **133**, 79 (1981).
[79] S. Dytman, GENIE final state interactions, AIP Conf. Proc. **1680**, 020005 (2015).
[80] S. A. Dytman and A. S. Meyer, Final state interactions in GENIE, AIP Conf. Proc. **1405**, 213 (2011).
[81] S. Dolan, G. D. Megias, and S. Bolognesi, Implementation of the SuSAv2-meson exchange current 1p1h and 2p2h models in GENIE and analysis of nuclear effects in T2K measurements, Phys. Rev. D **101**, 033003 (2020).
[82] R. González-Jiménez, G. D. Megias, M. B. Barbaro, J. A. Caballero, and T. W. Donnelly, Extensions of superscaling from relativistic mean field theory: the SuSAv2 model, Phys. Rev. C **90**, 035501 (2014), arXiv:1407.8346 [nucl-th].
[83] I. Ruiz Simo *et al.*, Emission of neutron–proton and proton–proton pairs in neutrino scattering, Phys. Lett. B **762**, 124 (2016), arXiv:1607.08451 [nucl-th].
[84] I. Ruiz Simo *et al.*, Relativistic model of $2p-2h$ meson exchange currents in (anti)neutrino scattering, J. Phys. G **44**, 065105 (2017), arXiv:1604.08423 [nucl-th].
[85] Y. Hayato and L. Pickering, The NEUT neutrino interaction simulation program library, Eur. Phys. J. Spec. Top. **230**, 4469 (2021), arXiv:2106.15809 [hep-ph].
[86] Y. Hayato, A neutrino interaction simulation program library NEUT, Acta Phys. Pol. B **40**, 2477 (2009).
[87] L. Salcedo, E. Oset, M. Vicente-Vacas, and C. Garcia-Recio, Computer simulation of inclusive pion nuclear reactions, Nucl. Phys. A **484**, 557 (1988).
[88] O. Buss, T. Gaitanos, K. Gallmeister, *et al.*, Transport-theoretical description of nuclear reactions, Phys. Rep. **512**, 1 (2012).
[89] T. Leitner, L. Alvarez-Ruso, and U. Mosel, Charged current neutrino-nucleus interactions at intermediate energies, Phys. Rev. C **73**, 065502 (2006), arXiv:nucl-th/0601103.
[90] U. Mosel, Neutrino event generators: foundation, status and future, J. Phys. G **46**, 113001 (2019), arXiv:1904.11506 [hep-ex].
[91] T. Sjöstrand, S. Mrenna, and P. Skands, PYTHIA 6.4 physics and manual, J. High Energy Phys. **2006** (05), 026, arXiv:hep-ph/0603175.
[92] A. Carlson, V. Pronyaev, D. Smith, N. Larson, Z. Chen, G. Hale, F.-J. Hambsch, E. Gai, S.-Y. Oh, S. Badikov, T. Kawano, H. Hofmann, H. Vonach, and S. Tagesen, International evaluation of neutron cross section standards, Nucl. Data Sheets **110**, 3215 (2009), special Issue on Nuclear Reaction Data.
[93] L. Bathe-Peters, S. Gardiner, and R. Guenette, Comparing generator predictions of transverse kinematic imbalance in neutrino-argon scattering, (2022), arXiv:2201.04664 [hep-ph].
[94] P. Abratenko *et al.* (MicroBooNE Collaboration), First measurement of differential cross sections for muon neutrino charged current interactions on argon with a two-

proton final state in the MicroBooNE detector, (2022), arXiv:2211.03734 [hep-ex].
[95] P. Abratenko *et al.* (MicroBooNE Collaboration), Measurement of triple-differential inclusive muon-neutrino charged-current cross section on argon with the MicroBooNE detector, (2023), arXiv:2307.06413 [hep-ex].

Measurement of double-differential cross sections for mesonless charged-current muon neutrino interactions on argon with final-state protons using the MicroBooNE detector

I. BASIC DATA RELEASE

The compressed tar archive file `basic_data_release.tar.bz2` contains the information required to allow new model predictions to be compared to the data reported in this paper. On Unix-like operating systems, the file contents can be extracted by running the command

```
tar xvfj basic_data_release.tar.bz2
```

in a terminal. All files discussed in the remainder of this section will be made available by this procedure. A separate, more detailed set of supplemental files related to this analysis is described in Sec. VI.

Table I reports the flux-averaged CC0πNp total cross section $\langle\sigma\rangle_\mu$ measured in each of the analysis bins μ defined in Table III from the main text. In the notation of Sec. VI F from the main text, the flux-averaged total cross sections and their covariances are obtained from the unfolded event counts $\hat{\phi}_\mu$ via the relations

$$\langle\sigma\rangle_\mu = \frac{\hat{\phi}_\mu}{\Phi\,\mathcal{N}_{\mathrm{Ar}}} \qquad\qquad \mathrm{Cov}\big(\langle\sigma\rangle_\mu, \langle\sigma\rangle_\nu\big) = \frac{\mathrm{Cov}(\hat{\phi}_\mu, \hat{\phi}_\nu)}{\Phi^2\,\mathcal{N}_{\mathrm{Ar}}^2}\,. \tag{1}$$

The $\langle\sigma\rangle_\mu$ values given here (in units of 10^{-38} cm^2 per argon nucleus) can thus be converted to the differential cross sections shown in the main text by dividing by the relevant bin width(s) $\Delta\mathbf{x}_\mu$. For two-dimensional bins, $\Delta\mathbf{x}_\mu$ is just the product of the widths along each axis, e.g., bin 0 from this analysis has $\Delta\mathbf{x}_0 = 0.063$ GeV/c. The choice to tabulate total rather than differential cross sections, as explained and recommended in Ref. [1, Sec. III D], greatly simplifies handling of units when covariances are reported between measurements of different observables. Statistical and total uncertainties on the measurements (calculated by taking the square root of the diagonal elements of the relevant covariance matrix) are also reported in the last two columns of Table I.

TABLE I: Measured flux-averaged CC0πNp total cross sections

bin number	total cross section (10^{-38} cm^2/Ar)	stat. unc. (10^{-38} cm^2/Ar)	total unc. (10^{-38} cm^2/Ar)
0	0.491	0.041	0.110
1	0.305	0.034	0.077
2	0.249	0.033	0.079
3	0.225	0.030	0.059
4	0.147	0.024	0.055
5	0.191	0.024	0.061
6	0.071	0.020	0.073
7	0.281	0.025	0.048
8	0.260	0.024	0.046
9	0.233	0.024	0.060
10	0.258	0.026	0.062
11	0.186	0.021	0.036
12	0.183	0.018	0.042
13	0.091	0.014	0.029
14	0.264	0.028	0.079
15	0.362	0.033	0.061
16	0.320	0.032	0.059
17	0.438	0.032	0.058
18	0.228	0.021	0.034
19	0.259	0.021	0.043
20	0.130	0.015	0.029
21	0.065	0.011	0.036
22	0.424	0.048	0.089
23	1.122	0.059	0.116
24	0.406	0.029	0.093
25	0.382	0.025	0.055

Table I continued from previous page

bin number	total cross section (10^{-38} cm^2/Ar)	stat. unc. (10^{-38} cm^2/Ar)	total unc. (10^{-38} cm^2/Ar)
26	0.188	0.018	0.059
27	0.089	0.012	0.023
28	0.325	0.084	0.172
29	0.986	0.091	0.175
30	1.045	0.072	0.162
31	1.118	0.056	0.171
32	0.618	0.039	0.093
33	0.392	0.026	0.087
34	0.151	0.017	0.038
35	0.474	0.156	0.261
36	0.740	0.088	0.243
37	0.487	0.045	0.134
38	0.446	0.035	0.085
39	0.151	0.018	0.043
40	1.100	0.182	0.414
41	0.771	0.082	0.151
42	0.828	0.061	0.194
43	0.405	0.036	0.122
44	0.612	0.064	0.251
45	1.400	0.099	0.249
46	0.215	0.032	0.081
47	0.481	0.054	0.143
48	0.777	0.055	0.145
49	0.639	0.044	0.116
50	0.479	0.042	0.123
51	0.120	0.025	0.059
52	0.175	0.035	0.102
53	0.311	0.040	0.110
54	0.923	0.058	0.170
55	0.484	0.040	0.093
56	0.697	0.046	0.138
57	0.627	0.045	0.088
58	0.168	0.028	0.068
59	0.244	0.032	0.120
60	0.200	0.027	0.109
61	0.650	0.046	0.106
62	0.370	0.033	0.106
63	0.428	0.034	0.078
64	0.382	0.032	0.064
65	0.408	0.035	0.106
66	0.148	0.025	0.103
67	0.193	0.027	0.104
68	0.266	0.033	0.071
69	0.248	0.031	0.069
70	0.402	0.038	0.082
71	0.450	0.037	0.091
72	0.456	0.037	0.099
73	0.360	0.030	0.087
74	0.326	0.046	0.139
75	0.832	0.076	0.168
76	0.937	0.080	0.195
77	0.609	0.058	0.141
78	0.768	0.057	0.158
79	0.959	0.051	0.184
80	1.213	0.059	0.162
81	2.743	0.081	0.290
82	3.030	0.085	0.383
83	2.474	0.079	0.296
84	2.108	0.076	0.296

Table I continued from previous page

bin number	total cross section (10^{-38} cm^2/Ar)	stat. unc. (10^{-38} cm^2/Ar)	total unc. (10^{-38} cm^2/Ar)
85	1.606	0.066	0.302
86	1.408	0.061	0.316
87	0.879	0.046	0.182
88	1.111	0.063	0.320
89	0.316	0.034	0.130
90	0.486	0.053	0.314
91	0.168	0.049	0.151
92	0.323	0.027	0.050
93	0.643	0.043	0.150
94	0.605	0.042	0.173
95	0.526	0.042	0.098
96	0.293	0.033	0.065
97	0.162	0.024	0.072
98	0.044	0.011	0.057
99	0.055	0.014	0.027
100	0.314	0.023	0.065
101	0.663	0.039	0.092
102	0.735	0.045	0.096
103	0.508	0.037	0.072
104	0.383	0.033	0.083
105	0.280	0.028	0.074
106	0.175	0.022	0.048
107	0.075	0.015	0.028
108	0.061	0.015	0.037
109	0.286	0.020	0.048
110	0.726	0.045	0.091
111	0.912	0.055	0.160
112	0.676	0.048	0.128
113	0.688	0.049	0.143
114	0.501	0.039	0.128
115	0.485	0.040	0.143
116	0.256	0.026	0.063
117	0.175	0.022	0.068
118	0.085	0.016	0.047
119	0.139	0.025	0.051
120	0.255	0.024	0.046
121	0.713	0.051	0.088
122	0.811	0.053	0.198
123	0.761	0.054	0.156
124	0.759	0.060	0.201
125	0.645	0.054	0.134
126	0.922	0.066	0.175
127	0.692	0.057	0.229
128	0.582	0.058	0.204
129	0.500	0.060	0.378
130	0.169	0.057	0.162
131	0.914	0.048	0.217
132	1.466	0.053	0.209
133	1.560	0.058	0.176
134	1.198	0.049	0.143
135	1.168	0.049	0.138
136	0.914	0.041	0.126
137	0.689	0.043	0.139
138	0.322	0.031	0.080
139	0.456	0.035	0.090
140	0.519	0.034	0.086
141	0.517	0.035	0.092
142	0.570	0.037	0.136
143	0.476	0.039	0.091

Table I continued from previous page

bin number	total cross section (10^{-38} cm^2/Ar)	stat. unc. (10^{-38} cm^2/Ar)	total unc. (10^{-38} cm^2/Ar)
144	0.335	0.030	0.081
145	0.135	0.018	0.046
146	0.159	0.019	0.080
147	0.309	0.026	0.086
148	0.341	0.030	0.079
149	0.458	0.035	0.110
150	0.380	0.034	0.096
151	0.292	0.031	0.078
152	0.041	0.011	0.027
153	0.125	0.018	0.058
154	0.288	0.027	0.063
155	0.547	0.038	0.099
156	0.964	0.057	0.247
157	1.348	0.078	0.385
158	1.056	0.081	0.419
159	0.083	0.015	0.028
160	0.248	0.029	0.078
161	0.628	0.046	0.122
162	0.956	0.060	0.167
163	1.778	0.083	0.270
164	2.353	0.095	0.329
165	3.090	0.112	0.407
166	2.636	0.103	0.515
167	2.102	0.091	0.250
168	1.875	0.088	0.313
169	0.899	0.056	0.255
170	0.494	0.042	0.142
171	0.345	0.033	0.089
172	0.029	0.011	0.024
173	0.079	0.017	0.024
174	0.158	0.026	0.063
175	0.384	0.044	0.126
176	0.554	0.054	0.108
177	0.696	0.063	0.160
178	0.614	0.058	0.135
179	0.812	0.073	0.165
180	0.803	0.071	0.167
181	0.603	0.059	0.132
182	0.827	0.069	0.176
183	0.492	0.048	0.182
184	0.258	0.037	0.121
185	0.203	0.028	0.064
186	0.021	0.010	0.034
187	0.017	0.006	0.015
188	0.073	0.016	0.034
189	0.230	0.029	0.053
190	0.361	0.039	0.097
191	0.892	0.060	0.168
192	1.535	0.083	0.184
193	2.007	0.097	0.252
194	1.660	0.088	0.334
195	1.274	0.074	0.174
196	0.943	0.066	0.146
197	0.297	0.033	0.085
198	0.218	0.028	0.064
199	0.114	0.022	0.041
200	0.007	0.005	0.014
201	0.019	0.007	0.027
202	0.056	0.012	0.026

Table I continued from previous page

bin number	total cross section (10^{-38} cm^2/Ar)	stat. unc. (10^{-38} cm^2/Ar)	total unc. (10^{-38} cm^2/Ar)
203	0.100	0.017	0.055
204	0.206	0.028	0.055
205	0.360	0.039	0.070
206	0.271	0.033	0.092
207	0.231	0.030	0.056
208	0.097	0.018	0.091
209	0.054	0.014	0.031
210	0.041	0.010	0.039
211	0.479	0.042	0.108
212	0.353	0.030	0.116
213	0.475	0.036	0.130
214	0.679	0.041	0.182
215	1.055	0.053	0.174
216	1.571	0.066	0.252
217	2.139	0.080	0.291
218	2.333	0.083	0.258
219	2.311	0.080	0.290
220	1.925	0.074	0.251
221	1.419	0.063	0.149
222	1.021	0.055	0.184
223	0.819	0.054	0.197
224	1.042	0.087	0.190
225	0.451	0.033	0.074
226	2.139	0.071	0.250
227	3.264	0.089	0.409
228	2.644	0.082	0.299
229	1.709	0.067	0.282
230	2.159	0.080	0.499
231	1.582	0.070	0.321
232	1.650	0.081	0.358
233	0.897	0.063	0.317
234	0.559	0.055	0.311
235	0.440	0.058	0.310
236	0.033	0.007	0.020
237	0.117	0.018	0.062
238	0.556	0.044	0.206
239	1.048	0.064	0.174
240	1.212	0.067	0.164
241	1.138	0.060	0.187
242	0.757	0.047	0.108
243	0.426	0.034	0.062
244	0.238	0.025	0.061
245	0.179	0.021	0.052
246	0.161	0.023	0.038
247	0.331	0.034	0.158
248	0.322	0.032	0.215
249	0.788	0.054	0.171
250	0.957	0.060	0.240
251	0.728	0.051	0.144
252	0.766	0.054	0.205
253	0.776	0.056	0.118
254	0.636	0.048	0.142
255	0.551	0.047	0.095
256	0.409	0.043	0.094
257	0.483	0.062	0.163
258	0.318	0.040	0.131
259	0.407	0.042	0.212
260	0.579	0.054	0.193
261	0.734	0.061	0.154

Table I continued from previous page

bin number	total cross section (10^{-38} cm^2/Ar)	stat. unc. (10^{-38} cm^2/Ar)	total unc. (10^{-38} cm^2/Ar)
262	0.604	0.053	0.146
263	0.592	0.054	0.122
264	0.578	0.055	0.177
265	0.470	0.049	0.130
266	0.381	0.052	0.210
267	0.456	0.077	0.182
268	0.252	0.028	0.072
269	0.185	0.018	0.037
270	0.161	0.015	0.025
271	0.161	0.017	0.041
272	0.221	0.019	0.060
273	0.212	0.018	0.058
274	0.248	0.023	0.054
275	0.246	0.021	0.042
276	0.282	0.024	0.066
277	0.323	0.024	0.058
278	0.321	0.023	0.067
279	0.374	0.028	0.057
280	0.389	0.029	0.072
281	0.440	0.029	0.079
282	0.563	0.034	0.070
283	0.598	0.035	0.090
284	0.674	0.039	0.097
285	0.786	0.041	0.086
286	0.802	0.041	0.113
287	1.027	0.047	0.146
288	1.170	0.054	0.228
289	1.433	0.060	0.198
290	1.689	0.067	0.288
291	1.271	0.056	0.226
292	0.708	0.036	0.115
293	0.716	0.035	0.092
294	0.759	0.036	0.139
295	0.667	0.033	0.107
296	0.563	0.032	0.103
297	0.283	0.025	0.086
298	0.100	0.017	0.041
299	0.194	0.027	0.072
300	0.292	0.038	0.083
301	0.230	0.032	0.107
302	0.300	0.036	0.077
303	0.392	0.042	0.119
304	0.523	0.046	0.169
305	0.668	0.049	0.204
306	1.083	0.061	0.257
307	0.990	0.050	0.170
308	1.365	0.061	0.181
309	1.695	0.070	0.245
310	2.160	0.080	0.299
311	2.470	0.086	0.298
312	1.121	0.050	0.184
313	1.440	0.059	0.159
314	0.652	0.034	0.127
315	0.584	0.034	0.097
316	0.658	0.037	0.144
317	0.596	0.038	0.136
318	1.298	0.082	0.228
319	1.549	0.071	0.266
320	1.725	0.068	0.222

Table I continued from previous page

bin number	total cross section (10^{-38} cm^2/Ar)	stat. unc. (10^{-38} cm^2/Ar)	total unc. (10^{-38} cm^2/Ar)
321	1.772	0.070	0.262
322	1.549	0.066	0.206
323	1.610	0.065	0.186
324	1.294	0.057	0.208
325	1.423	0.061	0.176
326	1.101	0.055	0.157
327	1.019	0.054	0.145
328	0.849	0.053	0.167
329	0.677	0.052	0.152
330	0.733	0.062	0.136
331	0.554	0.062	0.161
332	0.544	0.071	0.231
333	0.522	0.069	0.199
334	0.326	0.032	0.105
335	0.435	0.030	0.107
336	0.494	0.029	0.068
337	0.598	0.032	0.085
338	0.637	0.031	0.095
339	0.578	0.030	0.082
340	0.651	0.032	0.079
341	0.639	0.032	0.089
342	0.636	0.032	0.079
343	0.637	0.030	0.088
344	0.606	0.030	0.101
345	0.581	0.030	0.064
346	0.543	0.030	0.075
347	0.991	0.046	0.145
348	1.043	0.050	0.169
349	0.904	0.045	0.132
350	0.851	0.046	0.171
351	0.715	0.042	0.161
352	0.708	0.044	0.144
353	0.617	0.043	0.165
354	0.604	0.042	0.121
355	0.519	0.042	0.112
356	0.432	0.038	0.144
357	0.726	0.059	0.170
358	0.476	0.062	0.248

A machine-readable version of Table I is provided as the text file `xsec_summary_table.txt`. The first line of this file contains the string `numXbins` followed by the number of bins (359) used to present the final measurement. The following lines match the contents of Table I (without the column headings), but the numerical values are reported to the full precision adopted in the C++ code used to execute the analysis.

The 359×359 covariance matrix describing the total uncertainty on the measured $\langle\sigma\rangle_\mu$ values is too large to conveniently tabulate in this document. However, the left-hand panel of Fig. 1 presents a plot of the total covariance matrix elements. The right-hand panel gives the corresponding correlation matrix, whose elements are computed according to the formula

$$\mathrm{Corr}\big(\langle\sigma\rangle_\mu, \langle\sigma\rangle_\nu\big) = \frac{\mathrm{Cov}\big(\langle\sigma\rangle_\mu, \langle\sigma\rangle_\nu\big)}{\mathrm{Cov}\big(\langle\sigma\rangle_\mu, \langle\sigma\rangle_\mu\big) \cdot \mathrm{Cov}\big(\langle\sigma\rangle_\nu, \langle\sigma\rangle_\nu\big)} \,. \tag{2}$$

A machine-readable table of the elements of the total covariance matrix is provided in the `mat_table_cov_total.txt` file. The first two lines of the file contain the strings `numXbins` and `numYbins`, respectively, each followed by the total number of bins reported (359). The third line provides column labels (`xbin`, `ybin`, and `z`) for the numerical data that follow. The remaining lines of the file list a row (μ) and column (ν) index followed by the corresponding total covariance matrix element $\mathrm{Cov}(\langle\sigma\rangle_\mu, \langle\sigma\rangle_\nu)$ in units of 10^{-76} cm^4.

In addition to the total covariance matrix, several of its most important components are also provided in separate text files. These include `mat_table_cov_detVar_total.txt`, `mat_table_cov_flux.txt`, and `mat_table_cov_xsec_total.txt`,

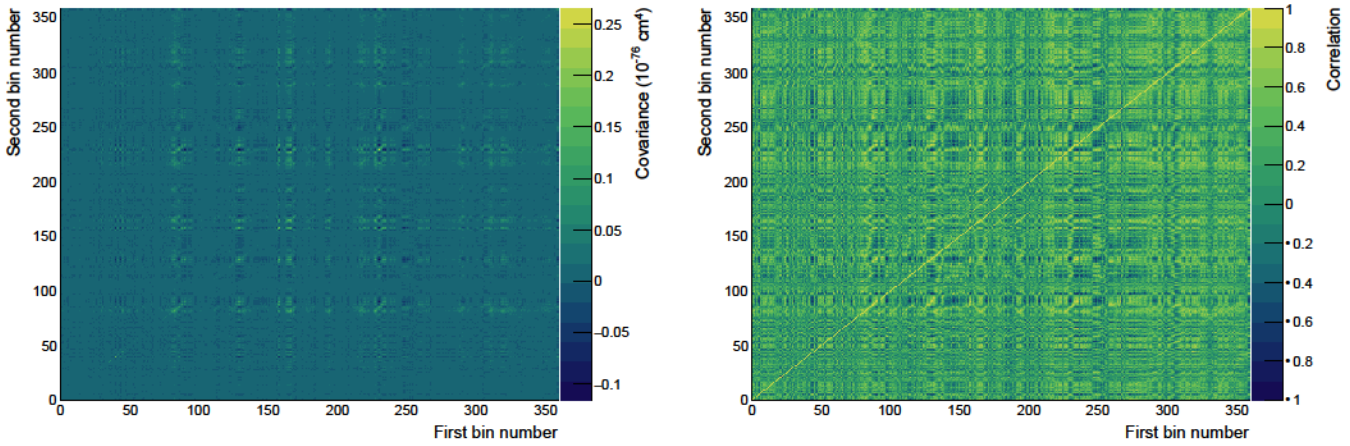

FIG. 1. The total covariance matrix (left) and correlation matrix (right) for the flux-averaged total cross sections measured in the analysis.

which respectively tabulate the covariances on the measured cross sections due to systematic uncertainties related to the detector response, neutrino flux prediction, and neutrino interaction model. In many bins, the portion of the interaction model covariance estimated by using NuWro as an alternative event generator (see Sec. VA of main text) is the leading source of systematic uncertainty. For reference, this contribution to the total covariance matrix is tabulated individually in the text file `mat_table_cov_NuWroGenie.txt`. It is already included in the overall interaction model covariance matrix reported in `mat_table_cov_xsec_total.txt`. All of these partial covariance matrix files use the same units (10^{-76} cm^4) as the total covariance matrix.

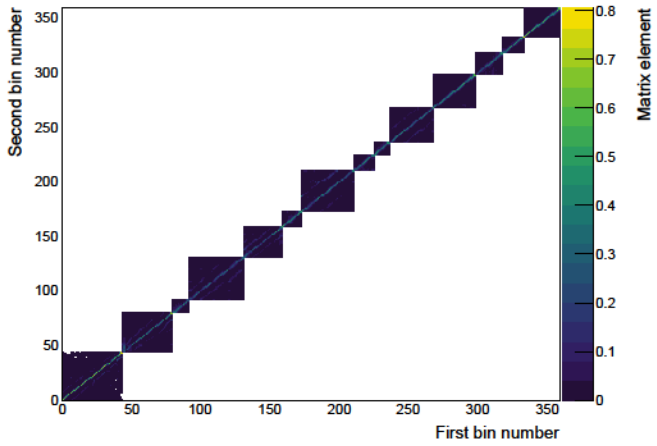

FIG. 2. The additional smearing matrix A_C.

As discussed in Sec. VI A of the main text, a theoretical prediction of the vector of flux-averaged total cross sections $\langle\sigma\rangle_\mu$ should be multiplied by the additional smearing matrix A_C before being directly compared to the data in Table I. Figure 2 displays the block diagonal structure of A_C using a color scheme in which matrix elements that are identically zero are rendered as white squares. The file `mat_table_add_smear.txt` provides a machine-readable list of the additional smearing matrix elements using the same format as the total covariance matrix file (`mat_table_cov_total.txt`). However, note that the numerical values in the final column are now dimensionless.

To illustrate how these text files may be manipulated to compare a theoretical prediction to the full data set, an example C++ program is provided in the file `calc_chi2.C`. The program relies on the `TMatrixD` class defined by ROOT and must either be executed using the ROOT C++ interpreter or be compiled against the ROOT shared libraries. The `calc_chi2.C` program loads tables of the measured $\langle\sigma\rangle_\mu$ values, their covariances, and the elements of A_C. It also loads a table of theoretical $\langle\sigma\rangle_\mu$ values (stored in the text file `vec_table_uBTune.txt`) predicted by the MicroBooNE Tune interaction model described in the main text. The overall χ^2 goodness-of-fit metric obtained for the MicroBooNE Tune model in the main text is then reproduced and printed to the terminal.

A similar program is provided in the file `calc_chi2.py` for users who prefer to work with the Python programming language. In this case, the program depends on the NumPy package but not on ROOT. Within the numerical precision printed to the terminal, it is expected to produce the same output as the example C++ program.

By replacing the numerical $\langle\sigma\rangle_\mu$ values in the file `vec_table_uBTune.txt` and rerunning either `calc_chi2.C` or `calc_chi2.py`, one may immediately compute an overall χ^2 score for a comparison of an alternate cross-section calculation to the measured data points. The replacement $\langle\sigma\rangle_\mu$ values need not have the same numerical precision as the original ones, and they may be represented using either scientific or fixed-point notation.

The expected ν_μ flux generated by the Fermilab Booster Neutrino Beam at the location of MicroBooNE is tabulated in the file `microboone_numu_flux.txt`, which has been duplicated from the supplemental materials included with Ref. [2]. Theoretical predictions of the total cross sections $\langle\sigma\rangle_\mu$ should be averaged over the neutrino energy distribution given therein.

II. MIGRATION MATRICES

The *migration matrix* $M_{j\mu}$ defined in Eq. 12 of the main text quantifies smearing effects in the reconstruction of physics observables measured in the present analysis. Plots of the migration matrices for each block of bins used to report the final results are given in the figures below.

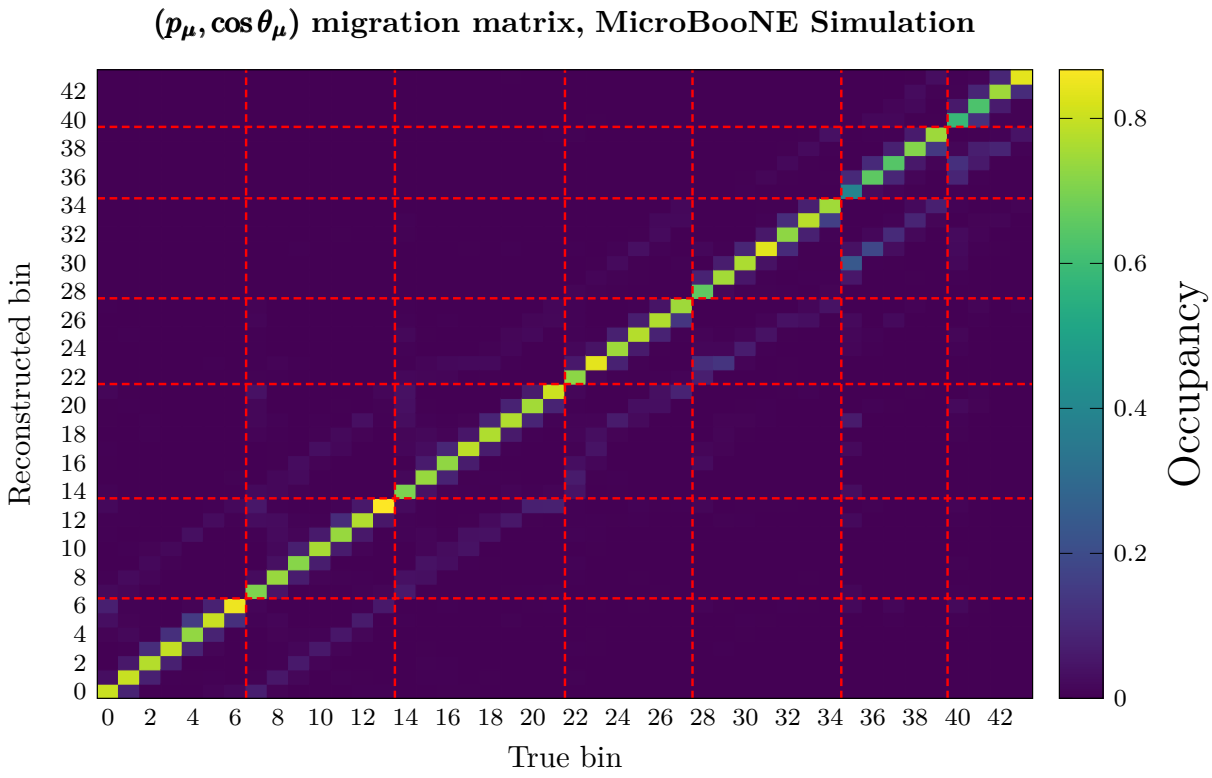

FIG. 3. Migration matrix for block #0 of bins used for the double-differential measurement of $(p_\mu, \cos\theta_\mu)$. Dashed red lines indicate momentum bin boundaries.

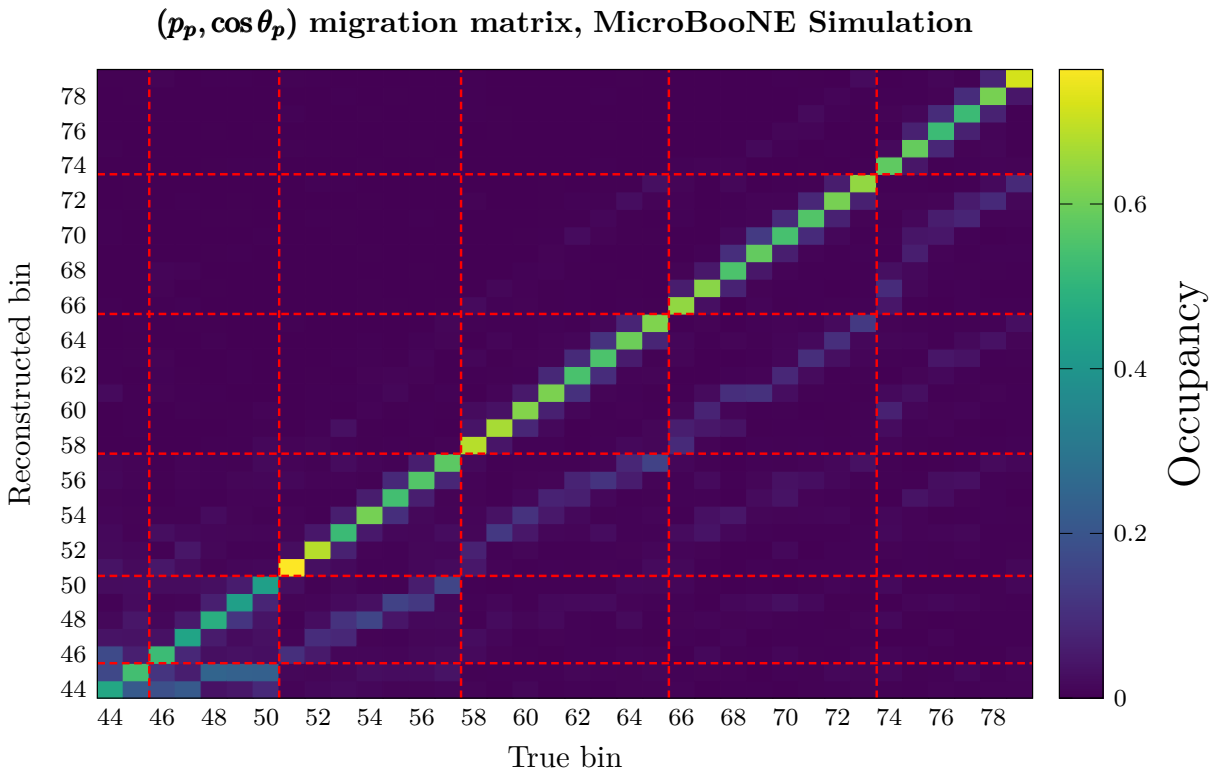

FIG. 4. Migration matrix for block #1 of bins used for the double-differential measurement of $(p_p, \cos\theta_p)$. Dashed red lines indicate momentum bin boundaries.

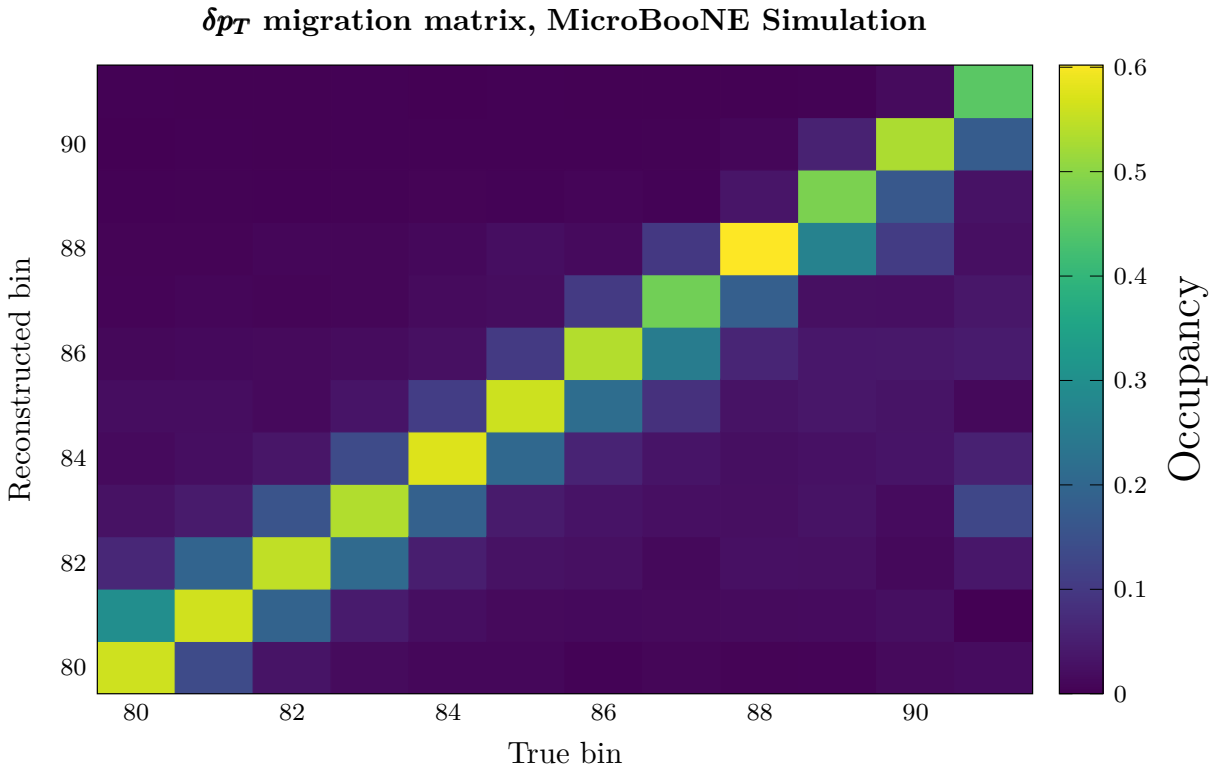

FIG. 5. Migration matrix for block #2 of bins used for the single-differential measurement of δp_T.

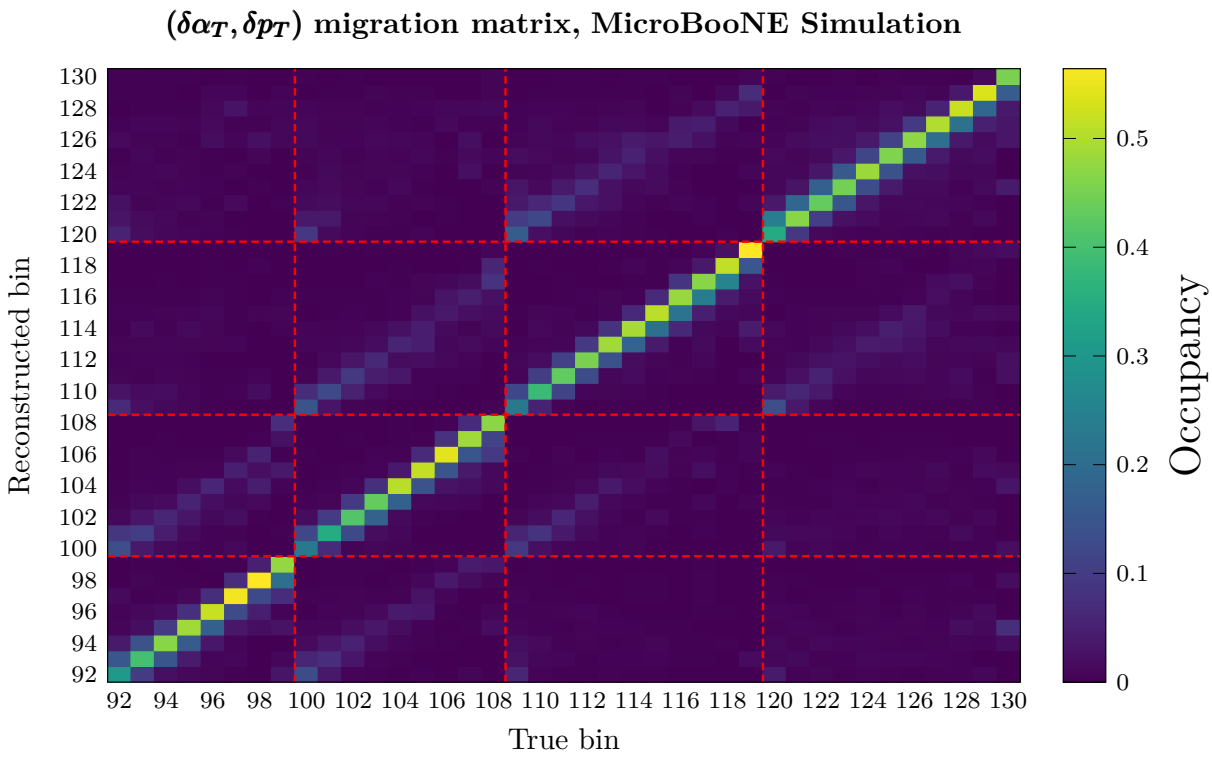

FIG. 6. Migration matrix for block #3 of bins used for the double-differential measurement of $(\delta\alpha_T, \delta p_T)$. Dashed red lines indicate $\delta\alpha_T$ bin boundaries.

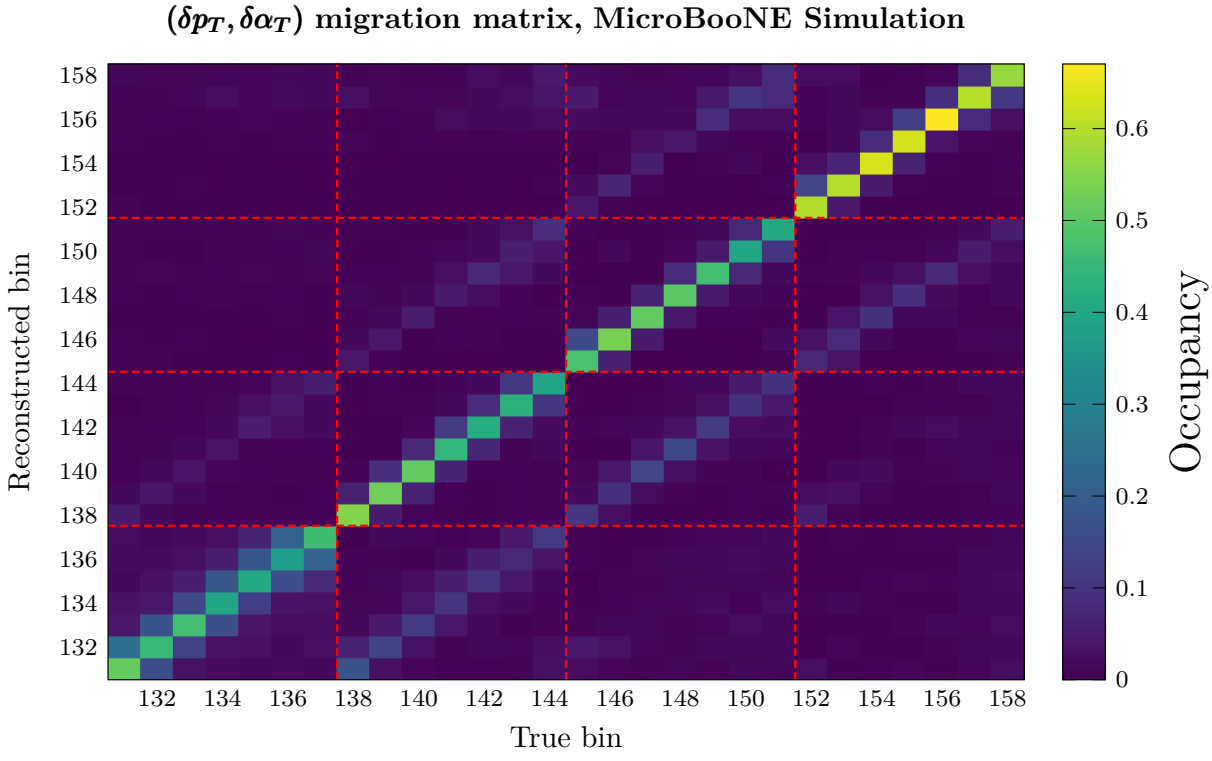

FIG. 7. Migration matrix for block #4 of bins used for the double-differential measurement of $(\delta p_T, \delta\alpha_T)$. Dashed red lines indicate δp_T bin boundaries.

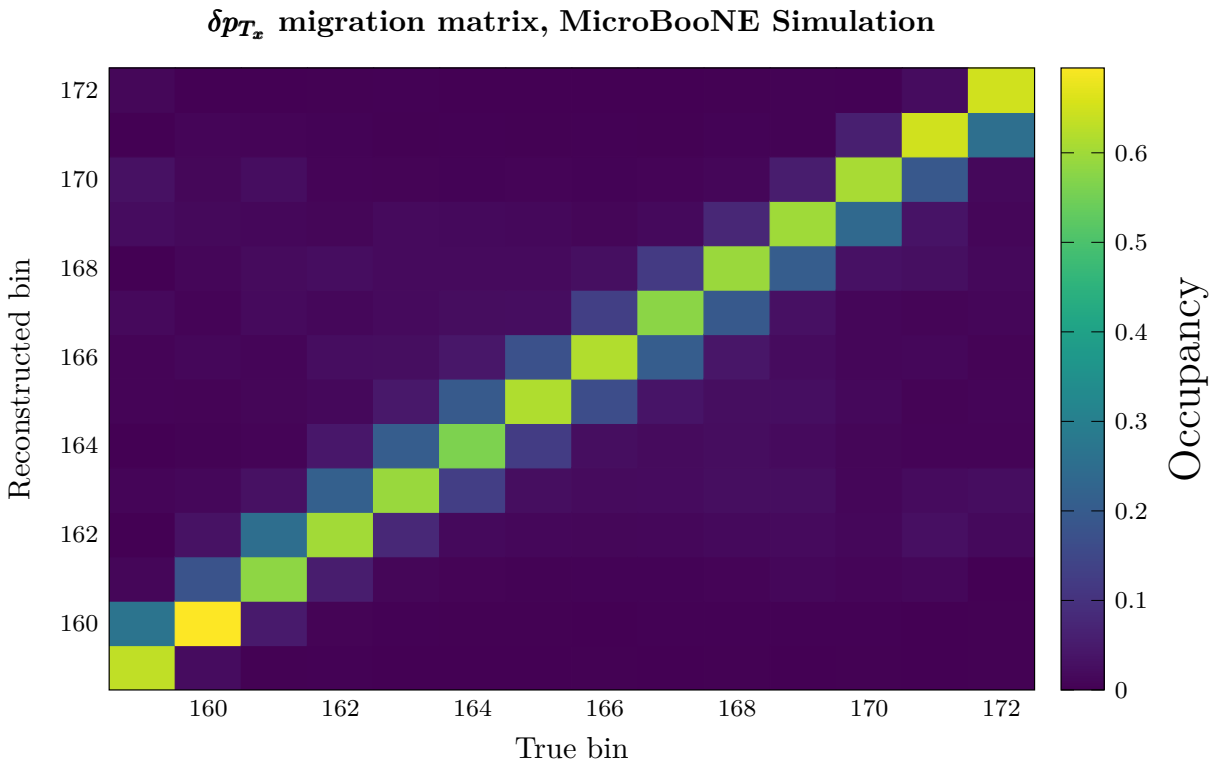

FIG. 8. Migration matrix for block #5 of bins used for the single-differential measurement of δp_{T_x}.

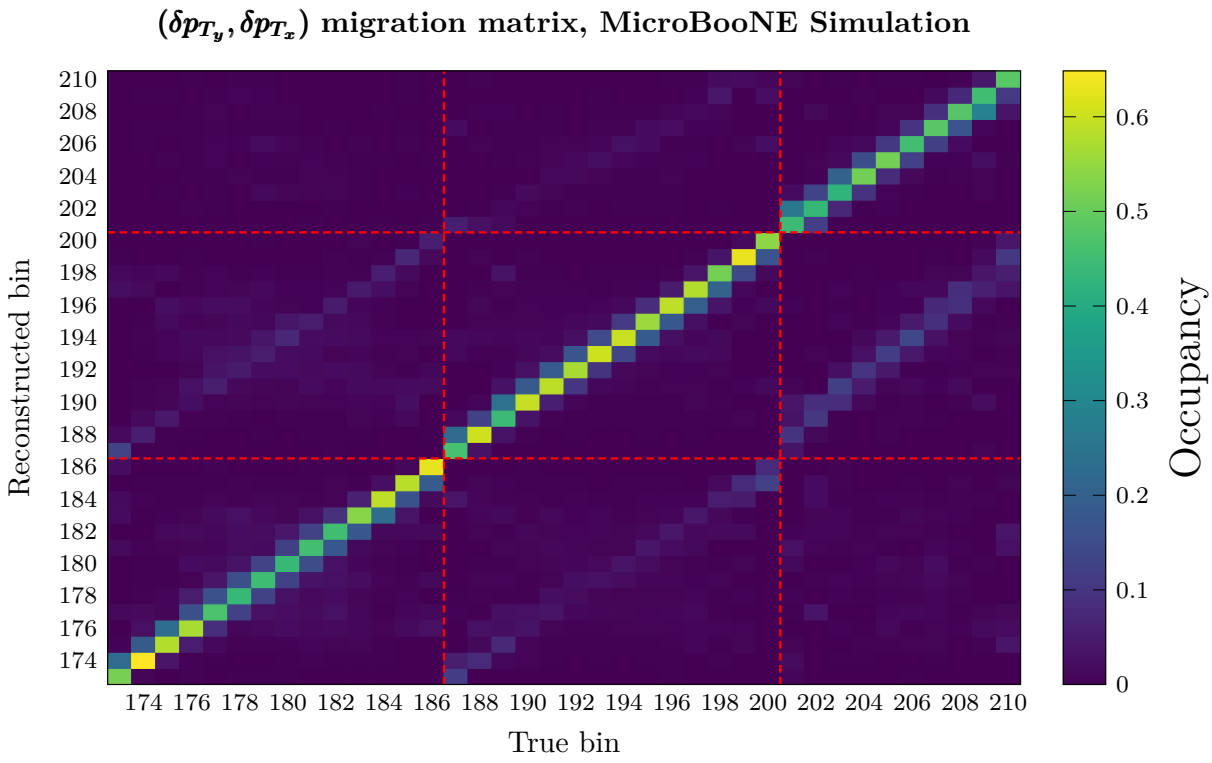

FIG. 9. Migration matrix for block #6 of bins used for the double-differential measurement of $(\delta p_{T_y}, \delta p_{T_x})$. Dashed red lines indicate δp_{T_y} bin boundaries.

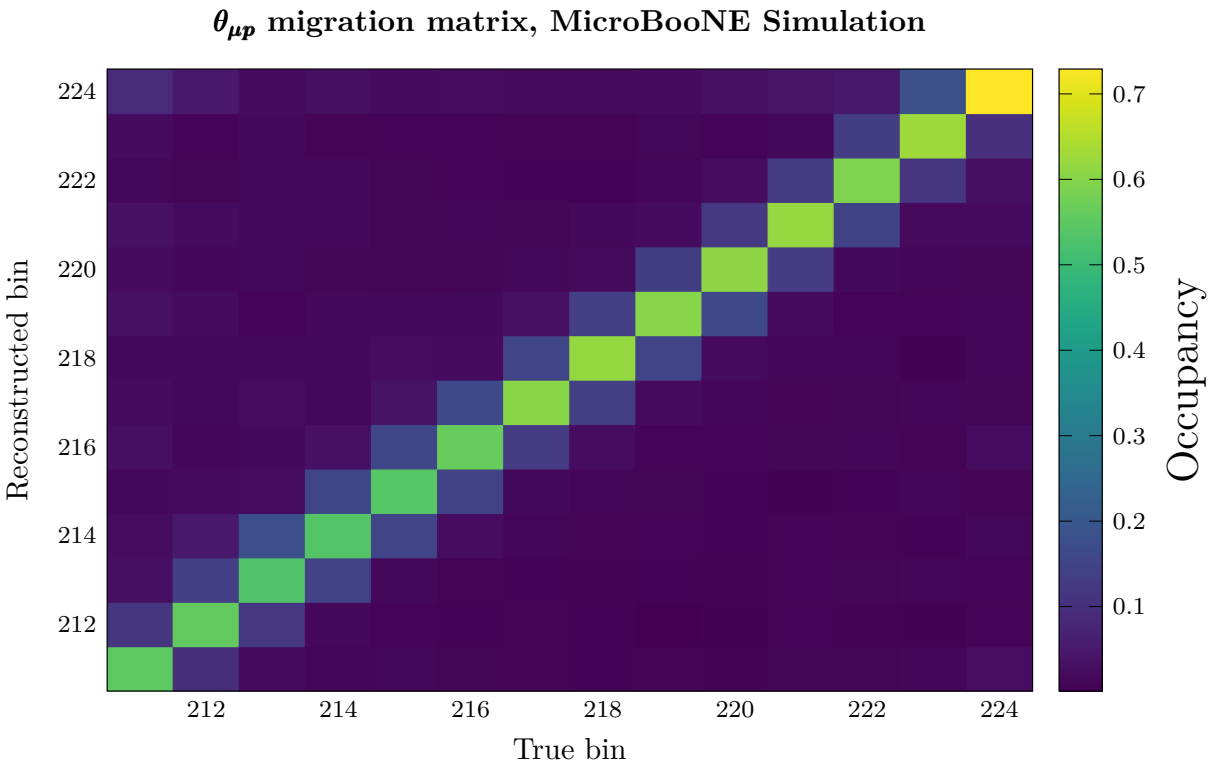

FIG. 10. Migration matrix for block #7 of bins used for the single-differential measurement of $\theta_{\mu p}$.

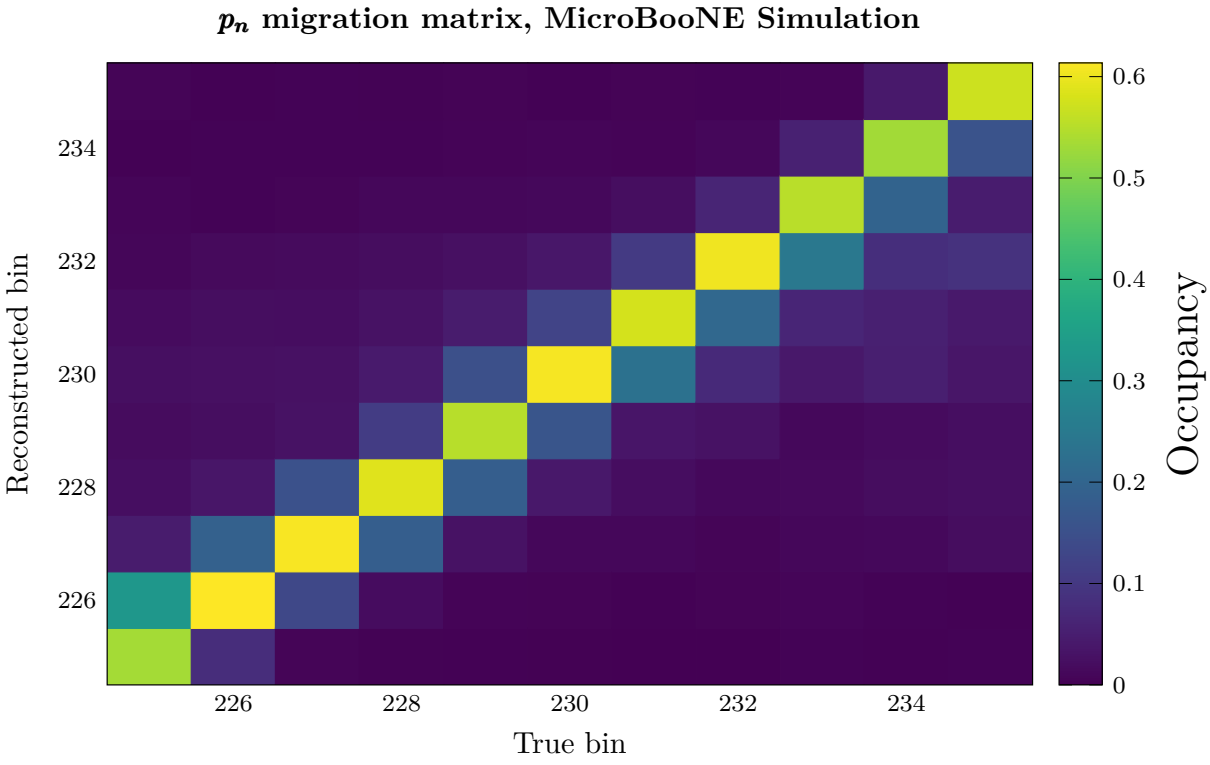

FIG. 11. Migration matrix for block #8 of bins used for the single-differential measurement of p_n.

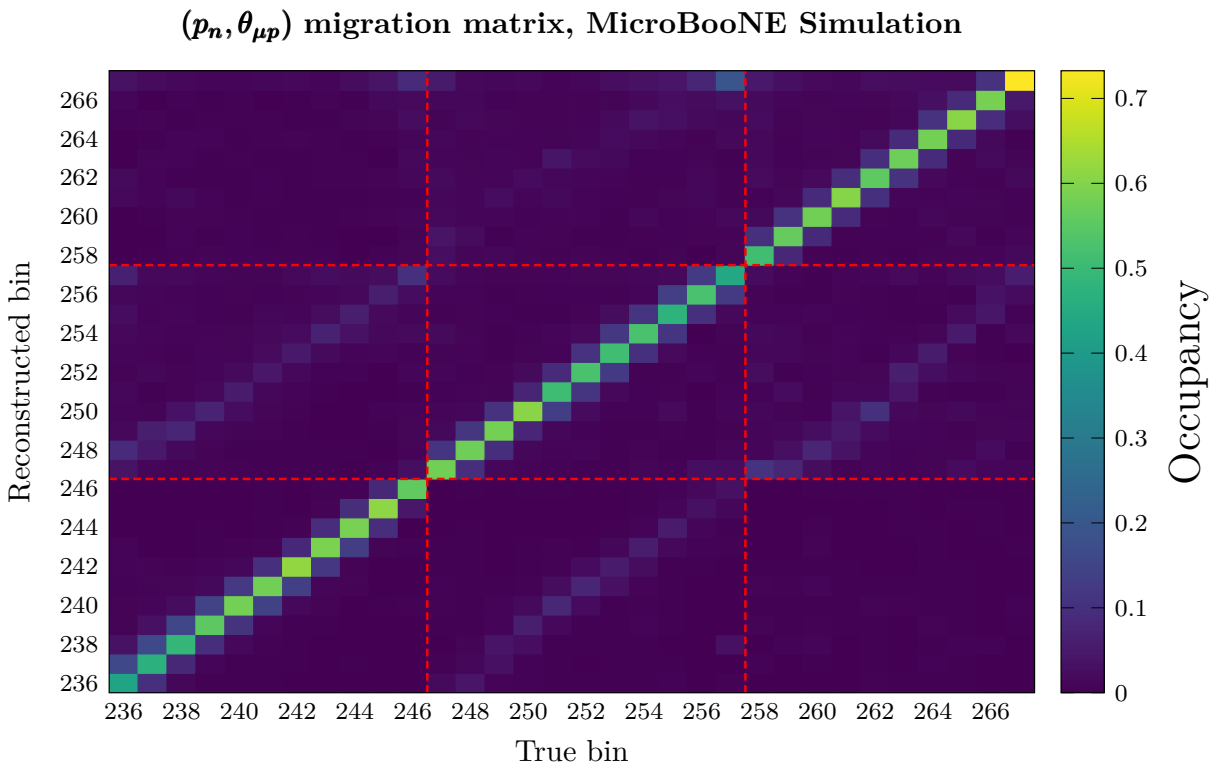

FIG. 12. Migration matrix for block #9 of bins used for the double-differential measurement of $(p_n, \theta_{\mu p})$. Dashed red lines indicate p_n bin boundaries.

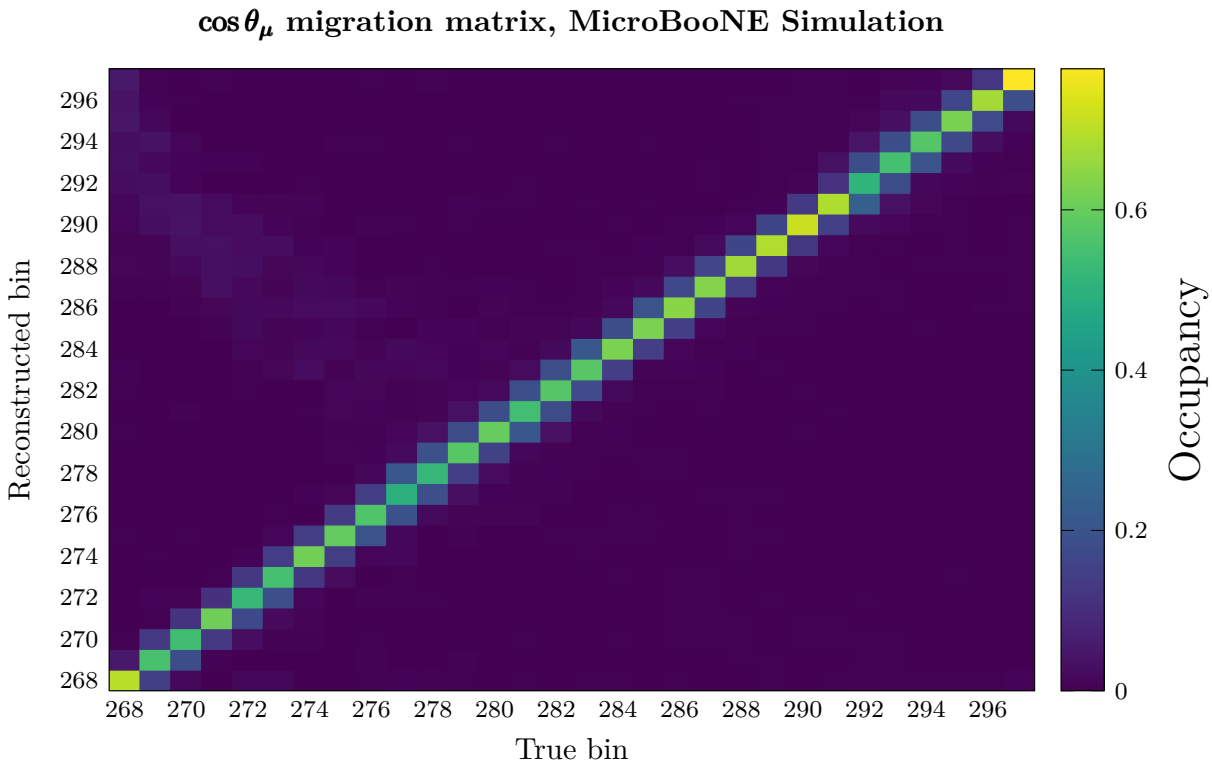

FIG. 13. Migration matrix for block #10 of bins used for the single-differential measurement of $\cos\theta_\mu$.

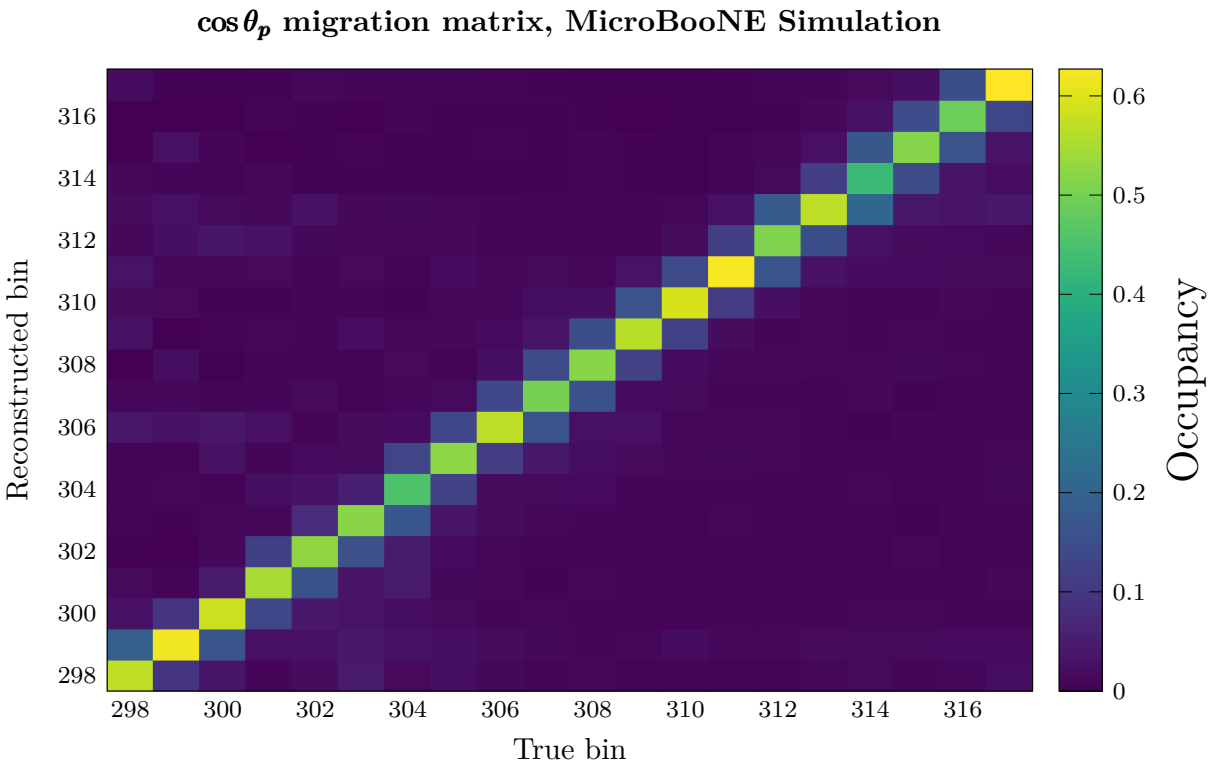

FIG. 14. Migration matrix for block #11 of bins used for the single-differential measurement of $\cos\theta_p$.

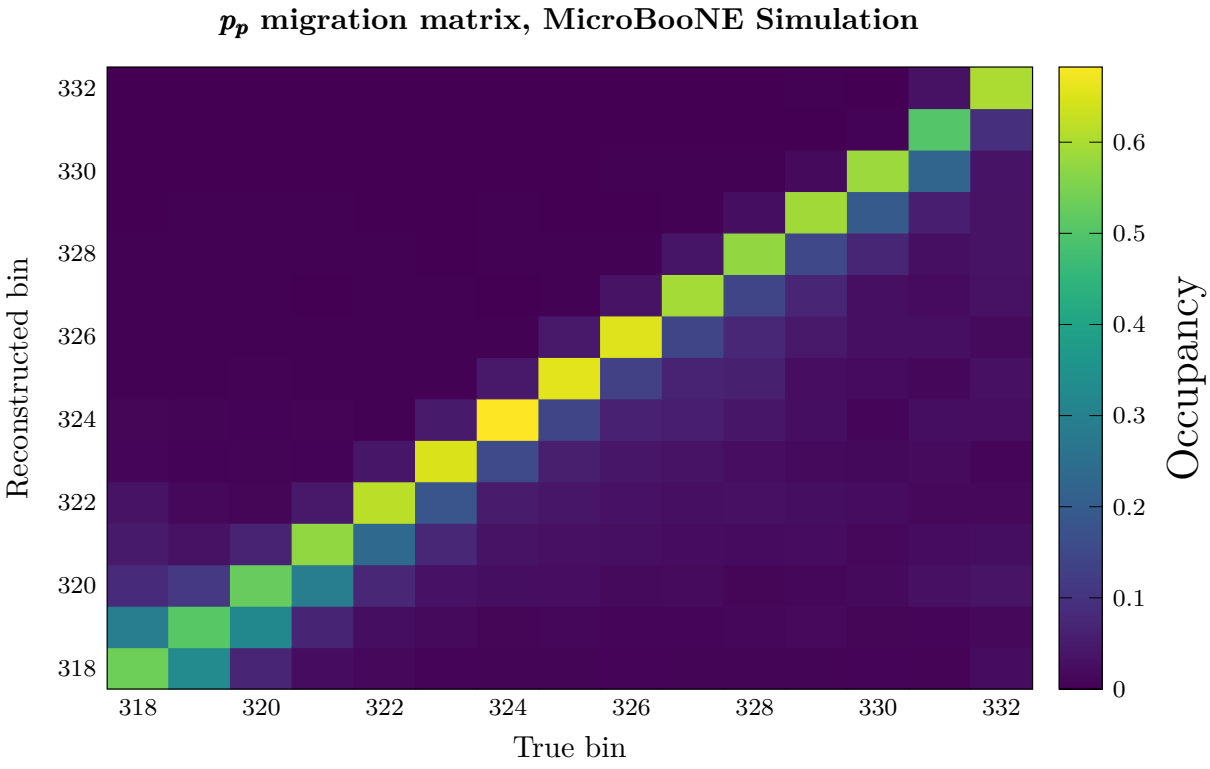

FIG. 15. Migration matrix for block #12 of bins used for the single-differential measurement of p_p.

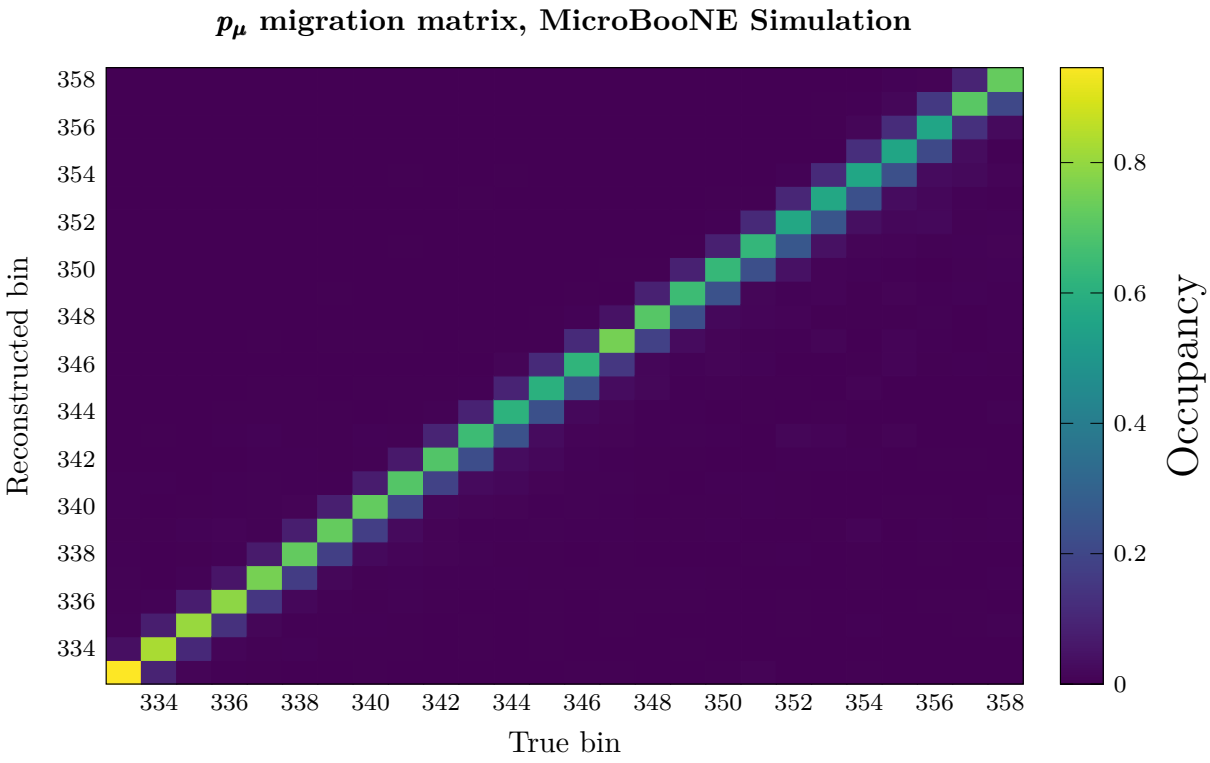

FIG. 16. Migration matrix for block #13 of bins used for the single-differential measurement of p_μ.

III. SIDEBAND STUDY RESULTS

Measured reconstructed event distributions obtained using the combined sideband selection defined in Sec. V F of the main text are shown below. The plots use the same format as those in Sec. V E of the main text.

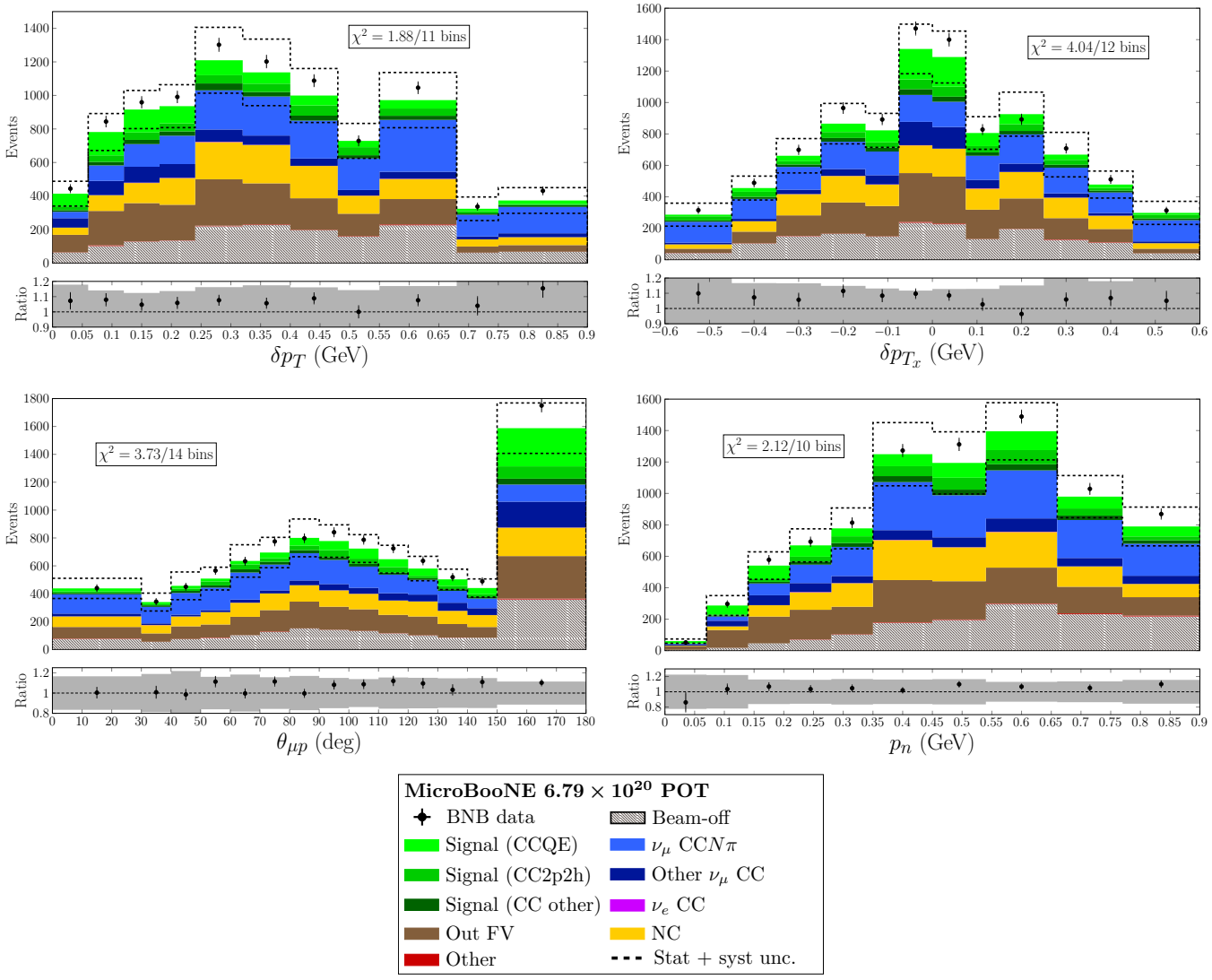

FIG. 17. Reconstructed event distributions for block #2 (δp_T, upper left), block #5 (δp_{T_x}, upper right), block #7 ($\theta_{\mu p}$, lower left), and block #8 (p_n, lower right).

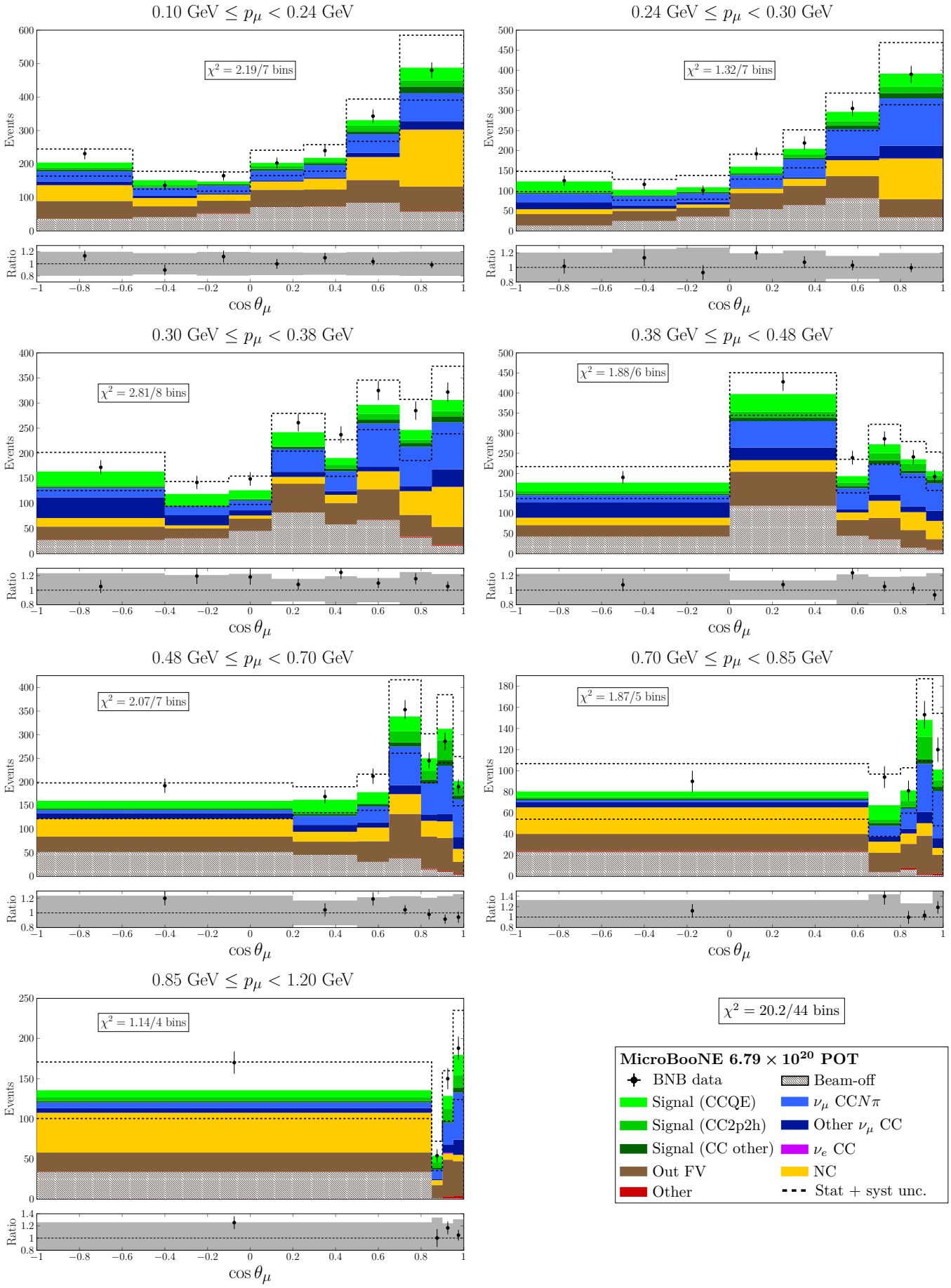

FIG. 18. Reconstructed event distributions for block #0 ($p_\mu, \cos\theta_\mu$).

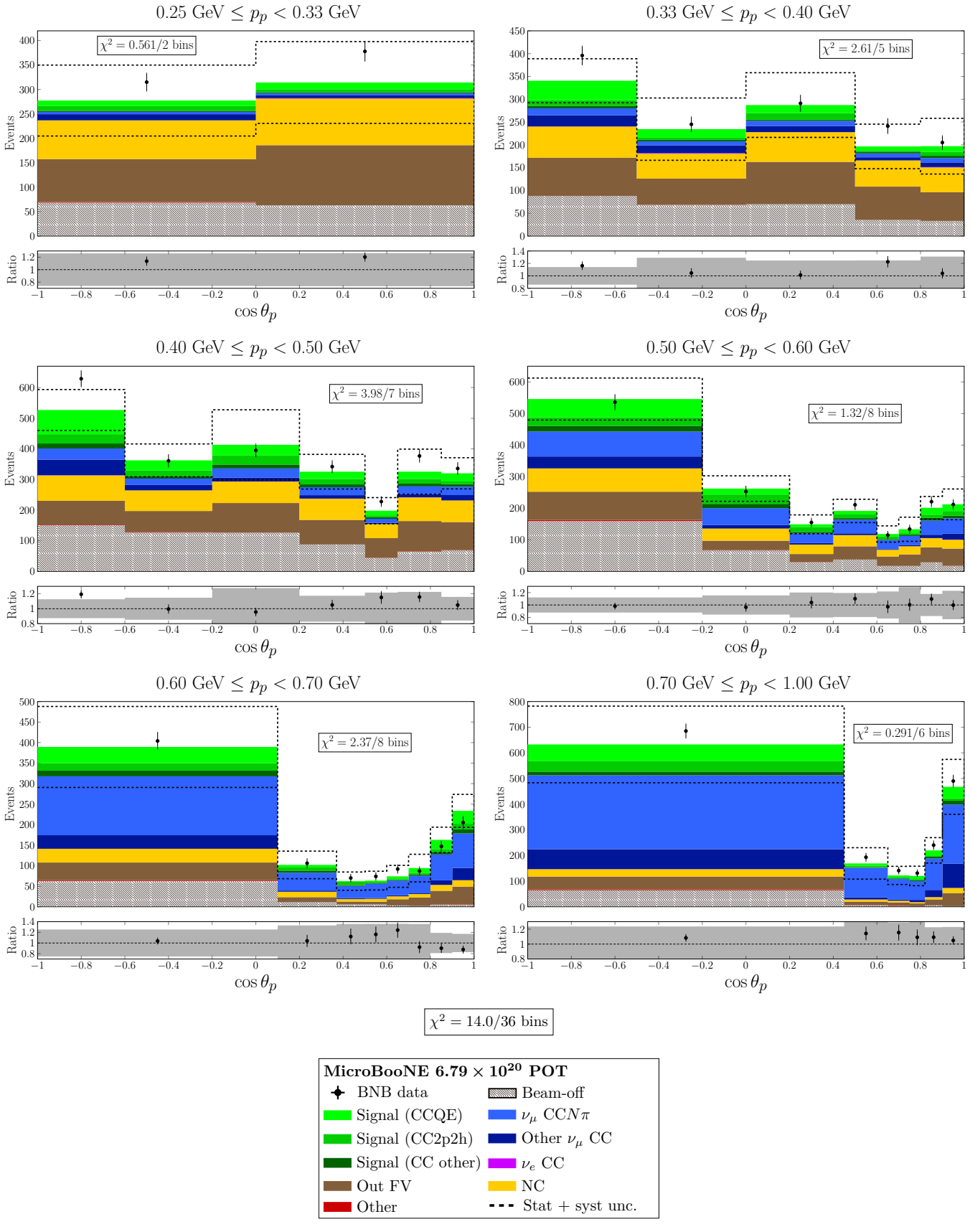

FIG. 19. Reconstructed event distributions for block #1 ($p_p, \cos\theta_p$).

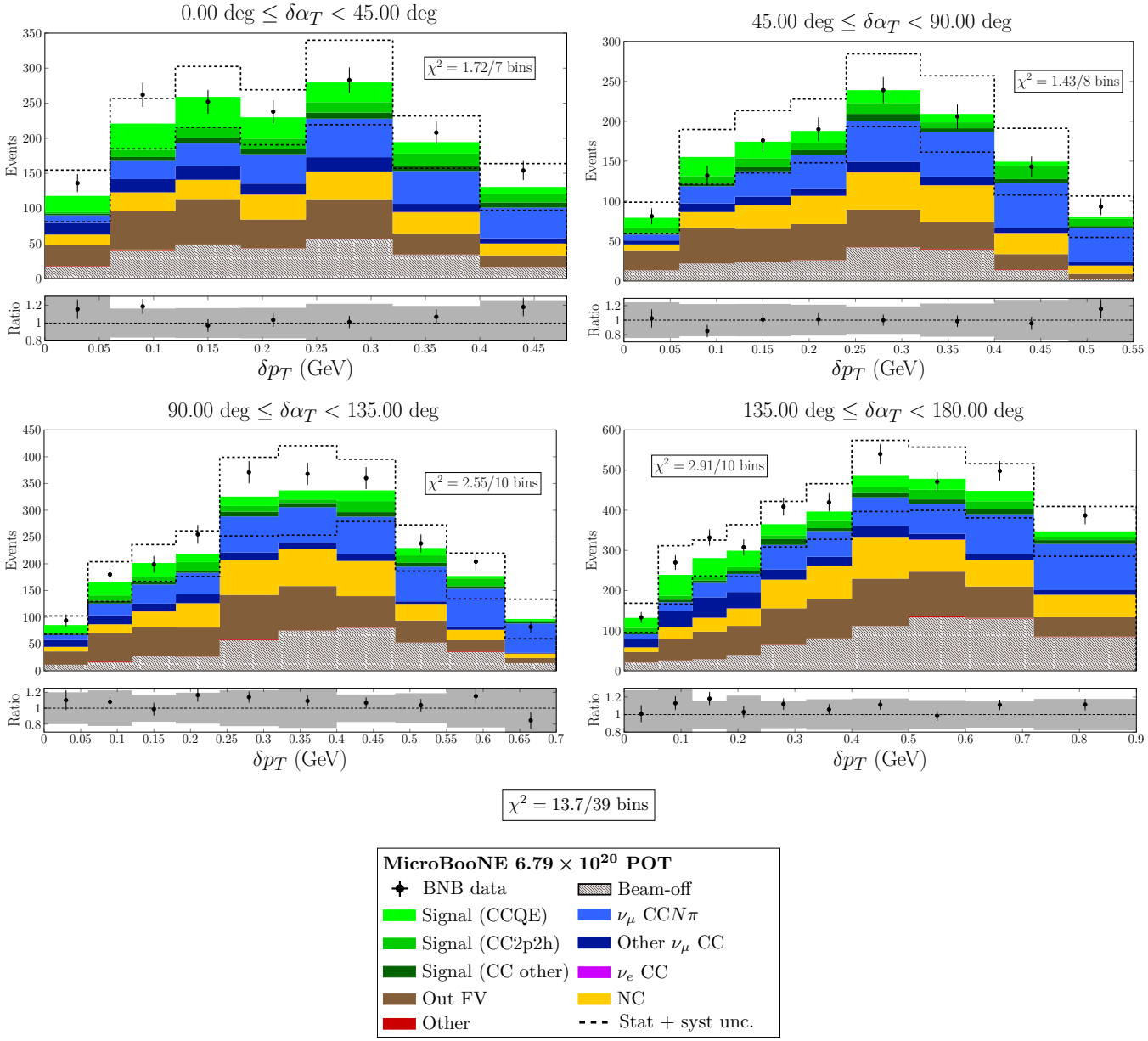

FIG. 20. Reconstructed event distributions for block #3 ($\delta\alpha_T, \delta p_T$). The overall χ^2 value includes contributions from four δp_T overflow bins that are not plotted.

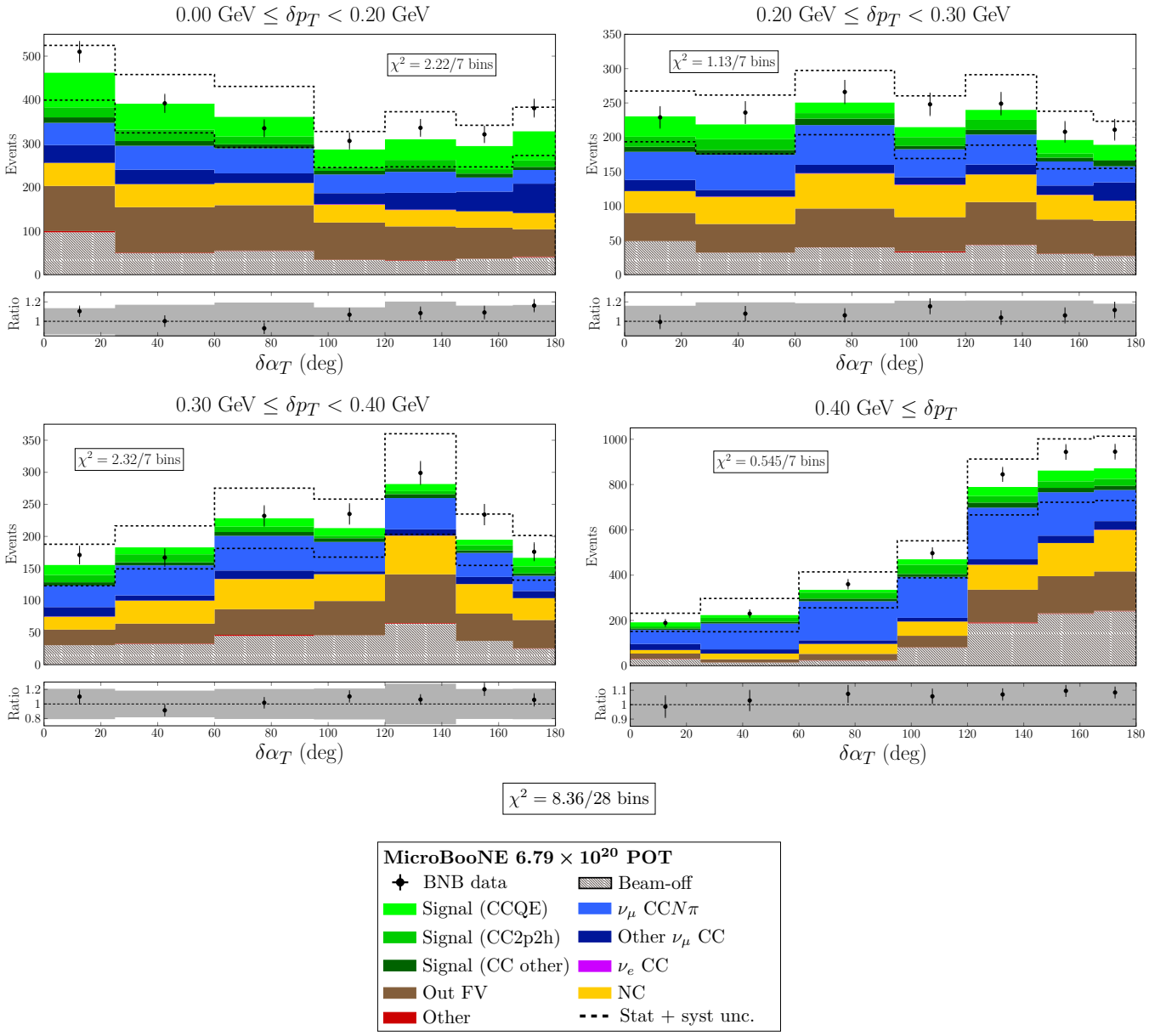

FIG. 21. Reconstructed event distributions for block #4 ($\delta p_T, \delta\alpha_T$).

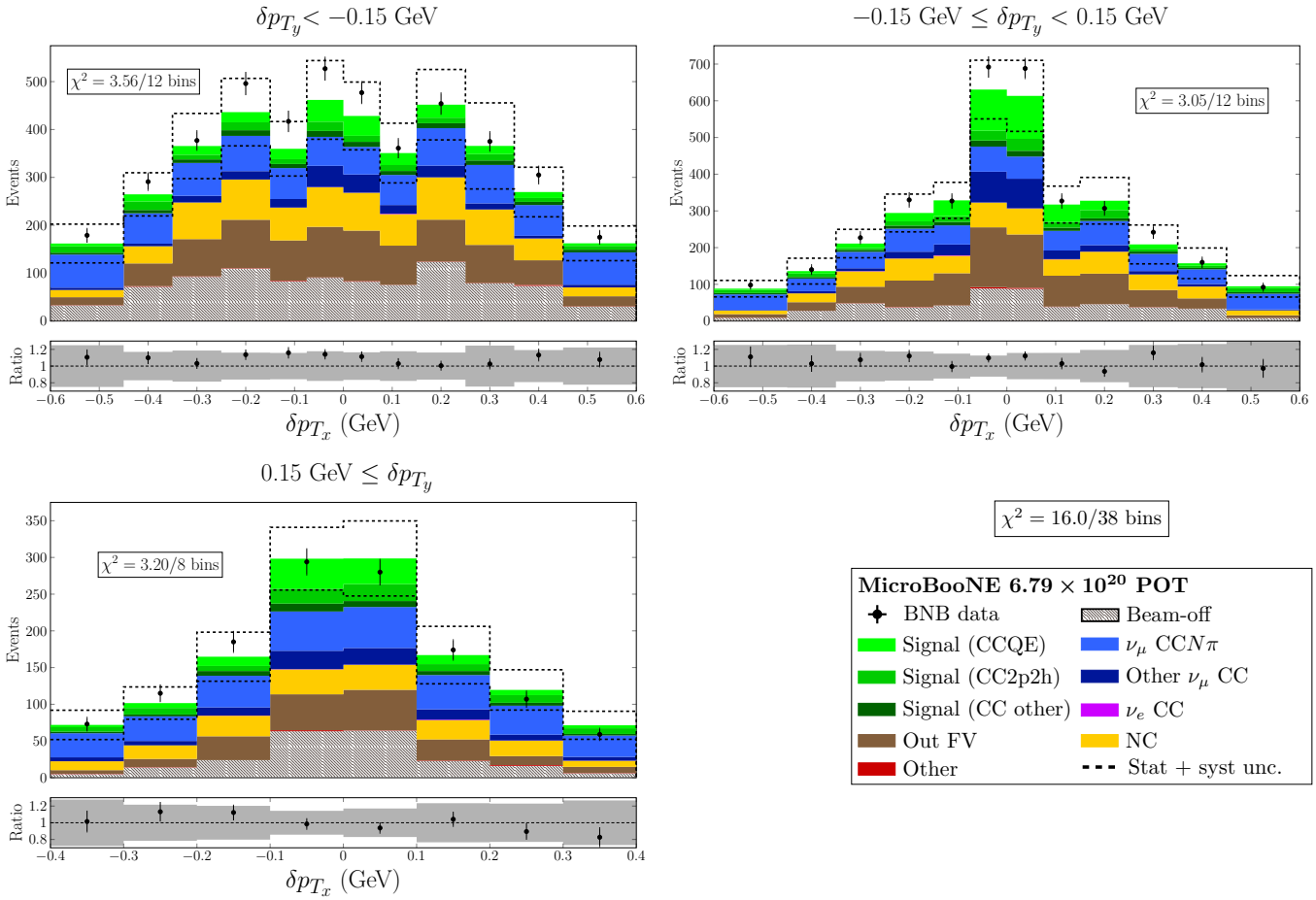

FIG. 22. Reconstructed event distributions for block #6 ($\delta p_{T_y}, \delta p_{T_x}$). The overall χ^2 value includes contributions from three underflow and three overflow δp_{T_x} bins that are not plotted.

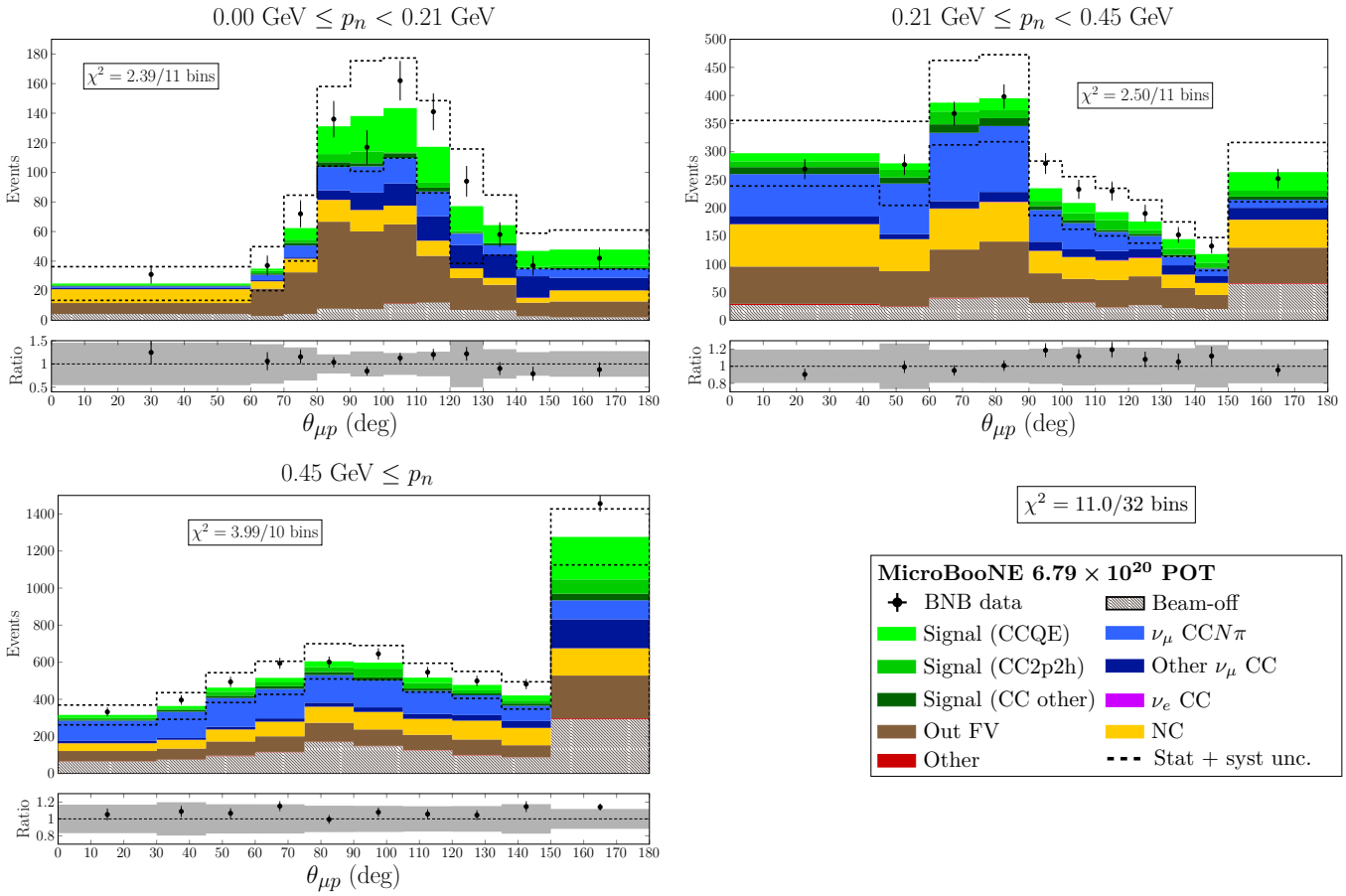

FIG. 23. Reconstructed event distributions for block #9 ($p_n, \theta_{\mu p}$).

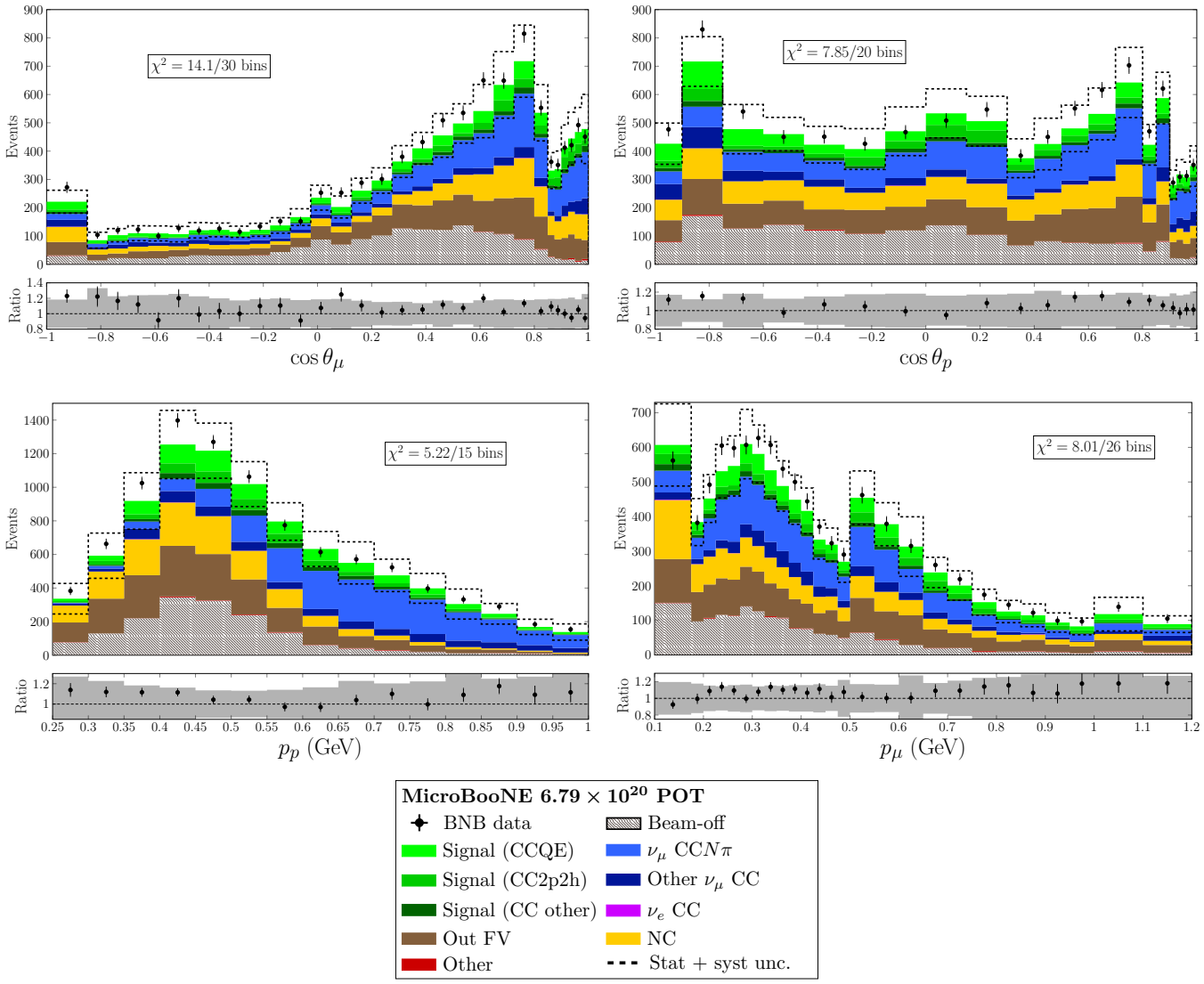

FIG. 24. Reconstructed event distributions for block #10 ($\cos\theta_\mu$, upper left), block #11 ($\cos\theta_p$, upper right), block #12 (p_p, lower left), and block #13 (p_μ, lower right).

IV. RESPONSE MATRIX

The *response matrix* Δ defined in Eq. 11 of the main text is employed in the cross-section unfolding procedure to estimate both efficiency and bin migration corrections. The elements of the matrix are tabulated in the text file `mat_table_detector_response.txt` using the reconstructed (true) bin index j (μ) along the x (y) axis. The file format is identical to the one used to report the matrices in Sec. I. Note that, like the additional smearing matrix A_C, the elements of Δ are dimensionless. A plot of the response matrix including all blocks for the full measurement is given in Fig. 25.

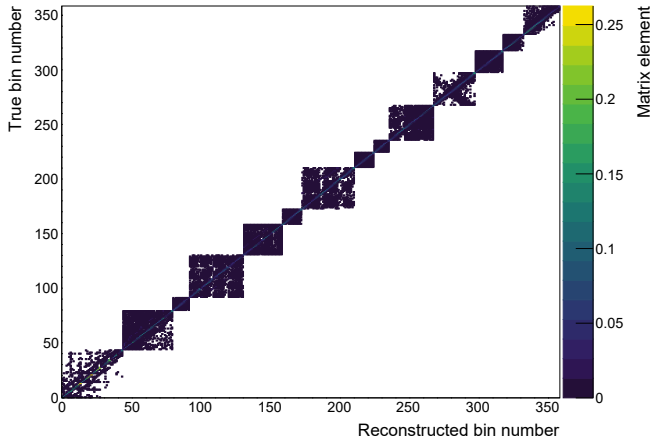

FIG. 25. The detector response matrix Δ.

V. DATA COMPARISONS TO MICROBOONE TUNE WITH MODEL UNCERTAINTY

Plots of the CC0πNp differential cross-section results shown in Sec. VII B of the main text are reproduced here with all model predictions other than the MicroBooNE Tune removed. Figures 26–39 follow the same conventions as the main text for displaying the data points in the main panel of each plot; the inner error bars represent the statistical uncertainty only, while the outer error bars also include shape-only systematic uncertainties. The remaining portion of the total measurement uncertainty is shown by the dark gray band along the x-axis.

The bottom panel of each plot displays the ratio of the measured data points to the MicroBooNE Tune prediction. The error bars on the black points in the ratio plots display the full uncertainty on the measurement.

The light gray band that appears in all panels of Figs. 26–39 displays the theoretical uncertainty on the MicroBooNE Tune prediction. This uncertainty is calculated using the same variations to the neutrino interaction model mentioned in Sec. V A of the main text. All other sources of uncertainty are omitted.

To calculate the theoretical uncertainty, the covariances between the expected signal event counts in the μ-th and ν-th true bins are evaluated via

$$V_{\mu\nu} = \frac{1}{N_{\text{univ}}} \sum_{u=1}^{N_{\text{univ}}} \left(\phi_\mu^{\text{CV}} - \phi_\mu^u\right)\left(\phi_\nu^{\text{CV}} - \phi_\nu^u\right). \tag{3}$$

Here, ϕ_μ^{CV} is the number of CC0πNp events in true bin μ predicted by the central-value MicroBooNE simulation, while ϕ_μ^u is a corresponding prediction for the u-th alternative universe. The total number of alternative universes for the systematic variation of interest is N_{univ}. Here the special prescription from Sec. V B is not followed; The signal event counts are directly varied in each alternative universe. To make them comparable to the data, the theoretical covariances from Eq. (3) have been scaled to differential cross section units and transformed using the additional smearing matrix A_C.

The legends accompanying Figs. 26–39 list a χ^2 score for the "MicroBooNE Tune with Uncertainty." The format is identical to the one used in similar legends from the main text: Each χ^2 score is separated from the number of bins for which it was calculated by a `/` character. Unlike the χ^2 scores given in the figures from the main text, however, the ones shown here include the theoretical uncertainty described above. The χ^2 calculation also accounts for the correlations between the signal prediction and the measured data points that were introduced by using the

MicroBooNE Tune model during the cross-section extraction procedure. The overall MicroBooNE Tune value of $\chi^2 = 2673$ for 359 bins (see Table II from the main text) improves to $\chi^2 = 979$ when the theoretical uncertainty is included in this way.

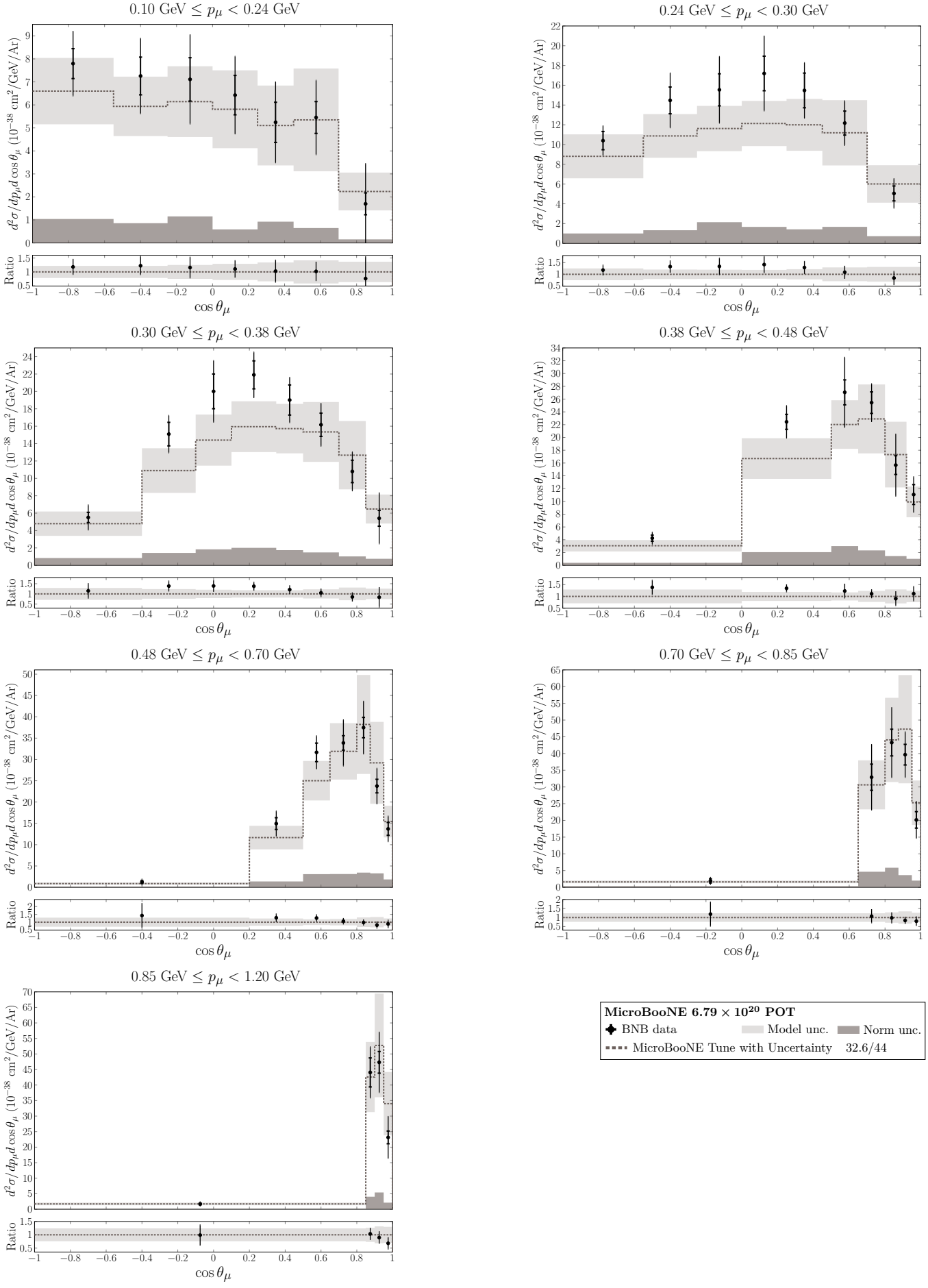

FIG. 26. Measured differential cross sections for block #0 ($p_\mu, \cos\theta_\mu$). Statistical (shape-only systematic) uncertainties are included in the inner (outer) error bars. The dark (light) gray band shows the remainder of the measurement uncertainty (theoretical uncertainty on the prediction). Error bars in the lower panels show the full measurement uncertainty.

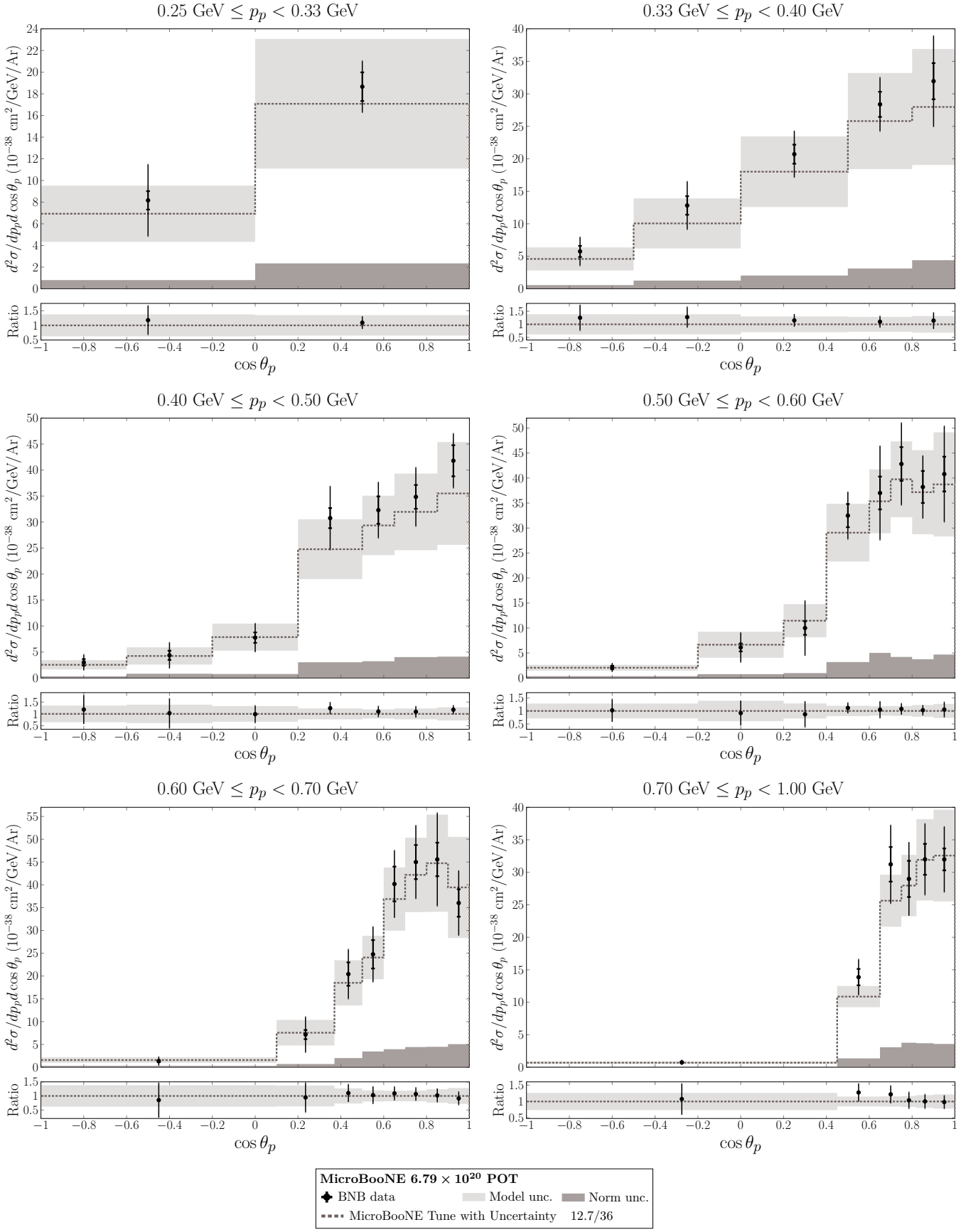

FIG. 27. Measured differential cross sections for block #1 $(p_p, \cos\theta_p)$. Statistical (shape-only systematic) uncertainties are included in the inner (outer) error bars. The dark (light) gray band shows the remainder of the measurement uncertainty (theoretical uncertainty on the prediction). Error bars in the lower panels show the full measurement uncertainty.

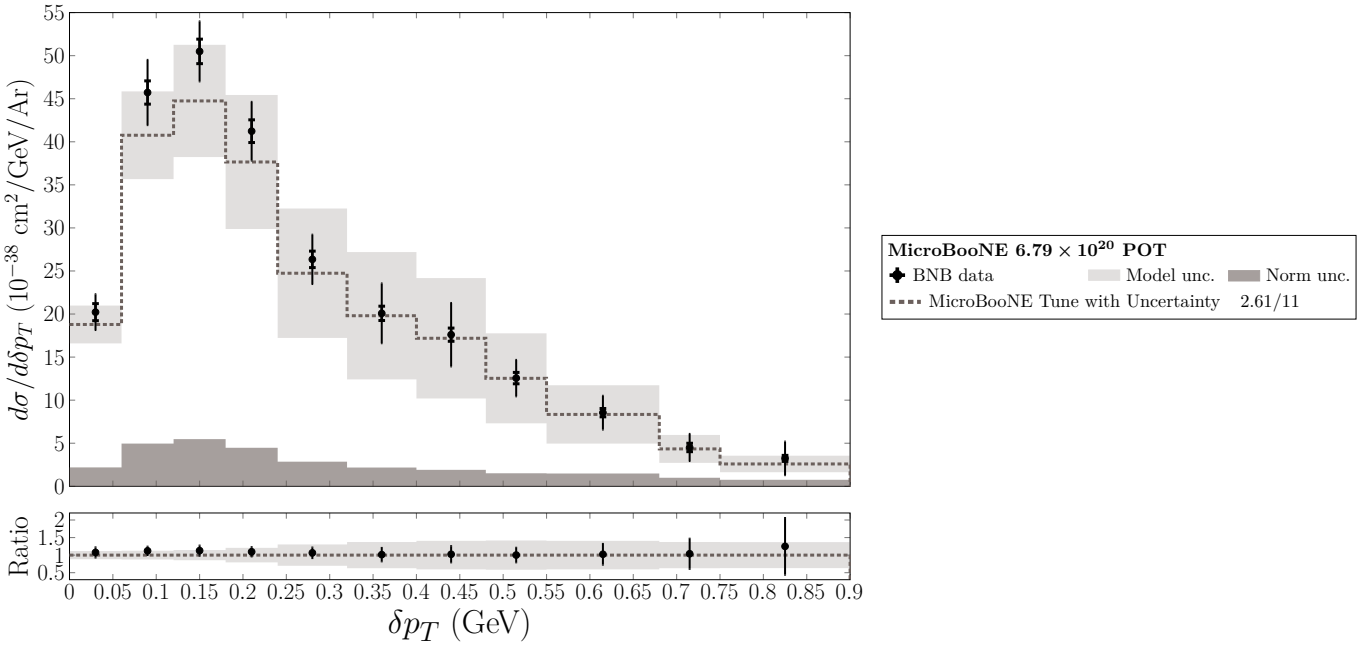

FIG. 28. Measured differential cross sections for block #2 (δp_T). Statistical (shape-only systematic) uncertainties are included in the inner (outer) error bars. The dark (light) gray band shows the remainder of the measurement uncertainty (theoretical uncertainty on the prediction). Error bars in the lower panels show the full measurement uncertainty.

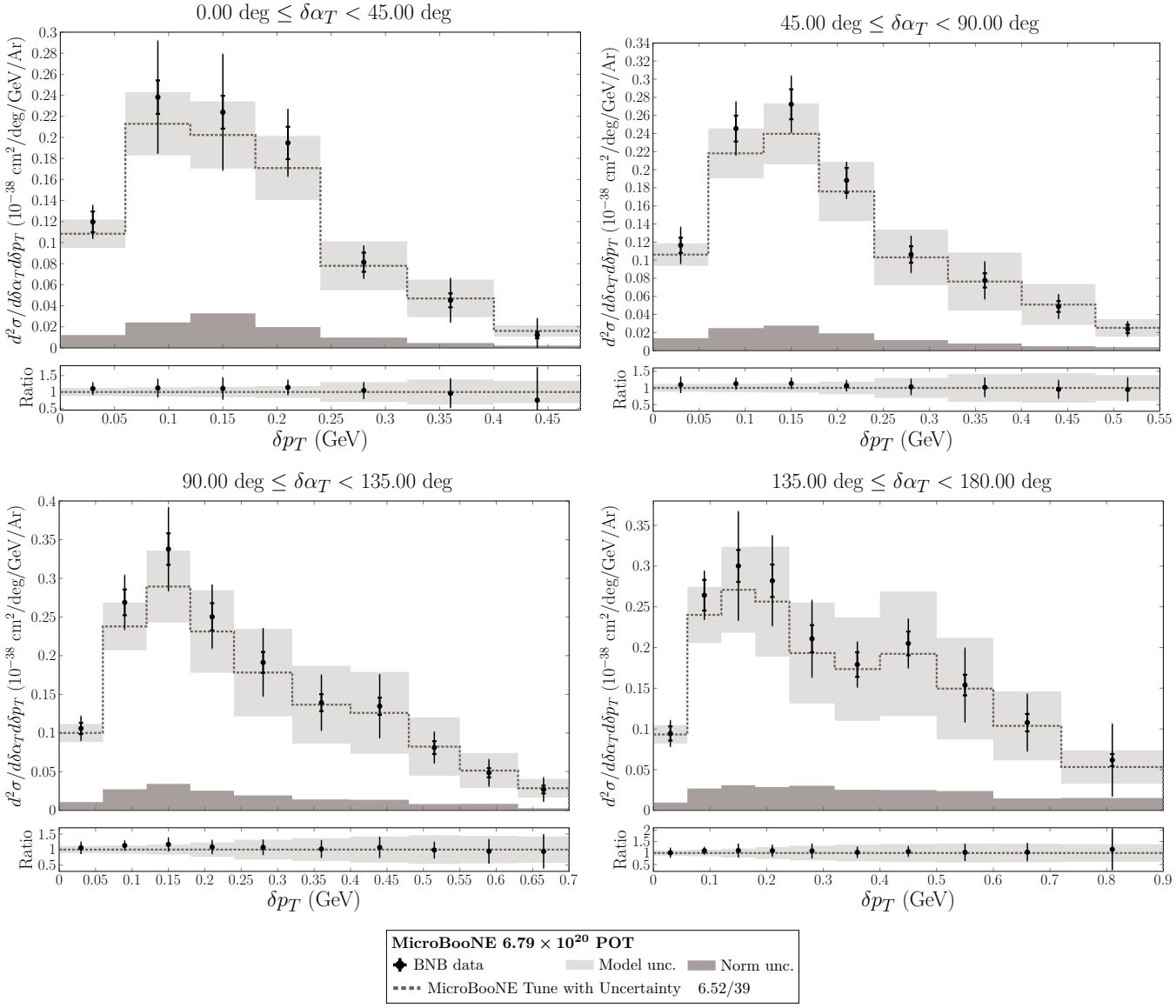

FIG. 29. Measured differential cross sections for block #3 ($\delta\alpha_T, \delta p_T$). The overall χ^2 value includes contributions from four δp_T overflow bins that are not plotted. Statistical (shape-only systematic) uncertainties are included in the inner (outer) error bars. The dark (light) gray band shows the remainder of the measurement uncertainty (theoretical uncertainty on the prediction). Error bars in the lower panels show the full measurement uncertainty.

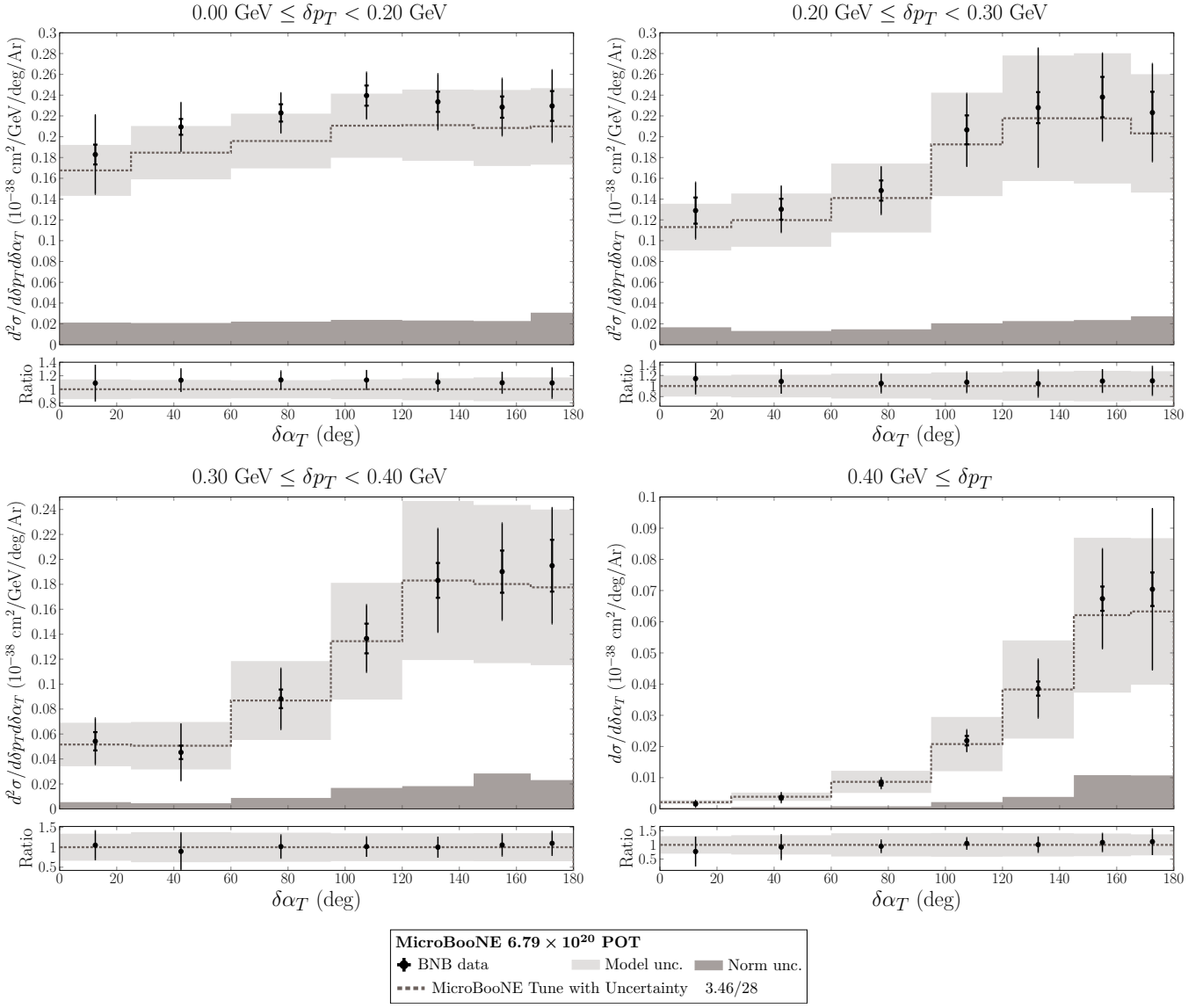

FIG. 30. Measured differential cross sections for block #4 ($\delta p_T, \delta\alpha_T$). Statistical (shape-only systematic) uncertainties are included in the inner (outer) error bars. The dark (light) gray band shows the remainder of the measurement uncertainty (theoretical uncertainty on the prediction). Error bars in the lower panels show the full measurement uncertainty.

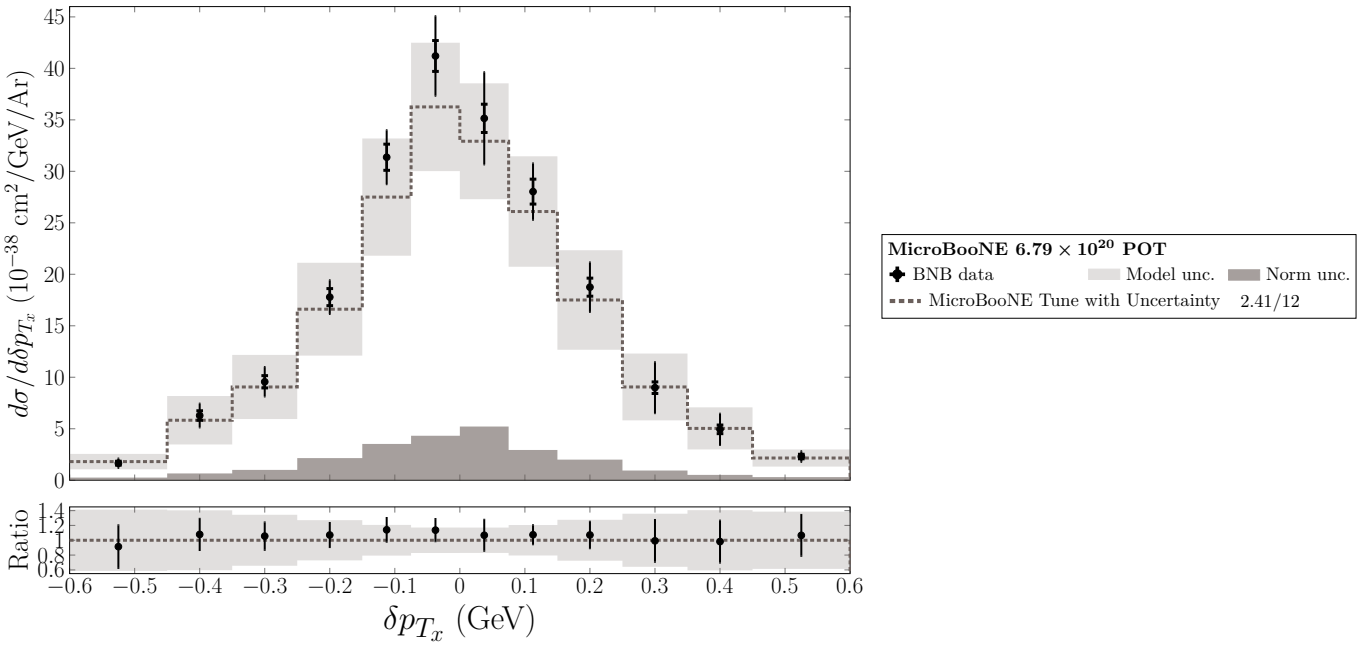

FIG. 31. Measured differential cross sections for block #5 (δp_{T_x}). Statistical (shape-only systematic) uncertainties are included in the inner (outer) error bars. The dark (light) gray band shows the remainder of the measurement uncertainty (theoretical uncertainty on the prediction). Error bars in the lower panels show the full measurement uncertainty.

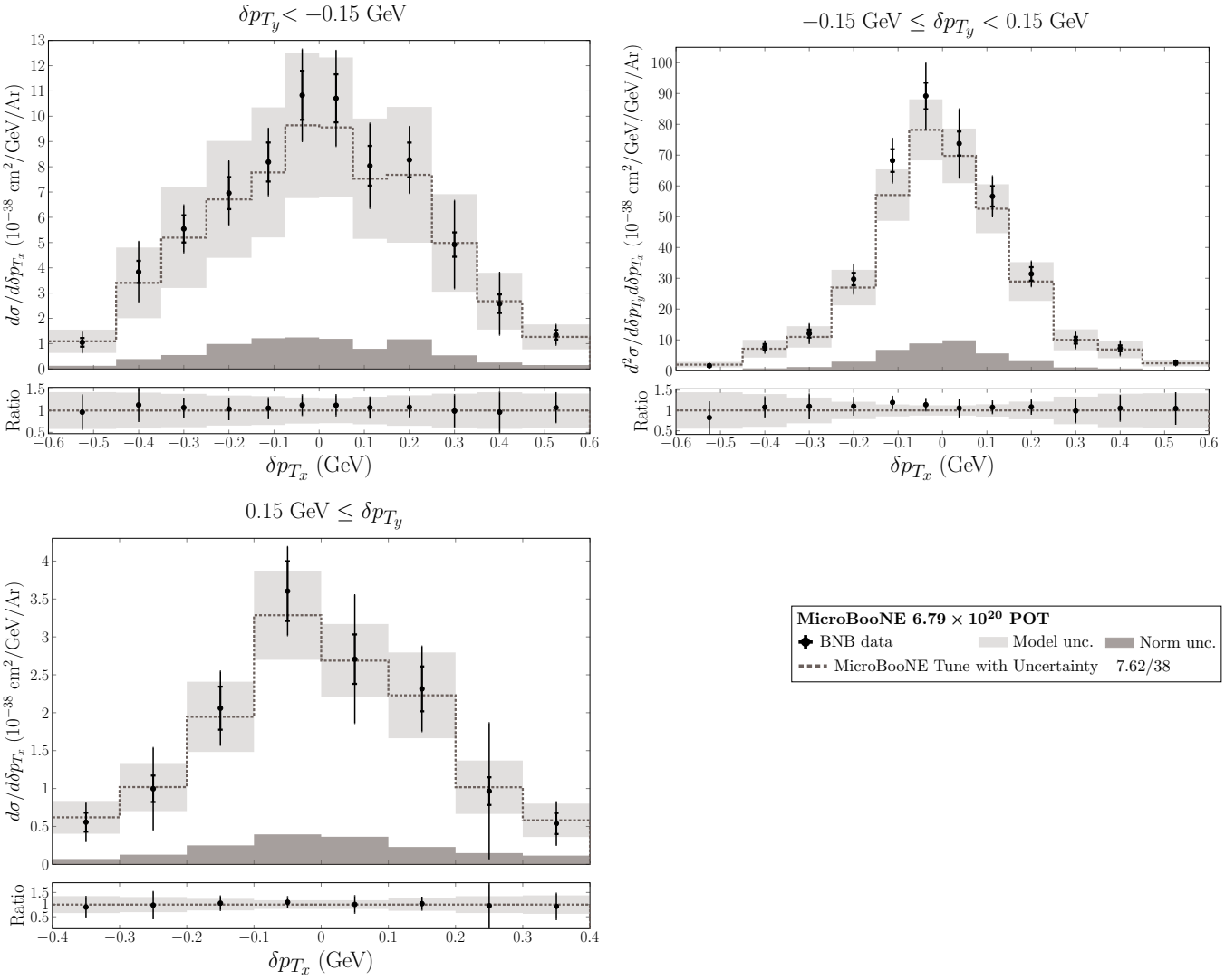

FIG. 32. Measured differential cross sections for block #6 ($\delta p_{T_y}, \delta p_{T_x}$). The overall χ^2 value includes contributions from three underflow and three overflow δp_{T_x} bins that are not plotted. Statistical (shape-only systematic) uncertainties are included in the inner (outer) error bars. The dark (light) gray band shows the remainder of the measurement uncertainty (theoretical uncertainty on the prediction). Error bars in the lower panels show the full measurement uncertainty.

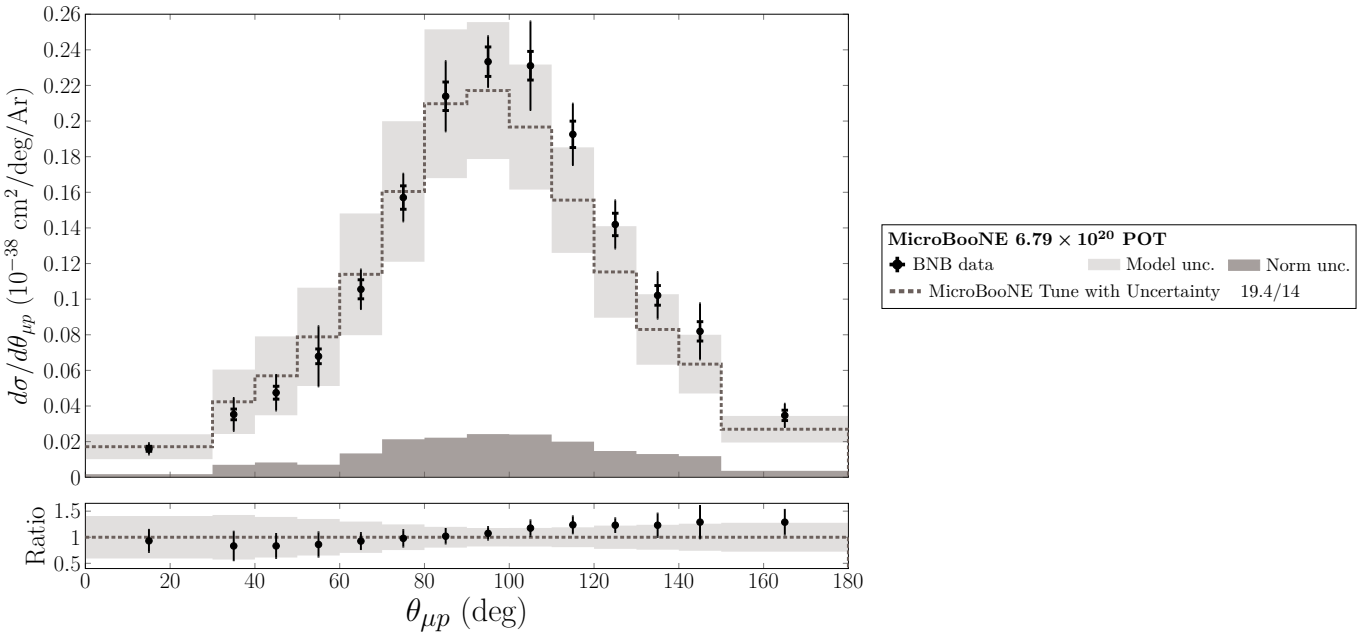

FIG. 33. Measured differential cross sections for block #7 ($\theta_{\mu p}$). Statistical (shape-only systematic) uncertainties are included in the inner (outer) error bars. The dark (light) gray band shows the remainder of the measurement uncertainty (theoretical uncertainty on the prediction). Error bars in the lower panels show the full measurement uncertainty.

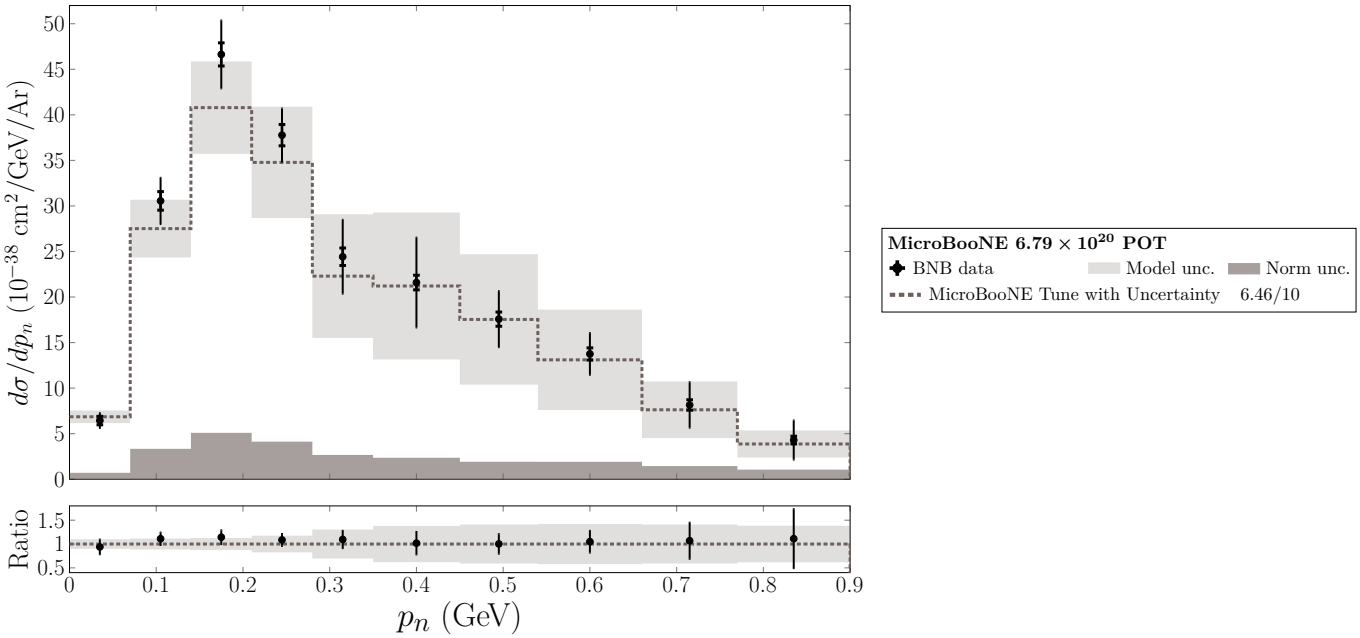

FIG. 34. Measured differential cross sections for block #8 (p_n). Statistical (shape-only systematic) uncertainties are included in the inner (outer) error bars. The dark (light) gray band shows the remainder of the measurement uncertainty (theoretical uncertainty on the prediction). Error bars in the lower panels show the full measurement uncertainty.

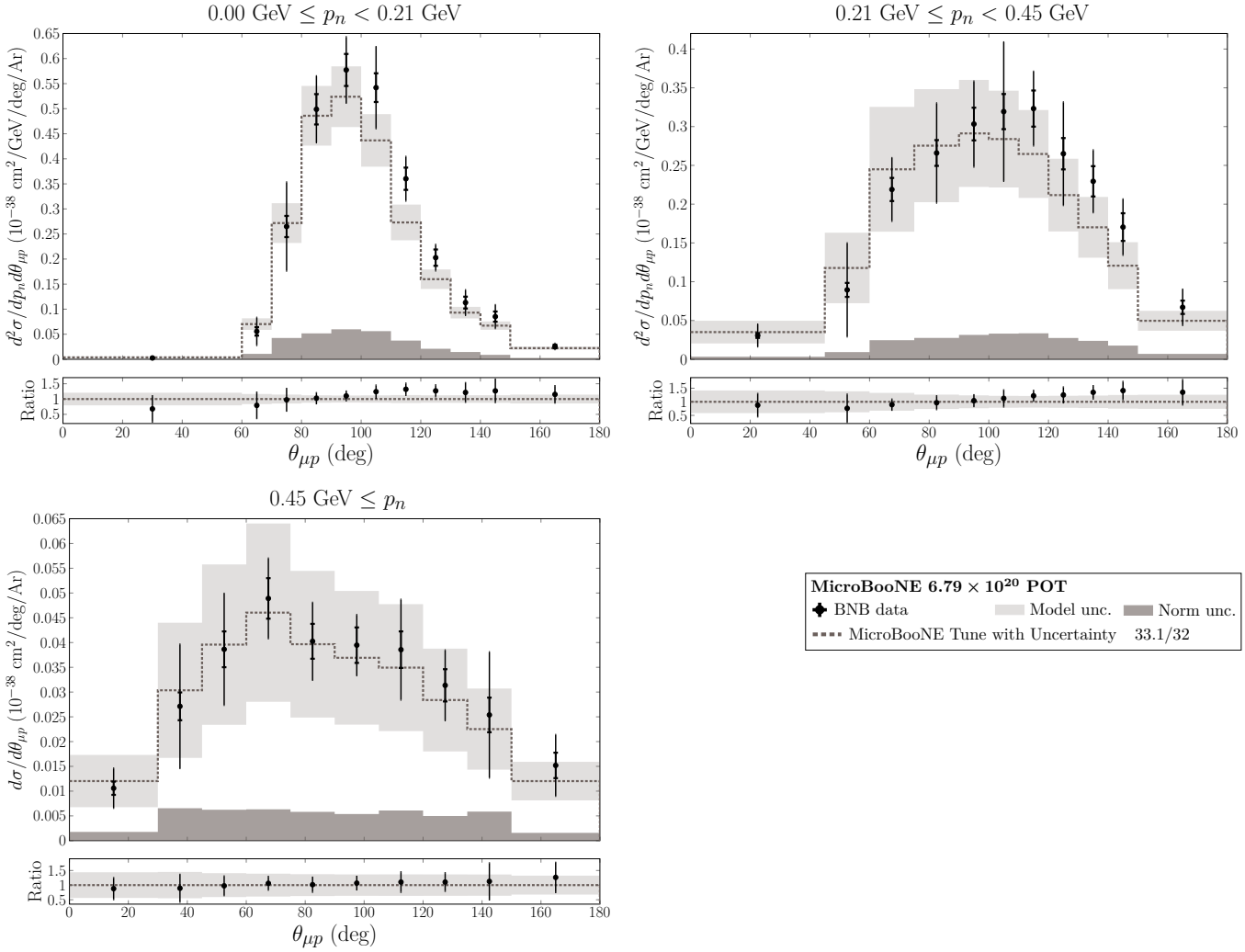

FIG. 35. Measured differential cross sections for block #9 ($p_n, \theta_{\mu p}$). Statistical (shape-only systematic) uncertainties are included in the inner (outer) error bars. The dark (light) gray band shows the remainder of the measurement uncertainty (theoretical uncertainty on the prediction). Error bars in the lower panels show the full measurement uncertainty.

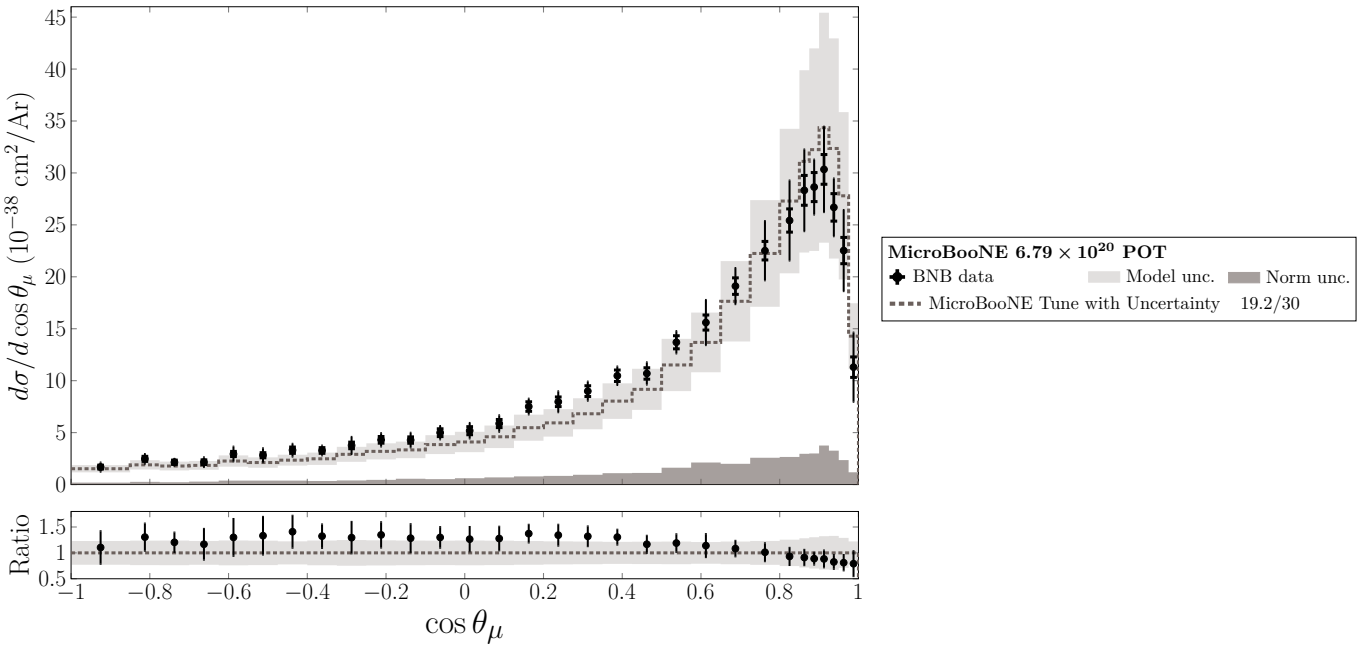

FIG. 36. Measured differential cross sections for block #10 ($\cos\theta_\mu$). Statistical (shape-only systematic) uncertainties are included in the inner (outer) error bars. The dark (light) gray band shows the remainder of the measurement uncertainty (theoretical uncertainty on the prediction). Error bars in the lower panels show the full measurement uncertainty.

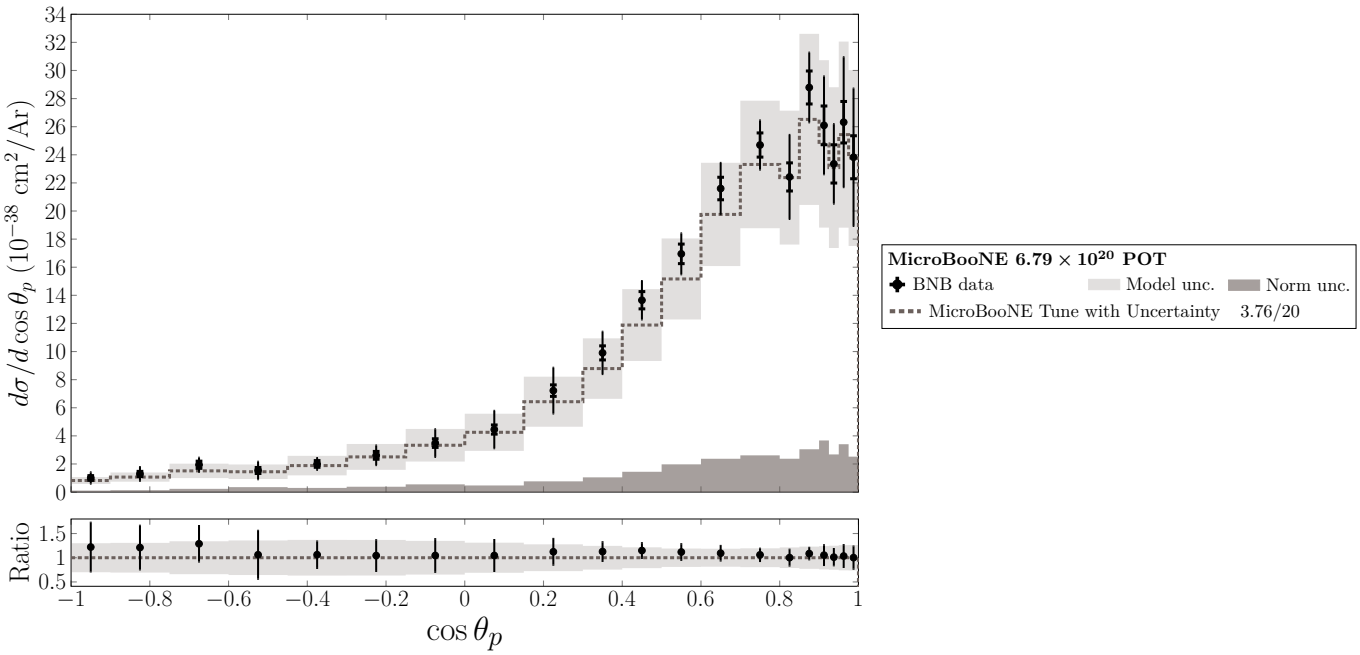

FIG. 37. Measured differential cross sections for block #11 ($\cos\theta_p$). Statistical (shape-only systematic) uncertainties are included in the inner (outer) error bars. The dark (light) gray band shows the remainder of the measurement uncertainty (theoretical uncertainty on the prediction). Error bars in the lower panels show the full measurement uncertainty.

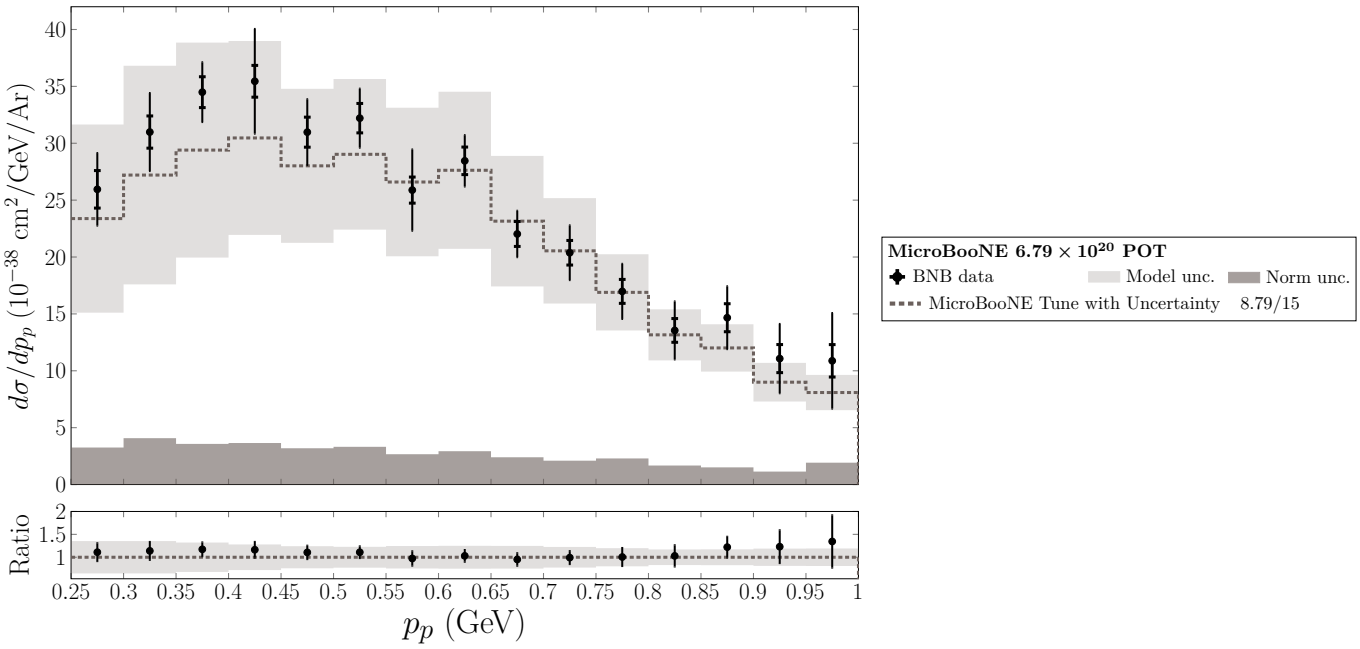

FIG. 38. Measured differential cross sections for block #12 (p_p). Statistical (shape-only systematic) uncertainties are included in the inner (outer) error bars. The dark (light) gray band shows the remainder of the measurement uncertainty (theoretical uncertainty on the prediction). Error bars in the lower panels show the full measurement uncertainty.

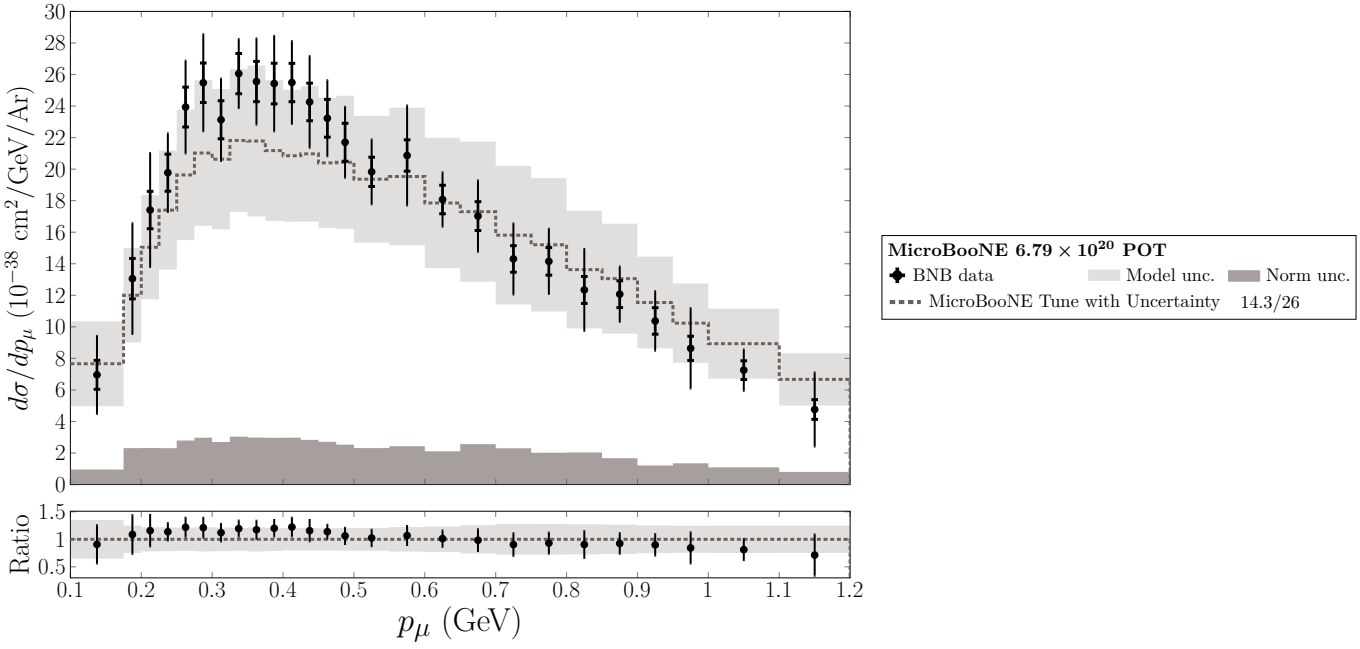

FIG. 39. Measured differential cross sections for block #13 (p_μ). Statistical (shape-only systematic) uncertainties are included in the inner (outer) error bars. The dark (light) gray band shows the remainder of the measurement uncertainty (theoretical uncertainty on the prediction). Error bars in the lower panels show the full measurement uncertainty.

VI. EXTENDED DATA RELEASE

The compressed tar archive file `extended_data_release.tar.bz2` contains detailed information from the analysis that allows many plots from the main text and this supplement to be reproduced. The archive file's contents may be extracted on Unix-like operating systems by running the command

```
tar xvfj extended_data_release.tar.bz2
```

in a terminal. All files discussed in the remainder of this section will be made available by this procedure.

The file `universes.txt` tabulates vectors of predicted event counts from the MicroBooNE simulation needed to reproduce all systematic covariance matrices used in the analysis. The first line of `universes.txt` contains a header of the form

```
numBins numCV numAltTypes numFullCorr numSum
```

where each of these variables takes an integer value. The header variables have the definitions given below.

numBins: The number of elements (1077) in each vector of predicted event counts reported in the file. The first 359 of these contain the quantity

$$n_j - O_j = \phi_j + B_j \tag{4}$$

in each reconstructed bin $0 \leq j \leq 358$ used for the cross-section measurements. The order and numbering scheme used for these bins is the same as in Table III of the main text. The notation used in Eq. (4) is the same as in Eq. (13) from the main text. The following group of 359 vector elements contain the same quantity but for the duplicate set of reconstructed bins in which the sideband selection discussed in Sec. V F from the main text has been applied. The bin ordering and definitions are otherwise the same as the first 359 elements. The final 359 elements of each vector contain the expected number of signal events ϕ_μ in each true bin μ. The bin ordering and definitions once again follow Table III from the main text.

numCV: The number of central-value universes (3) reported in the file. The nominal prediction of the MicroBooNE simulation is given by the first of these, which is labeled `CV`. To mitigate Monte Carlo statistical fluctuations when assessing detector-related systematic uncertainties, however, two additional central-value universes, `detVarCV1` and `detVarCV2`, were constructed with identical simulation parameters and used as replacement central-value predictions in specific cases when computing covariance matrix elements according to Eq. (14) from the main text.

numAltTypes: The number of alternative-universe covariance matrices (24) needed to compute the full set of systematic uncertainties adopted in the analysis. Each of these corresponds to a specific type of variation to the MicroBooNE simulation whose impact is studied with $N_{\text{univ}} \geq 1$ alternative universes.

numFullCorr: The number of fully-correlated systematic uncertainties (2) included in the analysis. As mentioned in Sec. V A of the main text, these are computed using a fractional uncertainty applied to each bin of the main central-value universe (`CV`).

numSum: The number of covariance matrices defined at the end of `universes.txt` as sums of other previously-defined covariance matrices.

The following `numCV` (3) lines of the file contain the event count vectors for each of the central-value universes. Each line starts with the name of the central value universe followed by its `numBins` (1077) elements.

After the central-value universe definitions, `universes.txt` contains `numAltType` definitions of alternative universes. Each of these begins with a line of the form

```
altName refCV numAltUniv
```

in which the first two fields are whitespace-delimited strings and the third is a positive integer. The `altName` field labels the simulation variation of interest, and `refCV` $\in \{$`CV`, `detVarCV1`, `detVarCV2`$\}$ specifies which of the central-value universes should be used when computing covariance matrix elements according to Eq. (14) from the main text. The integer `numAltUniv` gives the number N_{univ} of alternative universes that are defined for the current systematic variation. The following `numAltUniv` lines of the file each contain a vector with `numBins` (1077) elements corresponding to one of the relevant alternative universes. In the case of variations to the MicroBooNE Tune neutrino interaction model (`altName` begins with `xsec_` for these), the reconstructed bin counts are evaluated according to the special

prescription described in Sec. V B of the main text. The true signal event counts ϕ_μ are varied directly without special treatment for the last 359 elements of each alternative universe vector.

Following the `numAltType` (24) definitions of alternative universes, there are `numFullCorr` (2) definitions of fully-correlated systematic uncertainties given in `universes.txt`. Each of these appears as a single line of the form

```
FullCorrName FracUnc
```

in which `FullCorrName` $\in \{$`POT`, `numTargets`$\}$ labels the type of uncertainty (beam exposure and number of Ar targets in the fiducial volume, respectively). The `FracUnc` field contains the corresponding fractional uncertainty.

Finally, the last `numSum` (5) lines of `universes.txt` give definitions of new covariance matrices in terms of sums of others. Each definition appears on a single line. The line begins with the name `sumName` of the new covariance matrix followed by the number `numOther` of other covariance matrices included in the sum. The line concludes with `numOther` whitespace-delimited strings giving the names of the other covariance matrices. Allowed values for these names are the strings used earlier in the file within the `altName`, `FullCorrName`, and `sumName` fields, as well as the additional names `MCstats`, `EXTstats`, and `BNBstats`. These last three allowed names correspond to the precomputed statistical covariance matrices that appear in the subfolder `cov_matrices/`. Respectively, these label the Monte Carlo statistical uncertainty, the statistical uncertainty on the measured beam-off background, and the statistical uncertainty on the data measured when the BNB was active. These covariance matrices are provided explicitly because they cannot be computed from simple vectors of event counts; due to the multi-block structure of the analysis, events are shared between multiple bins, and a correct treatment of statistical correlations requires knowledge of the overlaps between each pair of bins.

The final line of `universes.txt` provides a definition for the summed covariance matrix `total`. This covariance matrix describes the full uncertainty on the measured event counts used for cross-section extraction (bins 0 to 358), the measured event counts in the sidebands (bins 359 to 717) and the MicroBooNE Tune prediction for the true signal event counts (bins 718 to 1077).

An example C++ program that interprets the contents of `universes.txt` is provided in the file `calc_covariances.C`. Like the `calc_chi2.C` program provided in the basic data release (see Sec. I of this supplement), `calc_covariances.C` relies on the `TMatrixD` class defined by ROOT and must either be executed using the ROOT C++ interpreter or be compiled against the ROOT shared libraries. Executing `calc_covariances.C` will parse the precomputed statistical covariance matrices and `universes.txt`. It will then create new covariance matrix files in the `cov_matrices/` subfolder representing all uncertainties used in the analysis. The total covariance matrix describing all uncertainties can be found in the file `cov_matrices/mat_table_extendedCov_total.txt` after the program has finished running. The format for both the precomputed statistical covariance matrix files and the new ones created by `calc_covariances.C` is identical to the `mat_table_cov_total.txt` file from the basic data release except for two differences. First, the number of bins is larger (1077 rather than 359). Second, the numerical values of the covariance matrix elements now represent uncertainties on event counts rather than flux-averaged total cross sections, so they are dimensionless.

For the first 718 bins represented in the universe vectors tabulated in `universes.txt`, the main central-value prediction (`CV`) is split into 11 separate event categories in the file `mat_table_mc_categories.txt`. Each row of the matrix defined in this file gives the contribution of a specific event category to the reconstructed bins in the `CV` universe vector. The categories $c \in [0, 10]$ are defined below in terms of the descriptions from Sec. III B of the main text.

0: Signal CC0πNp events in which the primary interaction mode was QE.

1: Signal CC0πNp events in which the primary interaction mode was 2p2h.

2: Signal CC0πNp events in which the primary interaction mode was resonance production.

3: Signal CC0πNp events with a primary interaction mode not specified by a prior category. In Figs. 1 and 7–14 from the main text, *Signal (CC other)* is used to label the sum of categories 2 and 3.

4: Background CC$N\pi$ events

5: Background CC0π0p events

6: Background Other ν_μ CC events

7: Background ν_e CC events

8: Background NC events

9: Background Out FV events

10: Background Other events

As described below, the beam-off background events are tabulated separately. Note that, as shown in Eq. (4), the beam-off background events do not contribute to the universe vectors by construction.

As implied by Eq. (29) of the main text, the portion of the extended data release covariance matrices representing the first 359 bins can be adjusted to represent uncertainties on the unfolded signal event counts $\hat{\phi}_\mu$ via transformation by the error propagation matrix $\mathfrak{E}$. The elements of $\mathfrak{E}$ are tabulated in the file `mat_table_err_prop.txt` for this purpose. A similar transformation using the additional smearing matrix A_C can be performed on the covariance matrix elements describing the MicroBooNE tune signal prediction (the last 359 bins) in order to obtain the theoretical uncertainty shown in Sec. V above. The elements of A_C are provided in the basic data release as described in Sec. I of this supplement. For completeness, the elements of the unfolding matrix U are also provided in the file `mat_table_unfolding.txt`. Note that all elements of $\mathfrak{E}$, A_C, and U are dimensionless.

The file `scale_factors.txt` contains the values of the integrated BNB ν_μ flux Φ and the number of Ar targets in the fiducial volume $\mathcal{N}_{\mathrm{Ar}}$ needed to convert event counts to cross sections. These are labeled in the file as `IntegratedFlux` (ν_μ/cm^2) and `NumArTargets` (dimensionless), respectively. Although it is not needed for the unit conversion, the beam exposure in POT used for the analysis is also given in the file with the label `BeamExposurePOT`.

The file `vec_table_data_bnb.txt` tabulates the measured number of events D_j in each reconstructed bin j for data taken when the BNB was active. The first 359 entries give the event counts for the selection criteria used to obtain the cross-section results. The remaining 359 entries give the corresponding results for the sideband selection defined in Sec. V F from the main text. Both groups of reconstructed bins use the same order and numbering scheme from Table III of the main text. The file `vec_table_data_ext.txt` has the same organization, but it tabulates the measured beam-off background event counts O_j.

[1] S. Gardiner, Mathematical methods for neutrino cross-section extraction, (2024), arXiv:2401.04065 [hep-ex].
[2] P. Abratenko *et al.* (MicroBooNE), First measurement of inclusive muon neutrino charged current differential cross sections on argon at E_ν ∼0.8 GeV with the MicroBooNE detector, Phys. Rev. Lett. **123**, 131801 (2019), arXiv:1905.09694 [hep-ex].